

**UNIVERSIDADE FEDERAL DE SANTA CATARINA
PROGRAMA DE PÓS-GRADUAÇÃO EM ENGENHARIA MECÂNICA**

**ESTUDO ANALÍTICO DA ESTRUTURA DE CHAMAS
ADIABÁTICAS PRÉ-MISTURADAS EM MEIOS POROSOS
INERTES E DESENVOLVIMENTO DE UM MODELO DE
CURVAS DE NÍVEL PARA SIMULAÇÕES NUMÉRICAS**

Tese submetida à

UNIVERSIDADE FEDERAL DE SANTA CATARINA

para a obtenção do grau de

DOUTOR EM ENGENHARIA MECÂNICA

FERNANDO MARCELO PEREIRA

Florianópolis, outubro de 2009

UNIVERSIDADE FEDERAL DE SANTA CATARINA
PROGRAMA DE PÓS-GRADUAÇÃO EM ENGENHARIA MECÂNICA

**ESTUDO ANALÍTICO DA ESTRUTURA DE CHAMAS ADIABÁTICAS
PRÉ-MISTURADAS EM MEIOS POROSOS INERTES E DESENVOLVIMENTO
DE UM MODELO DE CURVAS DE NÍVEL PARA SIMULAÇÕES NUMÉRICAS**

FERNANDO MARCELO PEREIRA

Esta tese foi julgada adequada para a obtenção do título de

DOUTOR EM ENGENHARIA

ESPECIALIDADE ENGENHARIA MECÂNICA

sendo aprovada em sua forma final.

Amir Antônio Martins de Oliveira Júnior, Ph.D. - Orientador

Fernando Fachini Filho, Dr. - Coorientador
Instituto Nacional de Pesquisas Espaciais - INPE

Eduardo Alberto Fancello, D.Sc. - Coordenador do Curso

BANCA EXAMINADORA

Amir Antônio Martins de Oliveira Júnior, Ph.D. - Presidente

Luis Fernando Figueira da Silva, Dr. - Relator
Pontifícia Universidade Católica do Rio de Janeiro - PUC-Rio

Thamy Cristina Hayashi, D.Sc.
Universidade Federal da Bahia - UFBA

Antônio Fábio Carvalho da Silva, Dr. Eng.
Universidade Federal de Santa Catarina - UFSC

Jáuber Cavalcante de Oliveira, Dr.
Universidade Federal de Santa Catarina - UFSC

Ao meu amor Beatriz.

Aos meus pais Isabel e Eraldo

Agradecimentos

Agradeço ao PRH09 - MECPETRO e à ANP pelo suporte financeiro.

Agradeço ao Prof. Amir Oliveira pela efetiva orientação, pela amizade que tanto prezo e, sobretudo, pelo exemplo como pesquisador e pessoa.

Agradeço ao Prof. Fernando Fachini pelo empenho na coorientação e incentivo para buscar desafios - "*O não nós já temos, vamos atrás do sim.*"

Agradeço a todos os amigos do LabCET pelo ótimo ambiente de trabalho e, principalmente, pela amizade ao longo desses anos. Em especial, agradeço aos amigos Catapan, Matelli, Leonel e Cirilo pelas diversas contribuições à tese através de discussões e sugestões.

Agradeço aos amigos Charles e Isaias pelo incentivo e pelo suporte nos momentos em que a tese teve que ser a única das minhas preocupações.

Agradeço aos meus pais, Isabel e Eraldo, por terem me propiciado condições de trilhar este caminho. Amo muito vocês e serei sempre grato a tudo o que fizeram por mim.

Agradeço, por fim, à Bia, meu amor e em breve minha esposa, pelo incentivo e companheirismo nesses anos do doutorado. Estarei ao seu lado, minha linda, sempre que você precisar.

Resumo

1. Introdução

A presente tese trata da combustão pré-misturada em meios porosos inertes em que a chama é estabilizada no interior do conjunto tridimensional de cavidades que forma a estrutura porosa. Como resultado, esses queimadores apresentam elevada temperatura de chama, ampla faixa de potências, baixa emissão de poluentes e possibilitam a queima de combustíveis de baixo poder calorífico. O objetivo da tese é desenvolver um modelo para a simulação numérica multidimensional de queimadores porosos capaz de captar as principais características térmicas do processo com baixo custo computacional.

O trabalho se divide em duas partes principais. A primeira parte é dedicada ao estudo analítico da estrutura de chamas pobres, estacionárias, adiabáticas e pré-misturadas em meios porosos inertes, cobrindo uma ampla faixa de riquezas. A segunda parte trata da construção de um modelo de curvas de nível para simulações numéricas multidimensionais de queimadores porosos.

2. Estudo Analítico da Estrutura de Chamas em Meios Porosos Inertes

A estrutura de chamas pré-misturadas, estacionárias e adiabáticas estabilizadas no interior de meios porosos inertes é investigada usando o método das expansões assintóticas acopladas, baseado em três escalas de comprimento características conforme mostrado na Fig. R1.

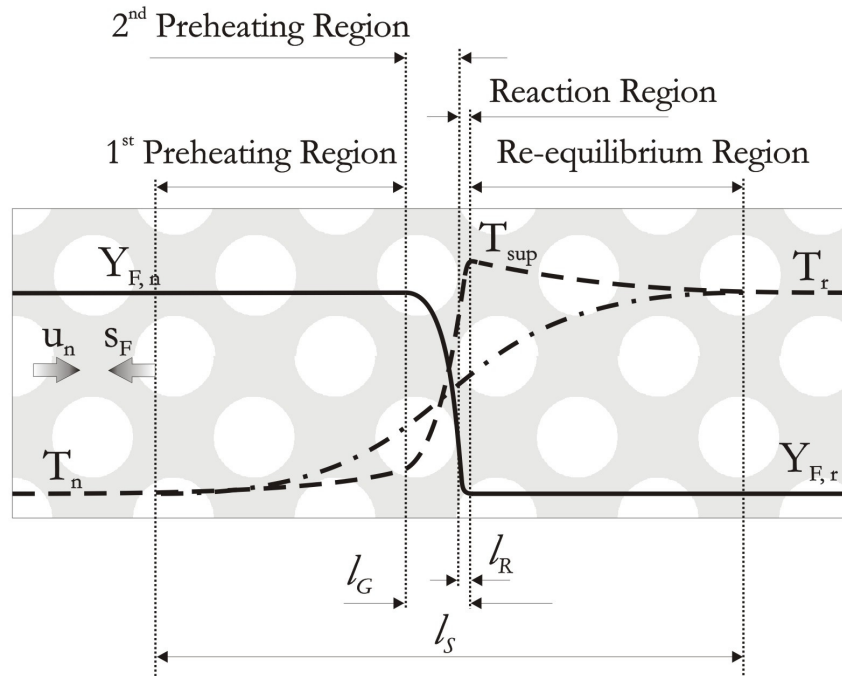


Figura R1 - Escalas características do problema

A escala característica do sólido é definida como $l_s = (1 - \epsilon) \lambda_s / (\epsilon \rho_n s_F c_p)$ e representa a região dominada pela difusão de calor no sólido e convecção no gás. A escala característica do gás é definida como $l_G = \epsilon \lambda_g / (\epsilon \rho_n s_F c_p)$ e representa a região

dominada pelos processos difusivos e convectivos na fase fluida. A escala característica da reação química é definida como $l_R/l_G = \delta$, sendo δ um número pequeno, e representa a região dominada pela reação química e difusão no gás. Estas escalas são suficientemente separadas, $l_S \gg l_G \gg l_R$, para permitir a solução do problema pelo método de expansões assintóticas acopladas.

O não-equilíbrio e a transferência de calor entre as fases são analisados em cada escala e hipóteses simplificativas são assumidas. Os modelos propostos resultam em soluções analíticas para as temperaturas das fases sólida e fluida, para as frações mássicas de combustível e oxidante, e para a velocidade de propagação de chama. A expressão para a velocidade de chama,

$$s_F^2 = \frac{2A\rho_f^2 \lambda_g Y_{O_n} T_{gf}^a e^{-\beta/\alpha} \left[\frac{\delta^2 L e_F (1-\phi)}{d_F^2} \right]}{(\rho_n^2 c_p)} \exp \left\{ \frac{-\beta(1-\theta_{gf}^{(*)})}{1-\alpha(1-\theta_{gf}^{(*)})} + mn \right\},$$

é obtida assumindo energia de ativação elevada, e inclui o efeito do parâmetro $m = d_\theta^+ / (d_\theta^+ + d_\theta^-)$, que é a razão entre o fluxo de calor a jusante da chama, d_θ^+ , e a geração total de calor ($d_\theta^+ + d_\theta^-$). Quando $m \rightarrow 1/2$ tem-se a extinção da chama.

A transferência de calor entre as fases é determinada pelo parâmetro $N = \lambda_s h_v / (\rho_n s_F c_p)^2$. Três soluções são obtidas para diferentes limites de N .

2.1. Solução para $N \sim O(1)$

No caso de $N \sim O(1)$, a transferência de calor entre as fases é moderada, resultando em uma larga região de não-equilíbrio térmico da ordem de l_s como pode ser visto na Fig. R2. Essa condição é típica de riquezas ϕ próximas da estequiométrica.

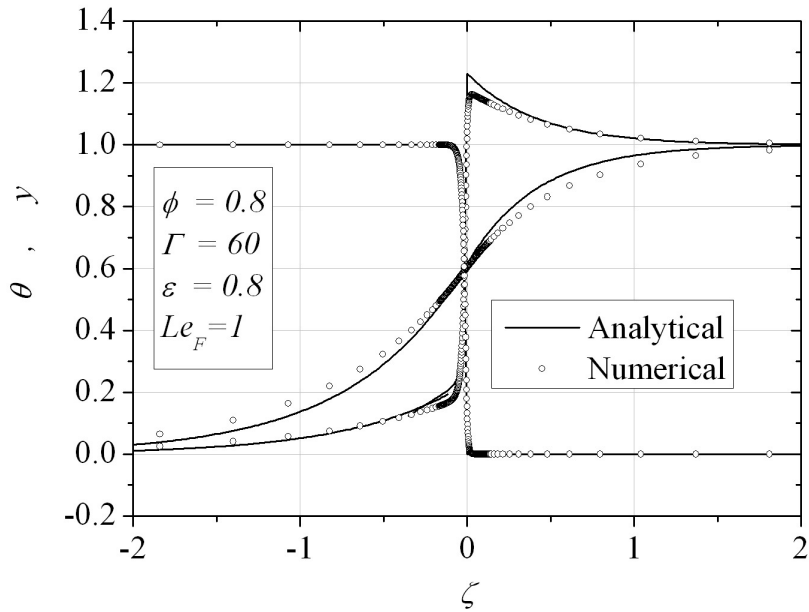


Figura R2 - Solução analítica e numérica da estrutura da chama para $N \sim O(1)$.

Os resultados mostram a existência de um número, $N_\varepsilon = 4\varepsilon^2 / [N(1-\varepsilon)]$, que determina as propriedades da chama, universalizando os resultados. Assim, a recirculação de calor induzida pelo meio poroso é dada por $\eta_{rec} = (1 + N_\varepsilon)^{-1/2}$, a temperatura do gás na chama por $\theta_g(\xi_f^+) = 1 + \eta_{rec}$, e a temperatura do sólido na chama por $\theta_s(\xi_f^+) = \theta_g(\xi_f^+) / 2$. A Fig. R3 mostra a variação das propriedades do meio poroso,

ε e $\Gamma = \lambda_s / \lambda_g$, e da mistura, ϕ , que resultam nos mesmos valores das variáveis na chama.

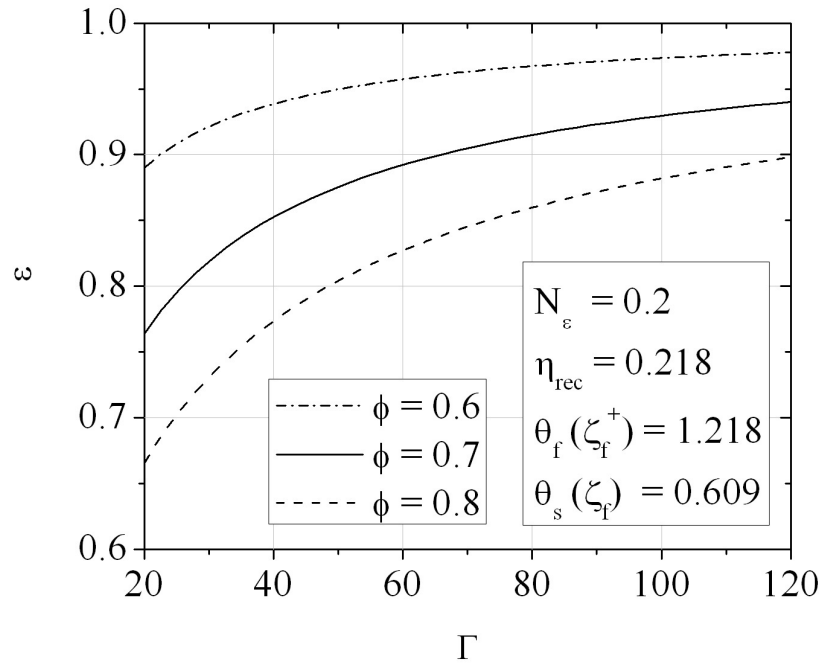


Figura R3 - Valores de Γ , ε e ϕ que resultam no mesmo N_ε .

Uma importante característica da combustão em meios porosos para $N \sim O(1)$ é o aumento da temperatura adimensional da chama, $\theta_g(\zeta_f^+) = 1 + \eta_{rec}$, para valores decrescentes de ϕ , isto é, η_{rec} cresce com o empobrecimento da mistura, como mostrado na Fig. R4.

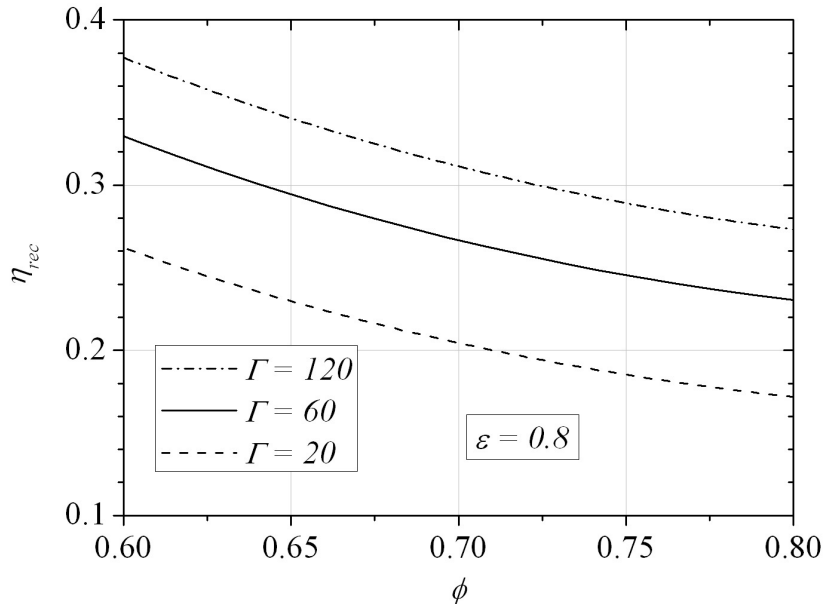


Figura R4 - Variação de η_{rec} com ϕ e Γ para $N \sim O(1)$.

2.2. Solução para $N \sim O(\Gamma)$

No caso de $N \sim O(\Gamma)$, a transferência de calor entre as fases é intensa, resultando em equilíbrio térmico em uma larga região, da ordem de l_s . O não-equilíbrio térmico entre as fases é encontrado em uma região estreita entorno da chama, da ordem de l_G . A Fig. R5 mostra a estrutura da chama para $N \sim O(\Gamma)$. Essa condição é típica de misturas ultra-pobres que resultam em baixas velocidades de chama e, conseqüentemente, em longo tempo de contato térmico entre as fases.

Para $N \sim O(\Gamma)$ a temperatura adimensional da chama, $\theta_{gf}^{(*)}$, decresce com valores decrescentes de ϕ , como mostrado na Fig. R6. Este comportamento é o contrário daquele mostrado na Fig. R4, para $N \sim O(1)$, e indica que existe um limite máximo para a temperatura adimensional da chama.

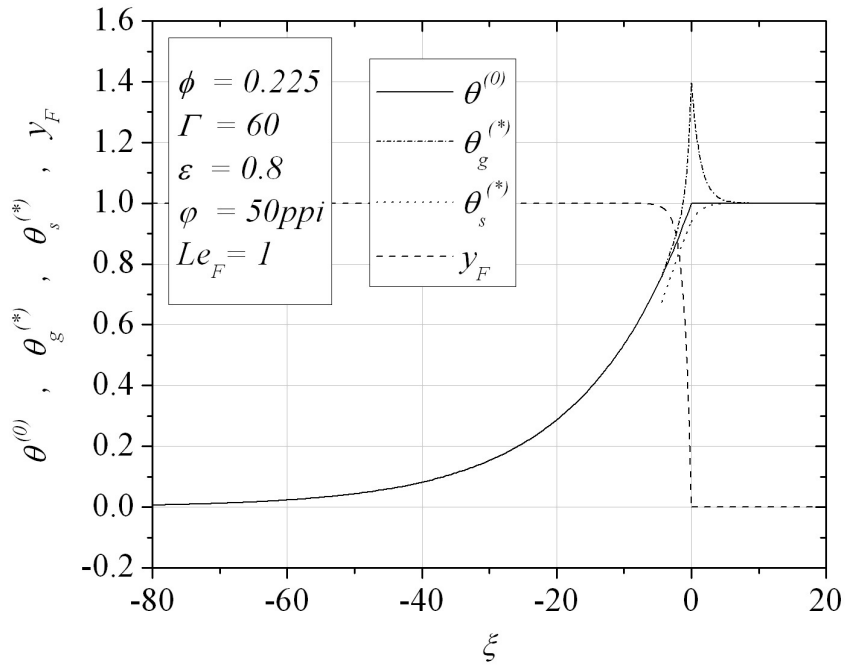


Figura R5 - Solução analítica da estrutura da chama para $N \sim O(\Gamma)$.

A Fig. R7 mostra a velocidade de chama obtida para diferentes tamanhos de poro. Nota-se que abaixo de certo valor de ϕ não se encontra mais solução, assim, os resultados para $N \sim O(\Gamma)$ prevêm (qualitativamente) o limite inferior de inflamabilidade para a combustão pré-misturada em meios porosos. Nota-se também que esse limite depende das propriedades da matriz porosa.

2.3. Solução para $1 < N < \Gamma$

Uma formulação alternativa, empregando a função excesso de entalpia, é capaz de captar a solução para a situação intermediária em que $1 < N < \Gamma$, o que equivale à combustão com valores intermediários de ϕ . A Fig. R8 mostra a estrutura da chama

para $N = 4,75$. Nesse caso, nota-se que as temperaturas das duas fases se aproximam, no entanto, a hipótese de equilíbrio térmico local ainda não é válida.

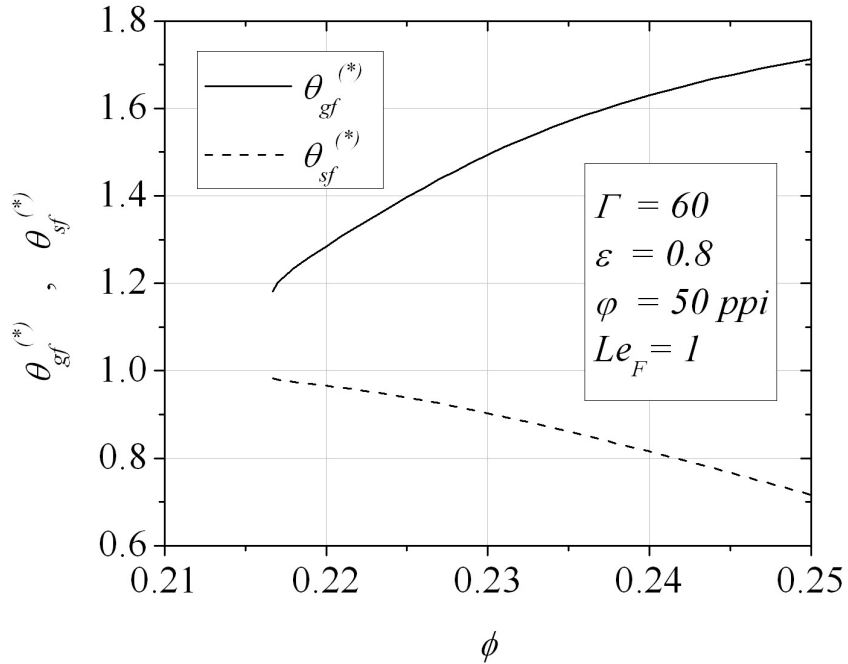


Figura R6 - Temperaturas adimensionais na chama em função de ϕ para $N \sim O(\Gamma)$.

A Fig. R9 apresenta a temperatura adimensional da chama θ_{gf} em função de ϕ . O modelo baseado na função excesso de entalpia tem uma boa concordância com o modelo de $N \sim O(1)$, enquanto apresenta uma concordância precária com o modelo de $N \sim O(\Gamma)$. No entanto, este modelo alternativo é capaz de capturar a inversão do comportamento θ_{gf} em relação a ϕ , o que corresponde ao limite máximo para a temperatura adimensional da chama.

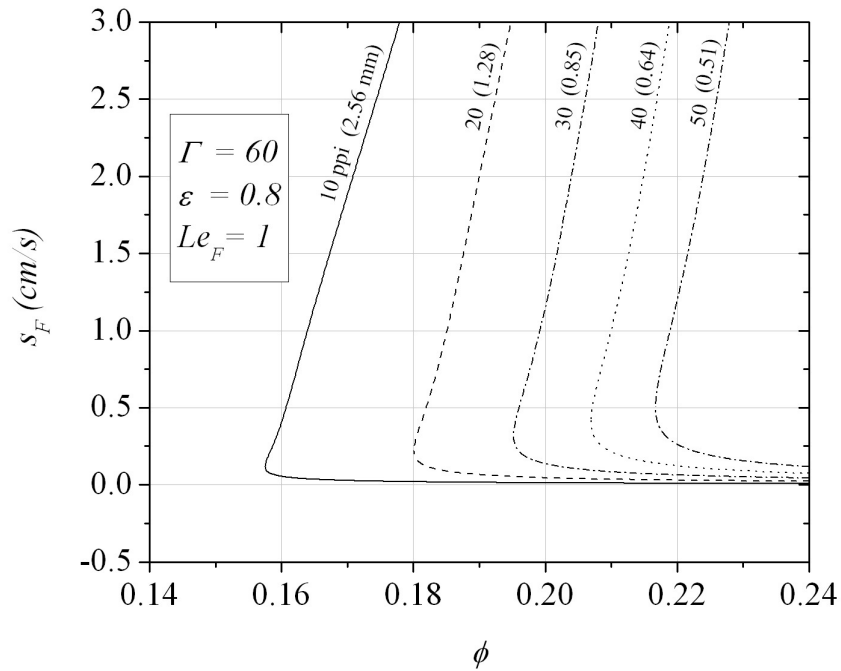


Figura R7 - Variação de s_F com o tamanho de poro e ϕ .

3. Desenvolvimento de um Modelo de Curvas de Nível para Simulações Numéricas

Os resultados analíticos são usados para desenvolver um modelo micro-escala (submalha) para a velocidade de chama que pode ser usado em simulações tridimensionais de escoamentos reativos em meios porosos. Para tanto, o problema é formulado através de uma forma simplificada das equações de conservação em termos de médias volumétricas (modelo macro-escala) usando a equação G (método de curvas de nível - *level-set method*) para descrever o movimento da frente de chama.

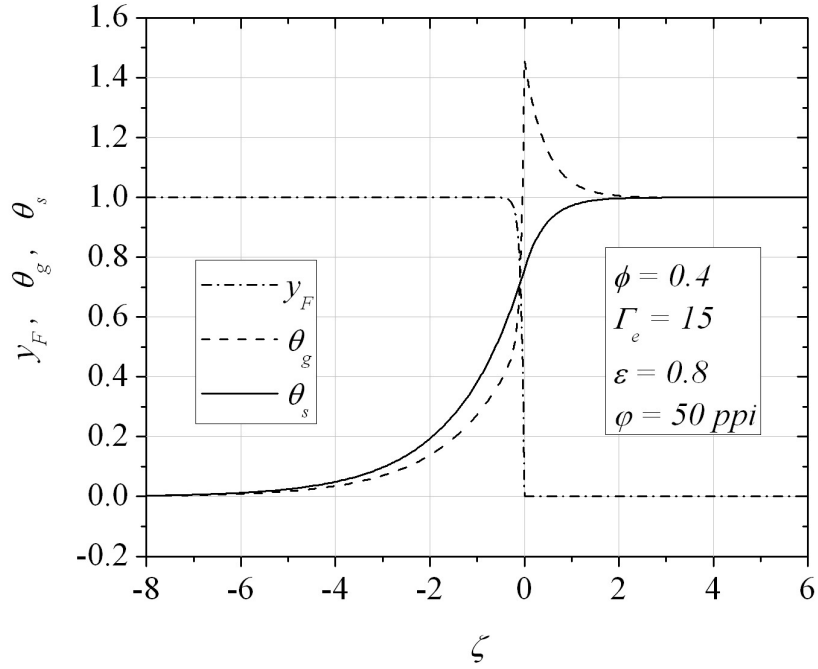


Figura R8 - Solução analítica da estrutura da chama para $1 < N < \Gamma$.

No método de curvas de nível considera-se o campo de um escalar não-reativo G , onde a chama é assumida como sendo uma superfície fina, coincidente com a iso-superfície $G = G_0$, conforme Fig. R10. A movimentação da chama é governada pela equação

$$\frac{\partial G}{\partial t} + u \cdot \nabla G = v_F |\nabla G|,$$

onde $v_F = s_F (\rho_n / \rho_f)$. Esta equação representa o balanço entre a convecção da iso-superfície $G = G_0$ pelo escoamento e a propagação local desta superfície causada pela propagação da chama.

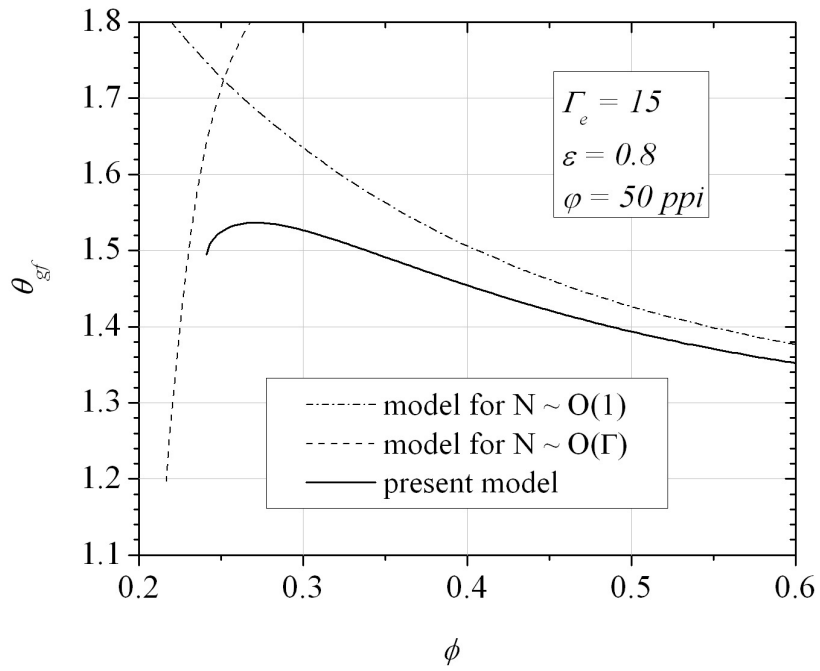


Figura R9 - Temperatura adimensional do gás na chama em função de ϕ .

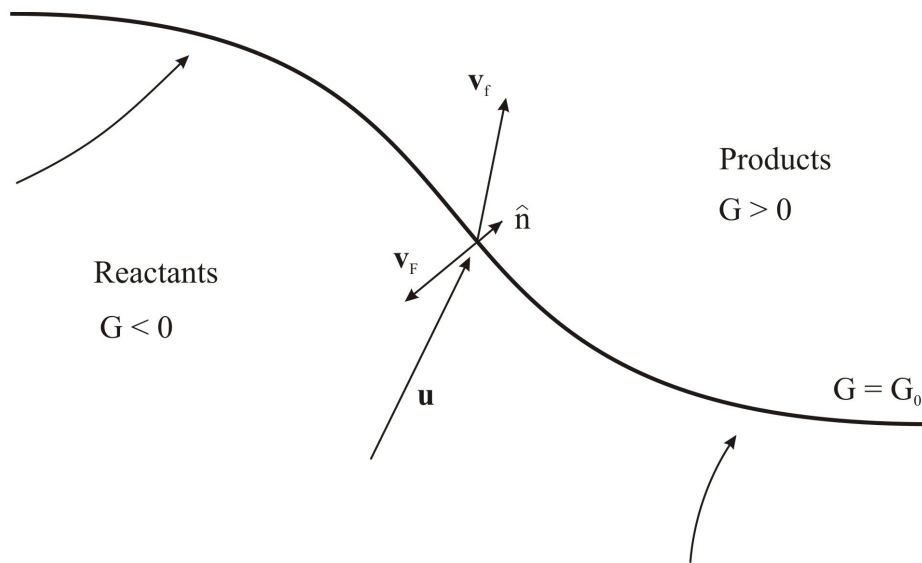


Figura R10 - Método de curvas de nível para movimentação da chama.

Nesse modelo, a solução da equação das espécies químicas não é necessária e toda a informação sobre a reação química é fornecida pela expressão para a velocidade de chama (modelo sub-malha). A liberação do calor de reação é modelada como uma fonte concentrada na equação da conservação da energia para o gás.

Uma versão 1D do modelo proposto é implementada para ilustrar o método, resultando em boa concordância com um modelo convencional baseado na solução do conjunto completo de equações de conservação. Dois problemas teste são propostos e avaliados:

3.1. Queimador infinito

O modelo proposto é empregado para resolver um queimador infinito e adiabático. A Fig. R11 mostra as velocidades de chama previstas pelo modelo de curvas de nível em comparação com o modelo convencional.

3.2. Queimador poroso radiante

O modelo proposto é também empregado para avaliar a estabilização da chama em um queimador finito com perdas de calor por radiação nas extremidades. Na Fig. R12 é mostrado o deslocamento da chama em função da velocidade de entrada dos reagentes em um queimador poroso radiante.

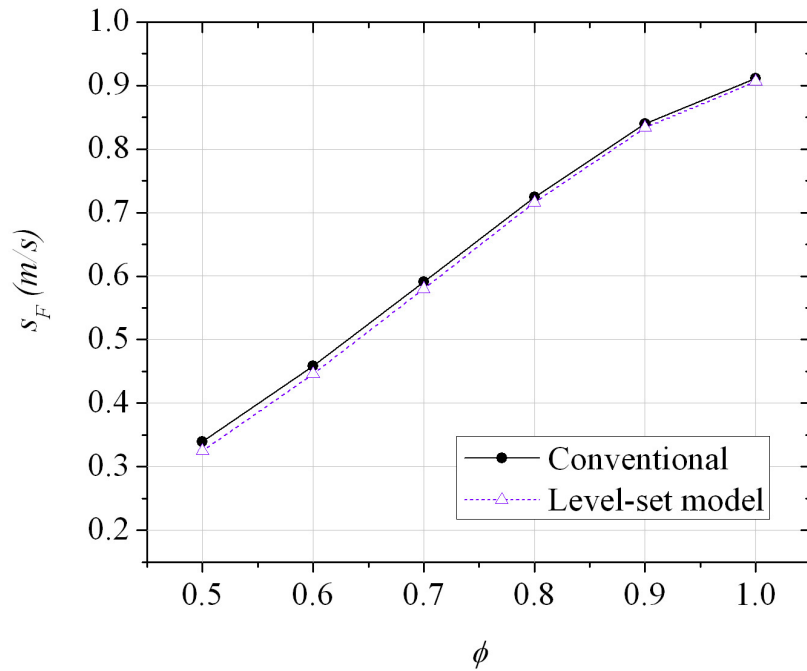


Figura R11 - Velocidades de chama previstas para um queimador infinito.

Como mostrado na Fig. R13, a vantagem do método proposto é o tempo computacional reduzido para alcançar a convergência, principalmente em geometrias complexas. O modelo convencional necessita de maior refinamento de malha do que o modelo de curvas de nível para a obtenção de resultados independentes. Assim, o modelo de curvas de nível mostrou-se de 6 a 16 vezes mais rápido do que o convencional.

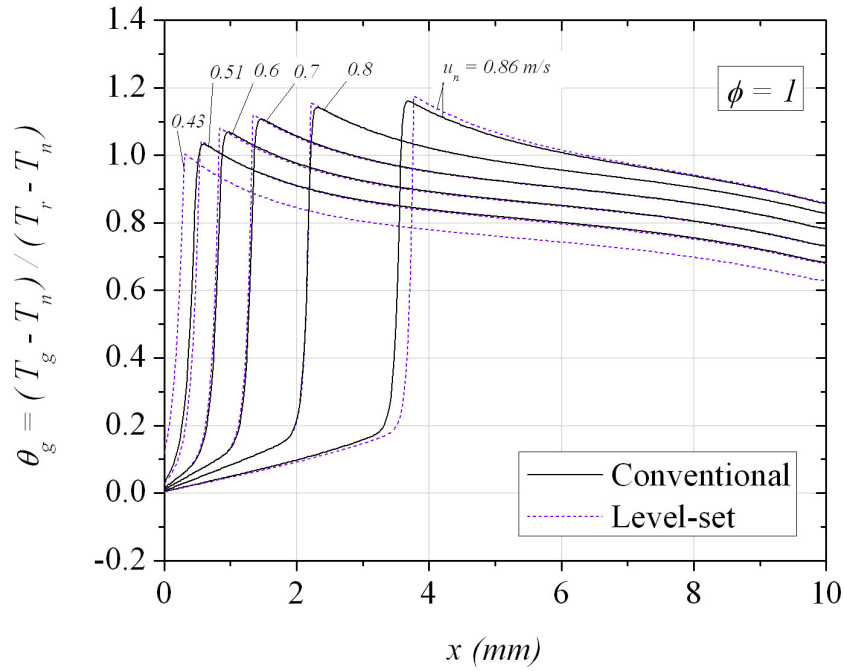


Figura R12 - Perfil de temperatura do gás em função da velocidade de entrada dos reagentes.

4. Conclusões

As seguintes conclusões podem ser tiradas a partir dos resultados obtidos:

- Expressões para as temperaturas de ambas as fases, fração mássica de combustível e oxidante, e velocidade de chama, são obtidas pelo método das expansões assintóticas acopladas, assumindo elevada energia de ativação.
- Um parâmetro, N_ε , que universaliza o problema é identificado.
- O limite inferior de inflamabilidade para chamas em meios porosos é alcançado quando a transferência de calor entre as fases é intensa, $N \sim O(\Gamma)$, e depende das propriedades da matriz porosa.

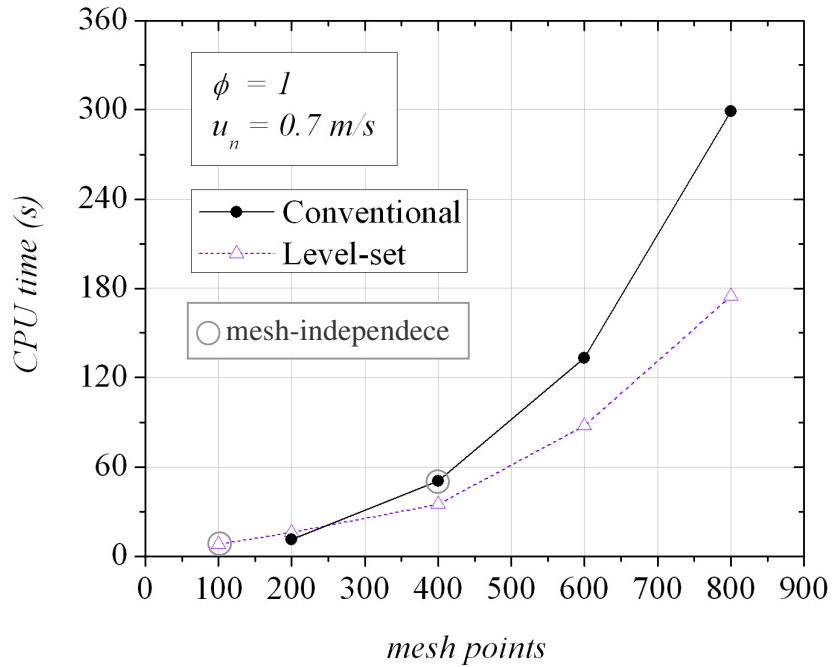


Figura R13 - Tempo computacional em função do tamanho da malha.

- Existe um limite máximo para a temperatura adimensional da chama θ_{gf} , sendo que θ_{gf} decresce com ϕ para $N \sim O(1)$ e cresce com ϕ para $N \sim O(\Gamma)$.
- O modelo de curvas de nível proposto reduz o tempo computacional para a solução de problemas de combustão em meios porosos, sendo, portanto, uma opção viável para a modelagem de queimadores com geometrias complexas.

Os resultados obtidos nessa tese podem ser estendidos através da solução analítica do mecanismo cinético de 4 passos, do desenvolvimento de um modelo para o caso de $N \gg \Gamma$, da inclusão de reações químicas superficiais e da implementação multidimensional do modelo de curva de nível proposto.

ANALYSIS OF THE PREMIXED FLAME STRUCTURE
WITHIN POROUS INERT MEDIA AND
DEVELOPMENT OF A LEVEL SET MODEL
FOR NUMERICAL SIMULATIONS

Fernando Marcelo Pereira

OCTOBER 2009

Table of Contents

List of Tables	vi
List of Figures	vii
Abstract	xi
Nomenclature	xii
1 Introduction	1
1.1 The combustion in porous media and its applications	1
1.2 Challenges for the numerical simulation.	9
1.3 Objectives	13
1.4 Organization of the manuscript	13
2 Problem formulation	15
2.1 Local problem	15
2.2 Volume averaging method	18
2.3 Semi-heuristic volume-averaged conservation equations	23
2.4 Reaction source term	26
2.5 Radiant source term	29
2.6 Simplifying assumptions	31
3 Asymptotic solution for moderately lean mixtures	33
3.1 Introduction	33
3.2 Length-scales and thermal non-equilibrium	38
3.3 Mathematical formulation	45
3.3.1 Non-dimensionalization	45
3.3.2 Outer zone: problem of the order of unity	47
3.3.3 Inner zone: problem of the order of Γ^{-1}	53

3.3.4	Inner zone: reaction region $O(\delta\Gamma^{-1})$	56
3.3.5	Model summary	61
3.4	Discussion	62
3.4.1	Flame structure	63
3.4.2	Influence of the equivalence ratio and Γ	65
3.4.3	Influence of the matrix porosity	69
3.4.4	Influence of the Lewis number	71
3.4.5	The porous-media-flame number	72
3.4.6	Comparison with a numerical solution	73
3.5	Conclusions	75
4	Asymptotic solution for ultra-lean mixtures	79
4.1	Introduction	79
4.2	Length scales	82
4.3	Mathematical formulation	83
4.3.1	Outer zone: problem of the order of unity	84
4.3.2	Inner zone: problem of the order of Γ^{-1}	86
4.3.3	Inner zone: reaction region $O(\delta\Gamma^{-1})$	90
4.3.4	Model summary	91
4.4	Discussion	91
4.4.1	Influence of the equivalence ratio	92
4.4.2	Influence of the matrix properties	98
4.4.3	Influence of the Lewis number	99
4.4.4	Flame structure	100
4.5	Conclusions	102
5	Alternative solution for intermediate lean mixtures	105
5.1	Introduction	105
5.2	Mathematical formulation	106
5.2.1	Non-dimensionalization	106
5.2.2	Excess enthalpy formulation	107
5.2.3	Approximated closed form solution for the excess enthalpy function	108
5.2.4	Inner zone: reaction region $O(\delta\Gamma^{-1})$	110
5.2.5	Model summary	110
5.3	Discussion	111
5.3.1	Flame structure	111
5.3.2	Maximum superadiabatic flame temperature	113
5.4	Conclusions	117

6	A Level-set model for the numerical simulation of porous burners	119
6.1	Introduction	119
6.2	Level-set method	121
6.3	Mathematical formulation	124
6.3.1	Macroscopic-level model	124
6.3.2	Microscopic-level model	125
6.3.3	Model validation	129
6.3.4	Numerical method	132
6.4	Discussion	135
6.4.1	Adiabatic combustion in an infinite medium	136
6.4.2	Flame stabilization in a porous radiant burner	138
6.4.3	Discussion on multi-dimensional implementation	148
6.5	Conclusions	151
7	Conclusion	153
7.1	Summary of conclusions	153
7.2	Suggestions for future works	155
	Bibliography	157

List of Tables

3.1	Properties and parameters used in the calculations and results for $\varepsilon = 0.8$, $\phi = 0.8$, $\Gamma = 60$ and $Le = 1$	63
4.1	Properties and parameters used in the calculations and results for $\phi = 0.225$, $\Gamma = 60$, $\varepsilon = 0.8$, $\varphi = 50$ <i>ppi</i> and $Le_F = 1$	93
5.1	Properties and parameters used in the calculations and a results for $\phi = 0.5$, $\Gamma_e = 15$, $\varepsilon = 0.8$, $\varphi = 50$ <i>ppi</i> and $Le_F = 1$	113
6.1	Properties and parameters used in the calculations.	136

List of Figures

1.1	SiC foam porous burner [1].	3
1.2	Gas-phase (T_g) and solid-phase (T_s) temperatures and mass fraction of fuel (Y_F) distributions for the steady-state combustion in a porous inert medium with heat losses at the ends. The heat fluxes \dot{q}_u , \dot{q}_k and \dot{q}_r are respectively the convection, conduction and radiation heat fluxes, \dot{q}_{ku} is the interphase heat transfer (surface convection), \dot{q}_{rec} is the heat recirculation, which includes the conduction and radiation through the solid-phase, and \dot{s}_r is the reaction energy conversion.	4
1.3	Porous radiant burner with multiple injections [2].	11
1.4	Infrared thermographic image of a porous radiant burner with multiple injections [2].	12
2.1	The local problem of a reacting fluid-phase flowing through a stationary inert solid-phase.	16
2.2	The representative elementary volume and position vectors	19
3.1	Rendering of the temperatures and fuel mass fraction distributions for the different characteristic length-scales of the problem.	39
3.2	Non-dimensional gas- and solid-phase temperatures and fuel mass fraction profile (solution of the $O(1)$ problem).	64
3.3	Non-dimensional gas- and solid-phase temperatures and fuel mass fraction profile (solution of the $O(\Gamma^{-1})$ problem).	65
3.4	Interphase heat transfer parameter N as a function of ϕ and Γ	66

3.5	Non-dimensional solid-phase temperature at the flame $\theta_s^{(0)}(\zeta_f)$ as a function of ϕ and Γ	67
3.6	Heat recirculation efficiency η_{rec} as a function of ϕ and Γ	68
3.7	Ratio s_F/s_F^0 as a function of ϕ and Γ	69
3.8	Ratio l_R/l_R^0 as a function of ϕ and Γ	70
3.9	Dependence of η_{rec} , $\theta_s^{(0)}(\zeta_f)$ and l_R/l_R^0 on ε	71
3.10	Dependence of the ratio s_F/s_F^0 and N on ε	72
3.11	Heat recirculation efficiency η_{rec} as a function of Le_F	73
3.12	Variation of ε with Γ and ϕ for $N_\varepsilon = 20$	74
3.13	Comparison of the present model to a numerical solution.	76
3.14	Comparison of the present model to a numerical solution in dimensional variables.	77
4.1	Schematic representation of the temperatures and fuel mass fraction distributions and the different characteristic length-scales of the problem.	83
4.2	The flame velocity s_F as function of ϕ . The upper branch corresponds to the physical solution.	94
4.3	The parameter N_0 as a function of ϕ	95
4.4	Gas and solid-phase temperatures at the flame as a function of ϕ	96
4.5	Dependence of N_0 , $\theta_{gf}^{(*)}$, $\theta_{sf}^{(*)}$ and s_F on ε	99
4.6	Dependence of N_0 , $\theta_{gf}^{(*)}$, $\theta_{sf}^{(*)}$ and s_F on φ	100
4.7	The flame velocity s_F as function of ϕ for different values of φ . The numbers in parenthesis are the corresponding mean pore diameters.	101
4.8	Dependence of N_0 , $\theta_{gf}^{(*)}$, $\theta_{sf}^{(*)}$ and s_F on Le_F	102
4.9	Flame structure for $\phi = 0.225$, $\Gamma = 60$, $\varepsilon = 0.8$, $\varphi = 50$ ppi and $Le_F = 1.103$	
5.1	Normalized superadiabatic flame temperature θ_{sup}	112
5.2	Flame structure for the condition described in Table 5.1.	114
5.3	Gas-phase temperature at the flame as a function of the equivalence ratio	115

5.4	Gas-phase temperature at the flame as a function of the equivalence ratio and Γ_e	116
5.5	Maximum superadiabatic flame temperature, $\theta_{sup,max}$, and the corresponding equivalence ratio, $\phi(\theta_{sup,max})$, as function of the porosity . .	117
6.1	Velocity balance at the flame surface.	122
6.2	Schematic representation of the temperatures and fuel mass fraction distributions for the different characteristic length-scales of the problem.	126
6.3	Source term distribution in the computational mesh.	133
6.4	Comparison of the predicted flame velocity for the conventional model and the level-set model with concentrated heat release.	137
6.5	Comparison of the gas- and solid-phase temperatures between a conventional model and the level-set model for $\phi = 1$	138
6.6	Comparison of the gas- and solid-phase temperatures between a conventional model and the level-set model for $\phi = 0.5$	139
6.7	Adjustment of the parameter C in Eq. (6.35).	140
6.8	Gas-phase temperature distribution as a function of the inlet flow velocity u_n for $\phi = 1$	141
6.9	Inlet velocity u_n and flame temperature $\theta_{g,f}$ as a function of the flame position x_f	142
6.10	Gas and solid-phase temperatures for $u_n = 0.51$ and 0.86 m/s.	144
6.11	Forward ($q_{rad,L}$) and backward ($q_{rad,0}$) radiant losses as a function of the inlet velocity for $\phi = 1$	145
6.12	Gas-phase temperature distributions as a function of the inlet flow velocity u_n for $\phi = 1$	146
6.13	Gas-phase temperature distributions as a function of the inlet flow velocity u_n for $\phi = 0.6$	147
6.14	Dependence of the gas-phase temperature on the numerical mesh for the conventional model.	148

6.15	Dependence of the gas-phase temperature on the numerical mesh for the level-set model.	149
6.16	CPU time vs mesh points.	150

Abstract

This thesis is divided in two parts. The first part is devoted to the analytical study of the structure of premixed flames within porous inert media, covering a wide range of equivalence ratios. The second part is devoted to the construction of a level-set model for multidimensional numerical simulations of porous burners.

The structure of stationary adiabatic lean premixed planar flames within porous inert media is investigated using the asymptotic expansion method based on three characteristic length-scales. The non-equilibrium between the phases and the inter-phase heat transfer are analyzed in each scale and simplifying hypothesis are assumed. The models developed result in closed form solutions for the solid- and gas-phase temperatures, fuel and oxidant mass fractions and flame propagation velocity. The results also predict (qualitatively) the lean flammability limit and the maximum superadiabatic temperature for lean mixtures.

The analytical results were used to construct a microscale (subgrid) model for the flame speed to be used in the simulation of three-dimensional flow and reaction in porous media. The problem is formulated with a simplified form of the volume-averaged conservation equations (macroscale model) using the G -equation (level-set method) to describe the movement of the flame front. A 1D version of the model is implemented to illustrate the method, showing reasonable agreement with a conventional model based on the solution of the full set of conservation equations. The advantage of the proposed method is the smaller *CPU* times required to achieve convergence.

Nomenclature

A	Pre-exponential factor,	$\text{m}^3(\text{kg s})^{-1}$
A_{gs}	interphase surface area ,	m^2
a	Temperature exponent (reaction rate expression),	-
c_p	Specific heat at constant pressure,	$\text{J}(\text{kg K})^{-1}$
D	Mass diffusion coefficient,	$\text{m}^2 \text{s}^{-1}$
Da	Damköhler number,	-
\overline{Da}	Modified Damköhler number of the $O(\delta\Gamma^{-1})$ problem,	-
d	Dimensionless flux in the reaction region,	-
E_a	Activation energy,	J mol^{-1}
f	Body force,	m s^{-2}
G	Nonreactive scalar,	-
H	Excess enthalpy function,	-
h_v	Volumetric convection heat transfer coefficient,	$\text{W}(\text{m}^3 \text{K})^{-1}$
h_i	Enthalpy of species i ,	J kg^{-1}
I_λ	Spectral radiant intensity,	$\text{W m}^{-2}(\text{sr } \mu\text{m})^{-1}$
\mathbf{K}	Permeability tensor,	m^2
k	Reaction rate coefficient,	s^{-1}
L	System length-scale,	m
Le	Lewis number ($\equiv \lambda_g/\rho c_p D$),	-
l	Characteristic length scale,	m
l_m	Mean free-path to radiation,	m

M	Molar mass,	kmol kg^{-1}
m	Energy flux ratio ($\equiv d_{\theta}^{+}/(d_{\theta}^{+} + d_{\theta}^{-})$),	-
m_g	Mass flow rate,	kg s^{-1}
n	Translation in the coordinate system ($\equiv -p/m$),	-
\hat{n}	Unitary normal vector,	-
N	Interphase heat transfer parameter, Eq. (3.5),	-
N_0	Modified interphase heat transfer parameter ($\equiv N/\Gamma$),	-
N_{ε}	Porous-media-flame number,	-
NTU	Number of transfer units,	-
p	Pressure,	Pa
Q	Heat of reaction,	J kg^{-1}
$\dot{\mathbf{q}}$	Heat flux,	W m^{-2}
R_u	Universal gas constant,	$\text{J}(\text{mol K})^{-1}$
\dot{r}	Molar reaction rate,	$\text{mol m}^{-3} \text{s}^{-1}$
s_F	Flame speed defined in the cold side of the flame,	m s^{-1}
\dot{s}	Source term,	W m^{-3}
T	Temperature,	K
T_H	Excess temperature ($\equiv T_{sup} - T_r$),	K
t	Time,	s
u	Gas velocity,	m s^{-1}
V	Volume,	m^3
$v_{i,diff}$	Diffusion velocity of species i,	m s^{-1}
x	Spatial coordinate,	m
X_i	Molar fraction of species i,	-
\dot{w}	Reaction rate,	$\text{kg}(\text{m}^3 \text{s})^{-1}$
Y	Mass fraction,	-
y	Dimensionless mass fraction,	-

Greek Symbols

α	Dimensionless heat release ($\equiv (T_r - T_n)/T_r$),	-
β	Zel'dovich number ($\equiv E_a(T_r - T_n)/R_u T_r^2$),	-
β'	Modified Zel'dovich number ($\equiv E_a(T_r - T_n)/R_u T_{\text{sup}}^2$),	-
Γ	Thermal conductivities ratio ($\equiv \lambda_s/\lambda_g$),	-
δ	Non-dimensional reaction region thickness ($\equiv l_R/l_G$),	-
ε	Volumetric porosity,	-
ϕ	Equivalence ratio ($\equiv \nu Y_{F,n}/Y_{O,n}$),	-
Φ	Phase function for scattering radiation,	-
ζ	Dimensionless spatial coordinate of the $O(1)$ problem,	-
η	Dimensionless spatial coordinate of the $O(\delta\Gamma^{-1})$ problem,	-
η_{rec}	Heat recirculation efficiency,	-
θ	Dimensionless temperature,	-
κ	Optical thickness,	-
λ	Thermal conductivity,	W(m K)^{-1}
μ	Dynamic viscosity,	kg(m s)^{-1}
ν	Stoichiometric mass of oxygen per mass of fuel ratio,	-
ξ	Spatial coordinate of the $O(\Gamma^{-1})$ problem,	-
ρ	Gas density,	kg m^{-3}
$\sigma_{\lambda,a}$	Absorption coefficient,	m^{-1}
$\sigma_{\lambda,s}$	Scattering coefficient,	m^{-1}
σ_{SB}	Stefan-Boltzmann constant,	$\text{W m}^{-2} \text{K}^{-4}$

Subscripts

D	Darcean
d	Pore diameter
e	effective
F	Fuel
f	Flame
g	Gas
gs	Interfacial
G	Gas-phase diffusion length-scale
n	Non-reacted
m	Massic
O	Oxidant
p	pore
r	Reacted
R	Reaction length-scale
REV	Representative elementary volume
s	Solid
S	Solid-phase diffusion length-scale
sup	Superadiabatic
θ	Thermal energy

Superscripts

- 0 Free flame
- (0) Leading order term
- (1) First correction term
- (*) Second preheating region
- + Downstream from the flame
- Upstream from the flame
- ' Spatial deviation
- d* Dispersion

Other

- $\langle \rangle$ Volume-averaging
- $\langle \rangle^g$ Intrinsic gas-phase volume-averaging
- $\langle \rangle^s$ Intrinsic solid-phase volume-averaging
- $||$ Modulus

Chapter 1

Introduction

In this chapter, an introduction to the combustion in porous media and its applications is presented. Then, the difficulties for the numerical simulations of practical devices are discussed. Finally, the objectives of the thesis are stated and an overview of the monograph is given.

1.1 The combustion in porous media and its applications

The focus of this thesis is on the stationary adiabatic combustion of premixed gases within porous inert media. In these burners, the flame front stabilizes within the three-dimensional structure of interconnected cavities that forms the solid matrix. When compared to freely propagating flames, flames in porous media are characterized by the existence of an enhanced heat transfer from the hot region downstream from the flame to the cold region upstream from the flame due to a local form of heat recirculation. This characteristic has received much attention in the last decades as a way of extending flame stability and burning fuel lean mixtures [3, 4, 5].

The heat recirculation from the combustion products is broadly used in recuperative and regenerative burners to increase the flame temperature. Weinberg [6] and Lloyd and Weinberg [7] proposed original ways to control the amount of heat recirculated to the incoming reactants and, consequently, the flame temperature. With a thermodynamic model, Hardesty and Weinberg [8] showed that the amount of heat provided by the heat recirculation produces an excess enthalpy at the flame, which in turn extends the flammability limits of the fuel and increases the combustion rate. In an experimental study, they used a burner with an integrated counter-flow heat exchanger between the combustion products and the incoming air. This burner was able to burn mixtures of very low heat content, showing that the excess enthalpy allows the stabilization of flames that would not burn otherwise. They also showed that the maximum flame temperature exhibited by these flames is not determined by the reactants stoichiometry only, but also by the amount of heat recirculated.

Takeno and Sato [9] demonstrated numerically that the insertion of a porous medium in the flame region recreates Weinberg's conditions to recirculate the heat from the outgoing hot combustion products to the incoming fresh reactants and produces excess enthalpy flames. They showed that in these systems the heat recirculation induced by the porous medium adds to the heat released by combustion resulting in local temperatures in excess of the adiabatic flame limit based on the initial conditions of the mixture. This has been called superadiabatic combustion [10]. It is important to note that this recirculation of heat differs from the conventional recuperation of heat from the combustion products as proposed by Weinberg and his co-workers. In flames within porous media, the heat recirculation occurs at the flame scale and no external heat transfer devices are required.

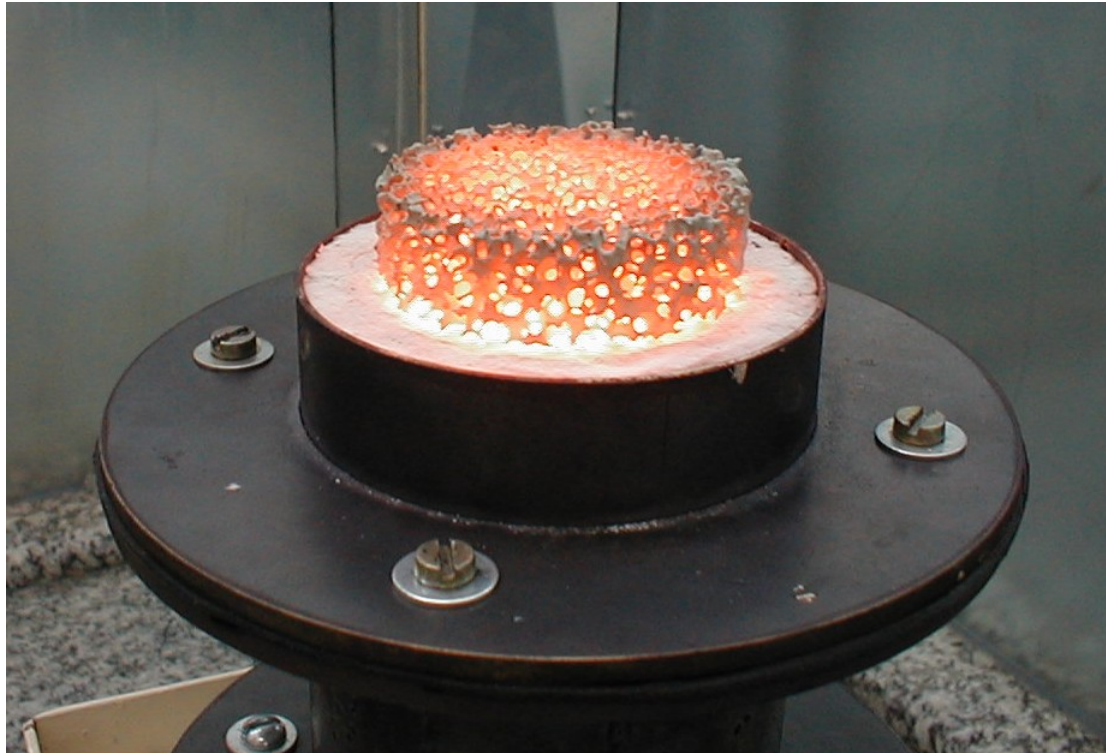


Figure 1.1: SiC foam porous burner [1].

Figure 1.1 shows a picture of a porous burner made of SiC foam in operation with the reactants flowing upward. The flame is not visible since it is stabilized within the porous matrix. The hot solid-phase loses heat to the surroundings by thermal radiation.

Figure 1.2 shows a scheme of the working principle of the steady-state combustion in a porous inert medium with heat losses at the ends. The gas-phase enters the porous medium and is preheated by the hot solid-phase. At the flame position, the gas-phase temperature increases steeply due to the heat released by the combustion reactions, reaching its maximum value. From this point ahead the gas-phase is hotter than the solid-phase and the surface convection heat transfer is established from the

gas-phase to the solid-phase. As a consequence of the temperature gradient across the solid-phase, heat is recirculated from the hot side of the solid matrix to its cold side by the solid-phase conduction and intramedium radiation. As a result of this local recirculation of heat, the flame temperature may exceed the adiabatic limit.

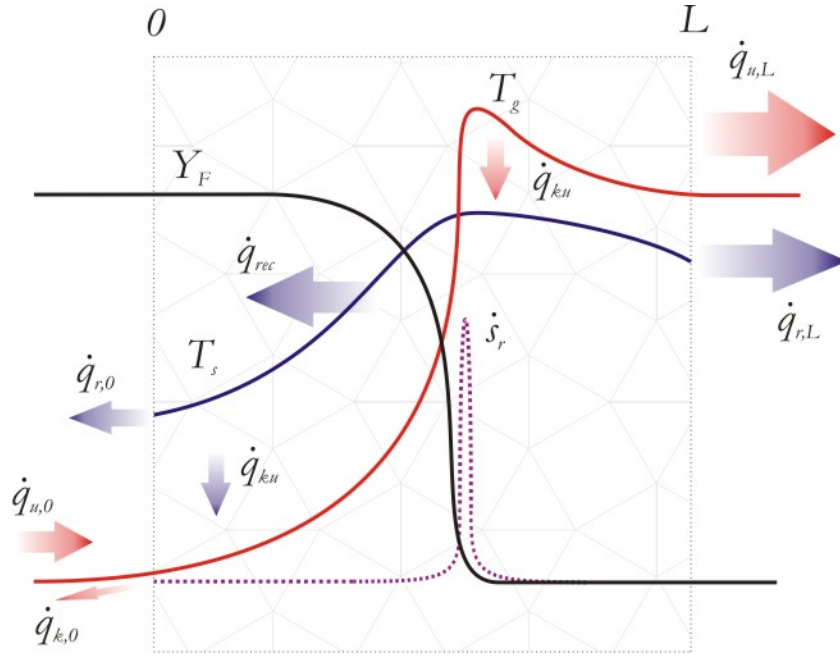


Figure 1.2: Gas-phase (T_g) and solid-phase (T_s) temperatures and mass fraction of fuel (Y_F) distributions for the steady-state combustion in a porous inert medium with heat losses at the ends. The heat fluxes \dot{q}_u , \dot{q}_k and \dot{q}_r are respectively the convection, conduction and radiation heat fluxes, \dot{q}_{ku} is the interphase heat transfer (surface convection), \dot{q}_{rec} is the heat recirculation, which includes the conduction and radiation through the solid-phase, and \dot{s}_r is the reaction energy conversion.

Since the pioneer work of Takeno and Sato [9], many researchers have turned their attention to the field of combustion in porous inert media. Experimental and numerical investigations were performed covering a variety of aspects. The experimental works aimed to characterize the operation of surface and volumetric burners in terms of the flame stability, turn-down-ratio, pollutants emission and flammability

limits [11, 12, 13, 14, 15, 16, 17]. Howell et al. [3] provide a longer list of earlier references. The measurement of the local thermal non-equilibrium between the phases is a problem particularly difficult to deal with because of the access restrictions to sensor probes within the solid matrix, the influence of the radiation field in the local temperature measurements and the possible catalytic reactions that may occur at the sensor surface. Some authors have proposed strategies to overcome these difficulties [12, 15], reaching limited success. Recently, the first optical measurement of temperature and species in a porous medium burner has been reported [18]. Nevertheless, the perspectives of this technique are still restricted to specific matrixes in which the structure permits optical access. Finally, some studies have also focused on the determination of transport properties for materials and conditions of interest to combustion in porous media such as effective thermal conductivity [19, 20], surface convection coefficient [21, 22] and radiant properties [23]. The numerical investigations are reviewed in the next section.

As a consequence of its modified flame structure, the combustion in porous media has several advantages over the free-flame combustion. The high temperatures at the reaction region lead to high reaction rates and, consequently, high flame speeds and high densities of energy release, allowing for the development of small burners. The elevated temperatures at the reaction region also permit the combustion of fuels of low heat content or mixtures that are under the standard lean flammability limit, i.e., the combustion of fuels and mixtures that otherwise would not be flammable. The high temperatures also lead to high efficiencies in the conversion of the reactants to saturated products, reducing the emissions of CO and unburned hydrocarbons. For very lean mixtures, the flame temperatures are low enough to prevent NO_x formation.

Furthermore, the increase in the flame speed also reduces the residence time in the hotter regions of the flame, reducing the NO_X emissions even for near-stoichiometric mixtures [14]. The solid matrix enhances the thermal inertia of the burner, making it less sensitive to fuel feed fluctuations. Finally, the hot solid matrix can enhance the heat transfer by radiation between the burner and the load. The heat transfer by radiation can provide much faster heating times than the surface convection heat transfer because it depends on the fourth power of the temperature of the burner and the load and is not limited by a thermal boundary layer. Then, the use of porous radiant burners can speed-up the processes that depend primarily on surface heat transfer, for example, reducing the necessary length of industrial kilns and dryers.

These attractive characteristics lead to the development of several industrial and domestic applications. Compact boilers with high efficiencies were developed based on the combustion in porous media (CPM) technology [24, 25]. Units, comprising burner and heat exchanger, of the order of 10-15 times smaller than the existing free-flame based units were reported. The high power density of flames in porous media have led to the development of compact heating systems for household applications [24, 26]. The high power modulation range of these burners makes them adequate to deal with the discrepancies between the power requirement of environment heating and hot water production. This characteristic avoids the need of several burner start-up and warm-up periods during the day, where the highest emissions occur.

The need of using fuels of low heat content had also led to the development of applications of the CPM technology. The rising cost of oil and the tendency of substituting fossil-fuels by renewable sources is increasing the interest in gas fuels generated by pyrolysis processes of many sources (coal, organic waste, biomass etc.),

which are known as syngas (synthetic gas), and gases emitted by landfills. The syngas may be composed by CO , H_2 and CH_4 diluted in a mixture of N_2 , CO_2 and H_2O , whereas municipal waste landfills emit mainly CO_2 and CH_4 . In all these cases the proportion between the constituents of the mixture may vary strongly depending on the source. If the fuel is very diluted with inert gases, the lean mixtures formed represent a challenge for conventional free-flame burners due to the low flame temperatures and poor flame stability. Numerical and experimental studies show that the combustion in porous media is a suitable technical solution to this application because of its ability to burn lean mixtures, to its wide power turn-down-ratio and improved flame stability [27, 28].

The study of liquid fuel combustion in porous inert media has also been addressed [29, 30, 31]. In general, these studies have been concerned with a dispersion of liquid fuel droplets suspended in air within the porous media. In this case, the three-dimensional structure of interconnected cavities of the solid matrix provides a radiation field that enhances the liquid vaporization, leading to high power loads.

Radiant porous burners are probably the most widespread devices based in the CPM technology. In these burners, the flame is stabilized at the surface of the porous matrix (surface burners) or within the matrix (volumetric burners). The hot solid-phase exchanges energy with the surrounding environment through radiation heat transfer. These burners found applications in paper and wood drying, powder coating, plastic curing and forming and food browning and baking [1, 3].

Surface burners are suited to the development of ultra-low NO_x burners. When these burners operate in the radiant mode, the flame is stabilized at the surface of the burner. The surface heat loss to the surroundings cools the flame and lowers the

NO_x emissions [32]. The conversion efficiency of CO and HC can be kept high, even at low flame temperatures, with the addition of catalytic particles to the solid matrix [33, 34]. The porous matrix is an appropriate substrate to catalytic particles since, in general, it has a large surface area to volume ratio (m^2/m^3).

The more general case of traveling combustion waves through porous media is known as filtration combustion (FC). Based on this process, efficient boilers were developed using the concept of reciprocating combustion [35]. In these boilers, the flow is reversed periodically, enhancing the heat recuperation of the device. Studies of filtration combustion in porous inert media show that a proper flow rate can lead to an overlap of the combustion and thermal waves, which in turn leads to extremely high excess temperatures at the reaction region [36, 37]. In these cases, ultra-lean mixtures ($\phi \sim 0.1$) become flammable.

Hydrogen production through partial oxidation within porous inert media has been investigated in experimental and numerical studies of forward filtration combustion [38, 39]. The high superadiabatic temperatures reached in these burners are adequate to the thermal cracking and partial oxidation of fuel rich mixtures.

Mujeebu and co-workers [40, 41, 42] and Mößbauer et al. [26] discuss several devices where combustion in porous medium is employed, including gas turbine and propulsion, thermoelectric conversion, powder combustion, highly polluting volatile organic components (VOC) oxidation, micro and meso-scale applications, air-heating systems for dryers, compact heating systems for cars, lightning and HCl synthesis.

The numerical simulation of practical devices, like those discussed above, presents several challenges. In the next section, some difficulties of numerical simulations of realistic devices are discussed with special attention devoted to radiant burners

applications.

1.2 Challenges for the numerical simulation.

Computational models for the simulation of combustion in porous media require the simultaneous solutions of chemical kinetics, mass, thermal energy and momentum equations. The multi-scale nature of the combustion process imposes difficulties in solving these equations because the reactions take place in a characteristic length scale that is much thinner than the characteristic length scale of the thermally affected region in the porous matrix. The mesh resolution required to solve the reaction region is much more restrictive than that to solve the large-scale problem. Local mesh refinement at the flame can reduce the computational demand, but complex adaptive algorithms to track the flame front are needed. Regarding the kinetic mechanism, an open question that still remains is the proper temperatures and concentrations that should be used to evaluate the reaction rates, since the volume-averaged values of these variables are valid approximations just for small departures from equilibrium [4].

Numerical works, in general, are based on one-dimensional homogeneous models (volume-averaged), and aim to understand the flame stabilization mechanisms, the influence of transport properties and chemical kinetics on the flame structure, transient behaviors and many other aspects [43, 44, 45, 46, 47, 48]. Multidimensional simulations were reported [49, 50], but in these cases the computational effort is a limiting aspect. Direct simulations are also found, but their application is restricted to simplified geometries [44, 51].

When dealing with engineering applications, such in radiant burners, some additional difficulties may arise. Each application requires different solutions in terms of power, operational temperature and burner shape. The burner must be designed to operate under the matrix maximum operational temperature to prevent matrix degradation. Intense gradients should be avoided in ceramic foam burners to increase the matrix durability [52]. The stability range and radiant efficiency of these burners depend on the burner configuration and the heat losses, then, the flame behavior under each operational condition changes. As a consequence, it is necessary to introduce new burner designs to face different applications.

One example of the possible complexities that can arise from the applications is the use of multiple discrete injection points of the reactant mixture at the inlet surface of radiant porous burners. This configuration creates a combined thermal and fluidynamic mechanism of flame stabilization, leading to an enlarged stability range which is specially interesting when burners with large superficial area are needed [2]. In these burners, at each injection point is associated a cone like flame configuration similar to the one observed in [50]. These multiple individual flames can merge depending on the operational conditions. Figures 1.3 and 1.4 show respectively a photograph and infrared image of a 15 cm x 15 cm radiant burner with 11 points of injection distributed in the inlet surface of the burner [2]. The injection points are clearly seen as brighter spots. This solution permits the development of a variety of burner configurations, aiming at surface homogeneity of temperature or staged power supply.

Then, the multiple scale nature of the problem, the stiffness and nonlinearity of the chemical reaction terms, combined with the nonlinearity of the flow in porous

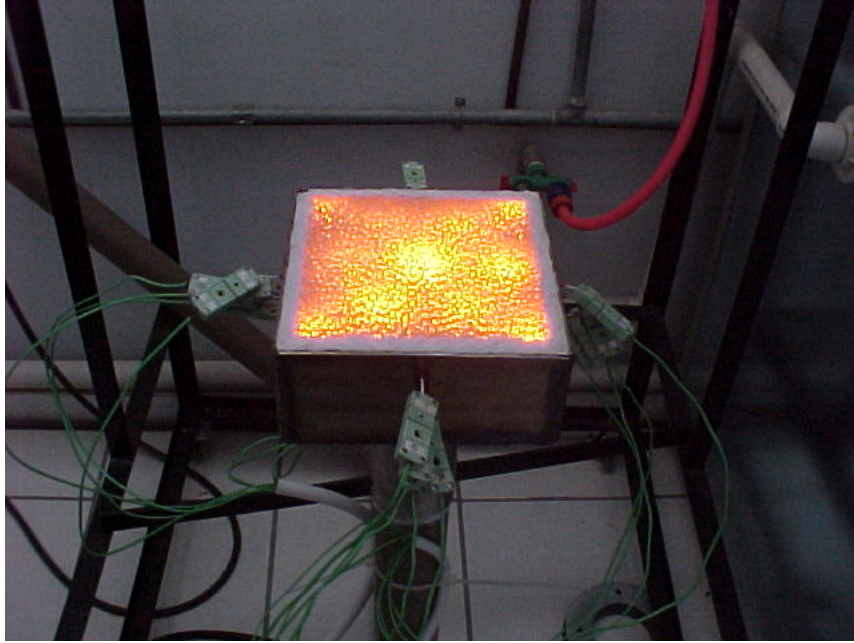


Figure 1.3: Porous radiant burner with multiple injections [2].

media and the 3D geometries involved, bring difficulties in building useful design tools to the development of new burners because of the large computational effort involved. Simplified models that could predict the most important thermal aspects of the combustion within porous media, with reduced computational effort, would be of great interest for engineering applications.

Researchers have focused their attention on developing new schemes to solve freely propagating premixed flames in a less expensive way than the traditional approach of solving the entire set of conservation equations. For example, the level-set approach based on the G -equation with a modeled turbulent flame velocity has been used to describe turbulent premixed combustion in the flamelet regime [53, 54]. In these models the flame inner structure is not solved explicitly and all information of the reaction scale is grouped in the flame velocity expression. An alternative approach to include

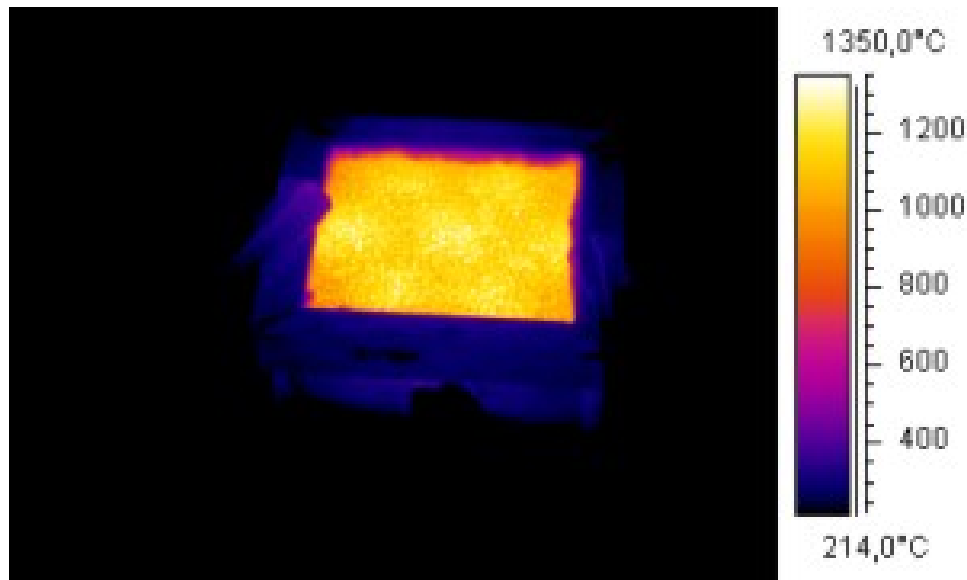


Figure 1.4: Infrared thermographic image of a porous radiant burner with multiple injections [2].

detailed kinetics is presented in [55, 56]. In this model (flamelet-generated-manifold - FGM) a higher dimensional flame is considered as an ensemble of one-dimensional flames. The results of the simulations of the 1D flamelet equations are parameterized and stored in a manifold that is accessed in the course of the multidimensional flame calculations. This technique has been applied to solve for the 3D gas flow and reaction above a surface radiant porous burner in a confined ambient [57].

The use of the level-set method with the G -equation in combination with an analytical expression for the flame velocity could be an interesting way of predicting the main thermal aspects of the combustion in porous media and of building a useful design tool for porous burners with complex three-dimensional shapes. The idea is to use a macroscopic volume-averaged model to describe the problem of heat transfer between the gas and solid phases at the largest scale (macroscale model) and a

subgrid model for the local flame consumption speed (microscale model) as a form of multiscale treatment for reaction in porous media [58].

1.3 Objectives

The objective of this thesis is to develop a model for multidimensional numerical simulations of premixed flames within porous inert media capable of capturing the main thermal characteristics of the processes with an associated low computational cost.

This general objective will be divided in two partial objectives:

1. To analyze the premixed flame structure in porous inert media with the aim of identifying possible simplifications for the inner scales of the problem.
2. To develop a level-set treatment for the simulation of flow and reaction in porous media based on a subgrid model for these inner scales.

1.4 Organization of the manuscript

Chapter 2 presents the problem formulation for reacting flows within porous inert media, discusses its main difficulties and proposes simplifications to allow the analytic treatment.

Chapters 3 to 5 are devoted to the analytical study of the structure of lean stationary adiabatic planar premixed flames within porous inert media, covering a wide range of equivalence ratios. Chapter 3 deals with an asymptotic solution for the combustion of near-stoichiometric mixtures, where high flame velocities are found

and where the interphase heat transfer at the inner scales of the problem can be neglected. This study has been published recently [59]. Chapter 4 is devoted to ultra-lean mixtures with low flame velocities, where the interphase heat transfer at an intermediate scale can not be neglected, and reveals the lean flammability limit for premixed combustion in porous inert media. Finally, Chapter 5 uses an alternative formulation of the conservation equations through the excess enthalpy function and reveals a limit for the superadiabatic effect. This study has been presented partially at the 12th Brazilian Congress of Thermal Engineering and Sciences November 10-14, 2008, Belo Horizonte, MG.

Chapter 6 is devoted to the construction of a level-set model for multidimensional numerical simulations of porous burners. The flame velocity expression found in the theoretical analysis is adapted as a subgrid model for the flame propagation in porous media and is used in conjunction with the G -equation (level-set method) to model the flame surface movement.

Finally, in Chapter 7, the main conclusions are summarized followed by recommendations for future works.

Chapter 2

Problem formulation

In this chapter, the volume averaging method is employed to obtain the homogeneous conservation equations for the problem of a reactive gas-phase flowing through a stationary inert solid-phase. Questions concerning the applicability of the model to the problem of combustion in porous inert media are discussed and simplifying hypothesis are assumed.

2.1 Local problem

Consider a mixture of reacting gases flowing through the interstices of a solid stationary matrix as shown in figure 2.1. The solid-phase is chemically inert and impermeable to the fluid-phase. The conservation of the total mass of the gas-phase reads

$$\frac{\partial \rho_g}{\partial t} + \nabla \cdot (\rho_g \mathbf{u}) = 0, \quad (2.1)$$

where ρ_g is the gas-phase density and \mathbf{u} is the gas-phase velocity vector. The conservation of mass of the chemical species, assuming the validity of the Fick's law [60, 61],

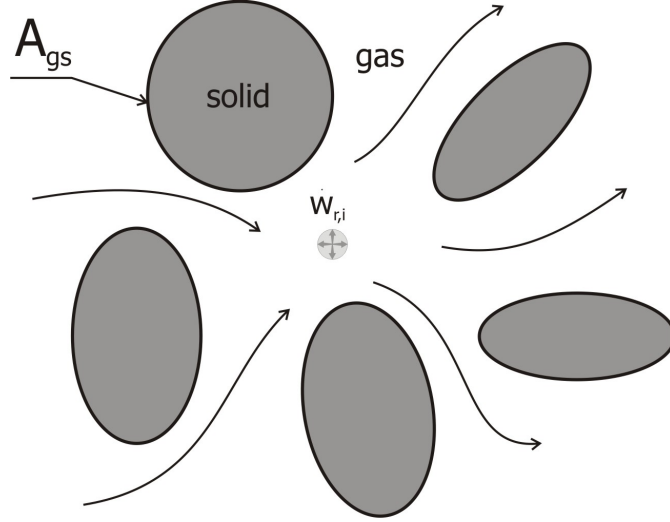


Figure 2.1: The local problem of a reacting fluid-phase flowing through a stationary inert solid-phase.

reads

$$\rho_g \frac{\partial Y_i}{\partial t} + \rho_g \mathbf{u} \cdot \nabla Y_i = \nabla \cdot (\rho_g D_{im} \nabla Y_i) + \dot{w}_{r,i}, \quad (2.2)$$

where Y_i is the mass fraction of the chemical species i , $D_{i,m}$ is the mass diffusivity of the species i into the mixture and $\dot{w}_{r,i}$ is the homogeneous volumetric rate of reaction of species i . The thermal mass diffusion (Soret effect) is neglected.

The energy conservation equations for the solid and gas phases are written assuming Fourier's law of heat conduction. For the gas-phase we have

$$(\rho c_p)_g \frac{\partial T_g}{\partial t} + (\rho c_p)_g \mathbf{u} \cdot \nabla T_g = \nabla \cdot (\lambda_g \nabla T_g) - \sum_{i=1}^{N_s} \rho_g Y_i c_{p,i} v_{i,diff} \cdot \nabla T_g - \sum_{i=1}^{N_s} h_i \dot{w}_{r,i}, \quad (2.3)$$

where T_g is the gas-phase temperature, $c_{p,g}$ is the specific heat at constant pressure for the gas-phase, λ_g is the molecular thermal conductivity of the gas-phase, N_s is the number of chemical species, $c_{p,i}$ is the specific heat at constant pressure of

species i , $v_{i,diff}$ is the diffusion velocity of species i in the mixture, which is given by $v_{i,diff} = -(D_{im}/Y_i)\nabla Y_i$ and h_i is the specific enthalpy of species i . The kinetic energy and viscous dissipation heating are neglected. The gas-phase radiation is, in general, negligible when compared to the solid-phase radiation. For the solid-phase we have

$$(\rho c_p)_s \frac{\partial T_s}{\partial t} = \nabla \cdot (\lambda_s \nabla T_s), \quad (2.4)$$

where T_s is solid-phase temperature, $(\rho c_p)_s$ is the product of the density and specific heat at constant pressure for the solid-phase and λ_s is the molecular thermal conductivity of the solid-phase.

The momentum conservation equation (Navier-Stokes) for a compressible flow is [62]

$$\rho_g \left(\frac{\partial \mathbf{u}}{\partial t} + \mathbf{u} \cdot \nabla \mathbf{u} \right) = \rho_g \mathbf{f} - \nabla p + \nabla (\lambda \nabla \cdot \mathbf{u}) + \nabla \cdot \left\{ \mu \left[\nabla \mathbf{u} + (\nabla \mathbf{u})^T \right] \right\}, \quad (2.5)$$

where \mathbf{f} is a body force, p is the thermodynamic pressure, μ is the dynamic viscosity of the gas-phase, λ is the second coefficient of viscosity and $(\nabla \mathbf{u})^T$ is the transpose of the tensor $\nabla \mathbf{u}$.

For closure, the ideal gas equation is used

$$p = \frac{R_u}{M_g} \rho_g T_g, \quad (2.6)$$

where R_u is the universal gas constant and M_g is the mixture molar mass ($M_g = \sum_{i=1}^N X_i M_i$, where X_i and M_i are respectively the molar fraction and molar mass of species i).

The boundary conditions at the interface (A_{gs}) between the solid and gas phases are: (1) impermeable solid with no surface reactions and no-slip conditions,

$$-\rho_g D_{i,j} \nabla Y_i = 0 \quad \text{and} \quad \mathbf{u} = 0 \quad \text{on} \quad A_{gs}, \quad (2.7)$$

and (2) continuity of temperature and heat flux

$$T_g = T_s \quad \text{and} \quad \lambda_g \nabla T_g \cdot \hat{n}_{gs} = (-\lambda_s \nabla T_s - \dot{\mathbf{q}}_{r,s}) \cdot \hat{n}_{sg} \quad \text{on} \quad A_{gs}, \quad (2.8)$$

where \hat{n}_{gs} is the unitary normal vector on A_{gs} pointing to the solid-phase ($\hat{n}_{gs} = -\hat{n}_{sg}$ on A_{gs}) and $\dot{\mathbf{q}}_{r,s}$ is the radiant heat flux at the solid surface, that is due to the radiation exchange between solid surfaces. The gas-phase radiation at the pore-scale is neglected.

The solution of this entire set of equations requires the description of the geometric details of the solid matrix in a direct numerical simulation. This approach represents a tremendous computational effort that is impractical, except for periodic structures. The method of volume averaging can reduce this problem to a macroscopic description of an homogeneous medium with effective properties that is more easily solved. On the other hand, this method requires some conditions for its validity that will be discussed in the next section.

2.2 Volume averaging method

In this method, the conservation equations are volume-averaged over a representative elementary volume (REV), i.e., the smallest volume that represents the local average properties. Thus, a small increase in the REV does not change the averaged properties. Figure 2.2 shows a rendering of the representative elementary volume and the position vectors. Any point in the domain can be located by the position vector $\vec{\mathbf{r}}$ in respect to the global coordinate system. Then, we can define a volume of integration (REV) with geometric center (GC) located by an arbitrary position vector $\vec{\mathbf{x}}$. Now, any point inside the REV can be located by the local position vector $\vec{\mathbf{y}}$ in respect to

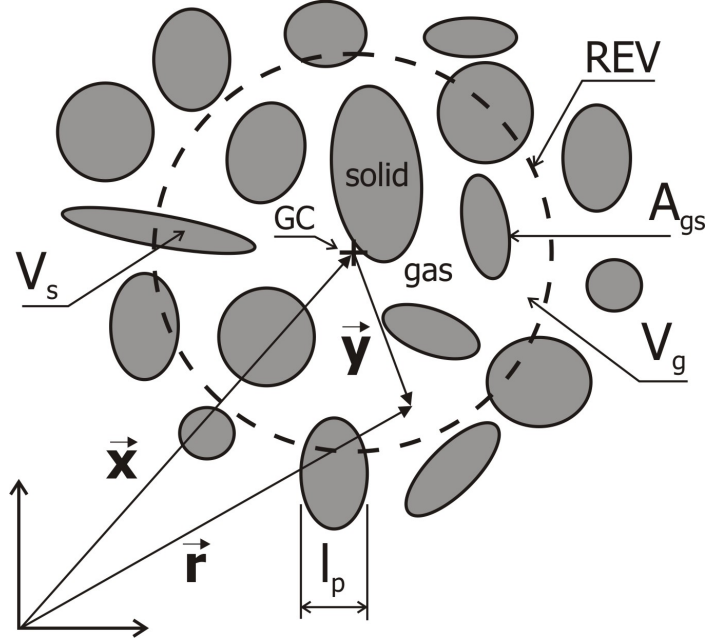


Figure 2.2: The representative elementary volume and position vectors

GC. The idea of the method is to average the property of interest in the REV, using the local coordinate system \vec{y} (microscopic coordinate), and to relate the result to the general coordinate system \vec{x} (macroscopic coordinate).

The volume average of a property ϕ is defined as [63]

$$\langle \phi \rangle = \frac{1}{V} \int_V \phi dV, \quad (2.9)$$

where V is the volume of the REV and $\langle \rangle$ denotes the volume averaging. The porosity of the matrix ε is defined as

$$\varepsilon = \frac{V_g}{V} = \frac{V_g}{V_g + V_s}, \quad (2.10)$$

where V_g and V_s are the gas- and solid-phase volumes inside the REV. Then, the average of a gas-phase property ϕ_g over the gas-phase volume (gas-phase intrinsic

volume average) is

$$\langle \phi_g \rangle^g = \frac{1}{V_g} \int_{V_g} \phi_g dV = \langle \phi_g \rangle / \varepsilon. \quad (2.11)$$

The theorem of the intrinsic volume-averaging of the gradient of a function ϕ_g is

$$\langle \nabla \phi_g \rangle^g = \nabla \langle \phi_g \rangle^g + \frac{1}{V_g} \int_{A_{gs}} \phi_g dA. \quad (2.12)$$

Analogously, the theorem of the intrinsic volume-averaging of the divergent of a vector \mathbf{b}_g is

$$\langle \nabla \cdot \mathbf{b}_g \rangle^g = \nabla \cdot \langle \mathbf{b}_g \rangle^g + \frac{1}{V_g} \int_{A_{gs}} \mathbf{b}_g \cdot \hat{n}_{gs} dA. \quad (2.13)$$

Central to the volume averaging method is the requirement of scales separation, which can be stated as

$$l_p \ll l_{REV} \ll L, \quad (2.14)$$

where l_p is the pore characteristic length-scale, l_{REV} is the characteristic length-scale of the REV and L is the largest characteristic length-scale of the problem. This prevents the analysis of thin media for which boundary effects are as important as bulk effects. Also, phenomenological scales have to be separated. For example, for conduction heat transfer, it is required that

$$\Delta T_{l_p} \ll \Delta T_{l_{REV}} \ll \Delta T_L, \quad (2.15)$$

where ΔT represents the maximum temperature difference across the respective length-scale. This condition represents a severe limitation to the volume-averaging modelling of combustion in porous media. It is usually not possible to define a REV that fulfils the separation of scales requirement since flames are characterized by a narrow region where the fuel is consumed and the chemical energy is released (the flame thickness) that is often of the order of a fraction of the length-scale of a single pore, which means that the leftmost inequality in equation (2.15) is violated.

A comparison between the direct simulation (2D) and the volume-averaged models for the combustion in porous media is presented by Sahraoui and Kaviany [44]. The two-dimensional results show that multiple flame velocities exist as the flame is displaced within a pore, a behavior not predicted by homogeneous models. Additionally, the flame temperature is under-predicted by the volume-averaged model. More details on the interaction of the flame with the pore walls at the pore level are found in Hackert et al.[51] and Daou and Matalon [64].

Nevertheless, if one assumes the validity of the volume-averaged model, the method proceeds with taking the volume average of the conservation equations (2.1) to (2.7) and applying successively the averaging theorems. For the total mass conservation equation, the application of the volume averaging gives

$$\left\langle \frac{\partial \rho_g}{\partial t} \right\rangle^g + \nabla \cdot \langle \rho_g \mathbf{u} \rangle^g = -\frac{1}{V_g} \int_{A_{gs}} \rho_g \mathbf{u} \cdot \hat{n}_{gs} dA. \quad (2.16)$$

Applying the Reynolds transport theorem to the transient term and using the impermeability and non-slip condition at A_{gs} the result is

$$\frac{\partial \langle \rho_g \rangle^g}{\partial t} + \nabla \cdot \langle \rho_g \mathbf{u} \rangle^g = 0. \quad (2.17)$$

Proceeding in the same way for the energy and species conservation equations, difficulties arise because of the additional unknowns introduced by the method (terms inside the area integrals). To treat these terms spatial decompositions are proposed for the variables in the form

$$\phi_g = \langle \phi_g \rangle^g + \phi'_g, \quad (2.18)$$

where the ϕ'_g is a local spatial deviation from the intrinsic phase-averaged value $\langle \phi_g \rangle^g$. The problem is closed proposing a set of closure constitutive equations that, in general,

relate the local deviation of the variable to the gradient of its average

$$\phi'_g = \mathbf{b}(x) \cdot \nabla \langle \phi_g \rangle^g, \quad (2.19)$$

where $\mathbf{b}(x)$ is a vector function. For the two-medium model described here, these closure constitutive equations include the effect of the gradients of the phase-averaged temperatures of both phases as well as the differences in the phase-averaged temperatures of the phases [63]. Then, the several unknowns of the problem are grouped in effective coefficients that have to be modeled. As an example, the volume-averaged gas-phase energy equation obtained for the two-medium treatment is

$$\begin{aligned} \frac{\partial \langle T_g \rangle^g}{\partial t} + \mathbf{v}_{gg} \cdot \nabla \langle T_g \rangle^g + \mathbf{v}_{gs} \cdot \nabla \langle T_s \rangle^s = \nabla \cdot \mathbf{D}_{gg} \cdot \nabla \langle T_g \rangle^g + \nabla \cdot \mathbf{D}_{gs} \cdot \nabla \langle T_s \rangle^s \\ + \frac{A_{gs}}{V_g} \frac{h_c}{(\rho c_p)_g} (\langle T_s \rangle^s - \langle T_g \rangle^g) + \langle \dot{s}_r \rangle^g, \end{aligned} \quad (2.20)$$

where the convective velocity vectors \mathbf{v}_{gg} and \mathbf{v}_{gs} are the coefficients of the terms containing the first-order derivatives, the total thermal diffusivity tensors \mathbf{D}_{gg} and \mathbf{D}_{gs} are the coefficients of the terms containing second-order derivatives, h_c is the interfacial conduction heat transfer coefficient, that is independent from the fluid velocity, and $\langle \dot{s}_r \rangle^g$ is an energy source term. The equation for the solid-phase energy is similarly obtained. Note that many cross terms between the solid- and gas-phase energy equations exist. The coefficients appearing in Eq. (2.20) are to be obtained from the solution of the closure problem.

Equations for the transformation vectors (and scalars, in the case of the two-equation model) are obtained and numerical solutions for the closure problems are proposed by some authors [65, 66]. These solutions are based on direct numerical simulations for idealized periodic structures. The results show the behavior of the

effective coefficients which can be parameterized and used in the volume-averaged conservation equations.

The derivation of the volume-averaged momentum conservation equation in a form equivalent to the Navier-Stokes equation is still an open problem. Some simplified forms are proposed in the literature [63].

As a result of the volume-averaging method, it is possible to arise at a set of volume-averaged conservation equations that describes the problem of a reacting flow through a stationary solid matrix. Nevertheless, data of the entire set of effective coefficients is very limited and the resulting equations are still too difficult to solve for engineering problems. To deal with these difficulties, semi-heuristic equations that rely on the volume average concepts but cannot be derived from first principles are proposed. These equations will be reviewed in the next section.

2.3 Semi-heuristic volume-averaged conservation equations

The volume-averaged conservation equations for the total mass, mass of species, gas-phase energy, solid-phase energy and momentum, based on semi-heuristic considerations and assuming uniform porosity, are presented below [44, 63, 67].

For the total mass conservation we have

$$\varepsilon \frac{\partial \langle \rho_g \rangle^g}{\partial t} + \varepsilon \nabla \cdot \langle \rho_g \rangle^g \langle \mathbf{u} \rangle^g = 0. \quad (2.21)$$

The species mass conservation equation reads

$$\varepsilon \langle \rho_g \rangle^g \frac{\partial \langle Y_i \rangle^g}{\partial t} + \varepsilon \langle \rho_g \rangle^g \langle \mathbf{u} \rangle^g \cdot \nabla \langle Y_i \rangle^g = \nabla \cdot \varepsilon \langle \rho_g \rangle^g (\langle \mathbf{D}_m \rangle_i^g + \langle \mathbf{D}_m^d \rangle_i^g) \cdot \nabla \langle Y_i \rangle^g - \varepsilon \langle \dot{w}_{r,i} \rangle^g, \quad (2.22)$$

where $\varepsilon \langle \mathbf{D}_m \rangle_i^g$ is the effective mass diffusivity tensor of species i and $\varepsilon \langle \mathbf{D}_m^d \rangle_i^g$ is the mass dispersion tensor of species i . Then, the effect of the porous medium on the conservation of species is included, first, in an effective diffusivity that may present anisotropic behavior and that depends on the solid matrix geometry and, second, via the dispersion tensor that is an enhancement of the diffusivity of the species due to the hydrodynamics of the local problem and is always anisotropic.

The gas-energy conservation equation is written as

$$\begin{aligned} \varepsilon \langle \rho_g \rangle^g c_{p,g} \frac{\partial \langle T_g \rangle^g}{\partial t} + \varepsilon \langle \rho_g \rangle^g c_{p,g} \langle \mathbf{u} \rangle^g \cdot \nabla \langle T_g \rangle^g = \nabla \cdot \varepsilon (\langle \lambda_g \rangle^g + \langle \rho_g \rangle^g c_{p,g} \langle \mathbf{D}^d \rangle^g) \cdot \nabla \langle T_g \rangle^g \\ - \sum_{i=1}^N \langle \rho_g \rangle^g \langle Y_i \rangle^g c_{p,i} \langle v_{i,diff} \rangle^g \cdot \nabla \langle T_g \rangle^g + \frac{A_{gs}}{V} h_{gs} (\langle T_s \rangle^s - \langle T_g \rangle^g) \\ - \varepsilon \sum_i^N h_i \langle \dot{w}_{r,i} \rangle^g, \quad (2.23) \end{aligned}$$

where $\varepsilon \langle \lambda_g \rangle^g$ is the effective thermal conductivity tensor of the gas-phase, $\langle \mathbf{D}^d \rangle^g$ is the thermal dispersion tensor and h_{gs} is the surface convective heat transfer coefficient. Again, the solid matrix introduces a geometric dependence in the effective thermal conductivity, leading to a tensorial description. The thermal dispersion enhances the thermal diffusivity of the media and is related to the matrix geometry and flow pattern of the local problem. Since non-equilibrium between the phases exists, the convection heat transfer effects are accounted for in a surface convection term based on h_{gs} . Rigorously, since there is energy generation in the gas phase, the average convective coefficient becomes a function of the strength of the local energy generation [44].

The solid phase conservation equation reads

$$(1 - \varepsilon) \langle \rho_s \rangle^s c_{p,s} \frac{\partial \langle T_s \rangle^s}{\partial t} = \nabla \cdot (1 - \varepsilon) \langle \lambda_s \rangle^s \cdot \nabla \langle T_s \rangle^s - \frac{A_{gs}}{V} h_{gs} (\langle T_s \rangle^s - \langle T_g \rangle^g) + \nabla \cdot \langle \dot{\mathbf{q}}_r \rangle, \quad (2.24)$$

where $(1 - \varepsilon) \langle \lambda_s \rangle^s$ is the effective thermal conductivity tensor of the solid-phase and $\langle \dot{\mathbf{q}}_r \rangle$ is the volume-averaged radiant heat flux.

Finally, the momentum conservation equation is written as

$$\frac{\langle \rho_g \rangle^g}{\varepsilon} \left(\frac{\partial \langle \mathbf{u} \rangle}{\partial t} + \langle \mathbf{u} \rangle \cdot \nabla \langle \mathbf{u} \rangle \right) = \langle \rho_g \rangle^g \mathbf{f} - \nabla \langle p \rangle^g + \frac{\mu}{\varepsilon} \nabla^2 \langle \mathbf{u} \rangle - \frac{\mu}{\mathbf{K}} \langle \mathbf{u} \rangle - \frac{C_E}{\mathbf{K}^{1/2}} \langle \rho_g \rangle^g |\langle \mathbf{u} \rangle| \langle \mathbf{u} \rangle, \quad (2.25)$$

where \mathbf{K} is the permeability tensor (a geometric property of the matrix) and C_E is the Ergun constant. The left hand side of Eq. (2.25) represents the macroscopic inertial forces. The first and second terms on the right hand side of Eq. (2.25) are respectively the pore pressure gradient and the body force. The third term is the macroscopic shear stress diffusion term (Brinkman viscous term), the fourth term is the microscopic viscous shear stress (Darcy term) and the fifth term is the microscopic inertial force (Ergun inertial term). When $\varepsilon \rightarrow 1$ ($\mathbf{K} \rightarrow \infty$) the macroscopic Navier-Stokes equation is recovered. Note, however, that the compressible effects were neglected in Eq. (2.25).

The ideal gas equation of state is

$$\langle p \rangle^g = \frac{R_u}{M_g} \langle \rho_g \rangle^g \langle T_g \rangle^g, \quad (2.26)$$

where the mixture molar mass is given by $M_g = \sum_1^{N_s} \langle X_i \rangle^g M_i$.

This set of equations is simpler than that obtained from the rigorous application of the volume average method to the local problem. Here, the effects of the many

coefficients that appear in the original equations are accounted for using fewer coefficients, namely the effective thermal conductivity tensors of both phases, the mass and thermal dispersion tensors of the moving phase and the superficial convection heat transfer coefficient. These coefficients have to be measured experimentally, which can be a difficult task since they are coupled in the two-energy equation model [65].

2.4 Reaction source term

In flames, the reaction region is characterized by the existence of several simultaneous elementary reactions [68]. For example consider the following elementary reaction



where the molecular oxygen (O_2) reacts with the atomic hydrogen radical (H) forming two new radicals, the hydroxyl (OH) and the atomic oxygen (O), in what is known as a branching step, i.e., one radical forming two radicals. The forward reaction rate \dot{r}_f is proportional to the reagents concentrations

$$\dot{r}_f = k_f [O_2] [H], \quad (2.27)$$

where the terms in brackets are molar concentrations ($[H] = \rho_g Y_H / M_H$, for example) and k_f is the forward reaction rate coefficient, which is usually written following an extended Arrhenius model

$$k_f = AT_g^a \exp\left(\frac{-E_a}{R_u T_g}\right), \quad (2.28)$$

where A is the pre-exponential factor, that is related to the collision frequency of the molecules, a is the temperature exponent and E_a is the activation energy required for the reaction to occur.

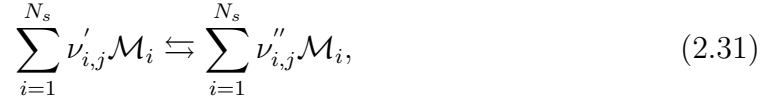
In general, the reactions are reversible and the reverse reaction rate \dot{r}_r is also included. Then, the net reaction rate for the elementary step under analysis is

$$\dot{r} = \dot{r}_f - \dot{r}_r = k_f [O_2][H] - k_r [OH][O], \quad (2.29)$$

where the reverse reaction rate is found through the equilibrium constant K_c [68]

$$K_c(p, T_g) = k_f/k_r. \quad (2.30)$$

Each elementary reaction can be written in the general form



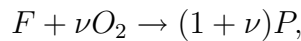
where $\nu_{i,j}$ is the number of moles of species i participating in the reaction j and \mathcal{M}_i represents the species i . Then, the reaction rate of the j^{th} reaction can be written as

$$\dot{r}_j = k_{f,j} \prod_{i=1}^{N_s} [\mathcal{M}_i]^{\nu'_{i,j}} - k_{r,j} \prod_{i=1}^{N_s} [\mathcal{M}_i]^{\nu''_{i,j}}. \quad (2.32)$$

Finally, the reaction source term appearing in Eqs. (2.2) and (2.3) include the contributions of all N_r elementary reaction steps

$$\dot{w}_{r,i} = M_i \sum_{j=1}^{N_r} \left(\nu''_{i,j} - \nu'_{i,j} \right) r_j. \quad (2.33)$$

Several degrees of detail can be employed in constructing a chemical kinetic mechanism. Reduced schemes based on global reaction steps are proposed to reproduce the main behavior of flames with reduced computational cost. In this sense, a common simplifying assumption is that the fuel combustion occurs following a global one-step irreversible mechanism, represented in mass units as



where ν is the stoichiometric mass of oxygen per mass of fuel ratio. Then, the fuel reaction rate can be written as

$$\dot{w}_{r,F} = -A\rho_g^2 T_g^a Y_F^n Y_O^m \exp\left(\frac{-E_a}{R_u T_g}\right), \quad (2.34)$$

where Y_F and Y_O are respectively the mass fraction of fuel and oxidant. This simple mechanism permits the adjustment of few parameters (a , A , n , m and E_a) to reproduce experimental results.

Detailed [47, 69, 70] and reduced [48, 32, 43] mechanisms were employed to the problem of premixed combustion in porous inert media. The results show that, for lean mixtures, the flame speed is less sensitive to the mechanism chosen, but the flame temperature is over-predicted when the one-step mechanism is used. A point that is an open question is the influence of the porous matrix on the reaction rates. The large specific superficial area of the matrix may act as a radical sink, reducing the reaction rates. To the author knowledge, no model in the literature considers this effect.

The intrinsic volume-averaged homogeneous reaction rates are also heuristically modeled in the works found in the literature. The average reaction rate is imposed to be equal to the reaction evaluated with the averaged variables. For example, the one-step mechanism of Eq. (2.34) is simply re-written as

$$\langle \dot{w}_{r,F} \rangle^g = -A (\langle \rho_g \rangle^g)^2 (\langle T_g \rangle^g)^a (\langle Y_F \rangle^g)^n (\langle Y_O \rangle^g)^m \exp\left(\frac{-E_a}{R_u \langle T_g \rangle^g}\right) \quad (2.35)$$

In the evaluation of Eq. (2.35), the use of the volume-averaged temperatures and concentrations is a valid approximation only for small departures from equilibrium [4]. In this sense, the use of detailed kinetic models is still a crude approximation regarding the effect of temperature on the reaction rates. This is still an open issue,

not completely solved.

2.5 Radiant source term

The effect of the radiation field within the solid matrix has been included in the solid-phase energy equation, Eq. (2.24), as the radiant heat flux $\langle \dot{\mathbf{q}}_r \rangle$. Then, the radiation heat transfer that affected the boundary condition in the local problem, Eq. (2.8), becomes an homogeneous treatment of a medium that emits, absorbs and scatters radiation, i.e., a participating medium.

The homogeneous treatment of the radiation in participating media requires the solution of the radiant transfer equation (RTE). This equation represents the variation of the radiant intensity in a generic direction s [63]

$$\begin{aligned} \frac{dI_\lambda}{ds} = & \langle \sigma_{\lambda,a} \rangle I_{\lambda,b} - (\langle \sigma_{\lambda,a} \rangle + \langle \sigma_{\lambda,s} \rangle) I_\lambda \\ & + \frac{\langle \sigma_{\lambda,s} \rangle}{2} \int_{-1}^1 I_\lambda(\theta_i) \langle \Phi_\lambda \rangle (\theta_i \rightarrow \theta) d\cos\theta_i, \end{aligned} \quad (2.36)$$

where I_λ is the spectral (λ) radiant intensity, i.e., the radiation energy in the direction θ per unit time, per unit projected area, per unit solid angle and per interval $d\lambda$ around the wavelength λ ($W/m^2 sr \mu m$), $I_{\lambda,b}$ is the spectral blackbody emitted intensity ($I_{\lambda,b} = E_{\lambda,b}/\pi$, where $E_{\lambda,b}$ is the spectral blackbody emissive power given by Plank's law for emission into vacuum), $\langle \sigma_{\lambda,a} \rangle$ and $\langle \sigma_{\lambda,s} \rangle$ are respectively the effective absorption and scattering coefficients ($1/m$), θ is the angle of propagation of the radiant beam (polar angle), θ_i is the angle of the in-scattering direction and $\langle \Phi_\lambda \rangle$ is a phase function that models the directional scattering behavior of the medium. In the above equation, azimuthal symmetry is assumed. Then, the first term on the right hand side of Eq. (2.36) is a gain in the radiant intensity due to emission, the second term represents

losses in the radiant intensity due to absorption and scattering and the last term is the gain in the radiant intensity due to the incident scattered radiation from all directions (θ_i) into the direction θ .

The radiant heat flux is found integrating the radiant intensity over all directions and wavelengths,

$$\langle \dot{\mathbf{q}}_r \rangle = 2\pi \int_0^\infty \int_{-1}^1 s I_\lambda d\cos\theta d\lambda. \quad (2.37)$$

For optically thick media (where the extinction coefficient $\langle \sigma_{\lambda,e} \rangle = \langle \sigma_{\lambda,a} \rangle + \langle \sigma_{\lambda,s} \rangle$ is large) a diffusion approximation can be proposed (Rosseland approximation [71, 72]). In this limit, the radiant flux is assumed to be dependent on the local temperature gradient only and a radiant conductivity can be defined as

$$\langle \dot{\mathbf{q}}_r \rangle = - (1 - \varepsilon) \left[\frac{16\sigma_{SB} (\langle T_s \rangle)^3}{3\langle \sigma_{\lambda,e} \rangle} \right] \nabla \langle T_s \rangle^s = - (1 - \varepsilon) \langle \lambda_r \rangle \nabla \langle T_s \rangle^s, \quad (2.38)$$

where σ_{SB} is the Stefan-Boltzmann constant and $\langle \lambda_r \rangle$ is the effective radiant conductivity of the solid-phase.

The Rosseland approximation is valid for small pores which often is not the case for the porous media used in porous burners. Siegel and Howell [71] suggest that this approximation is valid for $\kappa > 5$, with κ being the optical thickness of the medium. The optical thickness is equivalent to the ratio of the characteristic length of the system and the mean free-path l_m for the radiation ($l_m = 1/\langle \sigma_{\lambda,e} \rangle$). For the radiation heat transfer in a porous medium, the mean free-path can be estimated by $l_m = (l_d/3)/(1 - \varepsilon)$ [73], valid for pore diameters larger than 0.6 mm. The characteristic length of the system can be assumed to be equal to the thermally affected region around the flame l_T . Then, as an example, a ceramic foam with $\varepsilon = 80\%$ and $l_p = 2.0$ mm - and knowing that l_T is of the order of 30 mm [1] - we will have a reasonably

large optical thickness ($\kappa = 6$) and a radiant conductivity can be used as a first approximation to model the radiant heat transfer through the solid matrix.

2.6 Simplifying assumptions

In order to develop an analytic approximate solution for the problem of premixed flames within porous inert media some simplifying assumptions are required. Assuming a global one-step reaction mechanism, a steady-state one-dimensional two-medium model for the conservation of mass, gas-phase energy, solid-phase energy and mass of chemical species is written following Sahraoui and Kaviany [44]. For simplicity, the volume-averaging notation is omitted.

The mass conservation implies that $\rho_n u_n$ is constant for the one-dimensional flow, with ρ_n and u_n being respectively the gas density and the gas velocity far upstream from the flame. For a steady-state stationary flame, the laminar flame speed s_F is equal to u_n . The gas-phase specific heat capacity c_p , the effective thermal conductivities ($\varepsilon\lambda_g$ for the gas and $(1 - \varepsilon)\lambda_s$ for the solid) and the product $\rho\varepsilon D$ (gas-phase density times mass effective diffusivity) are assumed to be uniform along the flame. The effective thermal conductivity of the solid-phase includes the pore tortuosity and the intraphase radiation through a radiant conductivity (Rosseland approximation). The effective thermal conductivity and mass diffusivity of the gas-phase include the pore tortuosity and the hydrodynamic dispersion effects. The diffusion of heat due to the species diffusion is neglected in the gas-phase energy equation. The pressure drop across the porous medium is assumed negligible when compared to the total pressure and the momentum equation becomes trivial.

The steady-state volume-averaged mass, species and energy conservation equations then become

$$\varepsilon \rho u = \varepsilon \rho_n s_F, \quad (2.39)$$

$$\varepsilon \rho_n s_F \frac{dY_F}{dx} = \varepsilon \rho D_F \frac{d^2 Y_F}{dx^2} - \varepsilon A \rho^2 Y_O Y_F T_g^a e^{-E_a/R_u T_g}, \quad (2.40)$$

$$\varepsilon \rho_n s_F \frac{dY_O}{dx} = \varepsilon \rho D_O \frac{d^2 Y_O}{dx^2} - \varepsilon \nu A \rho^2 Y_O Y_F T_g^a e^{-E_a/R_u T_g}, \quad (2.41)$$

$$\varepsilon \rho_n s_F c_p \frac{dT_g}{dx} = \varepsilon \lambda_g \frac{d^2 T_g}{dx^2} + \varepsilon Q A \rho^2 Y_O Y_F T_g^a e^{-E_a/R_u T_g} + h_v (T_s - T_g), \quad (2.42)$$

$$0 = (1 - \varepsilon) \lambda_s \frac{d^2 T_s}{dx^2} - h_v (T_s - T_g), \quad (2.43)$$

where εD_F and εD_O are de fuel and oxidant effective mass diffusivities, Q is the fuel mass based heat of reaction and h_v is the volumetric surface-convection coefficient ($h_v = h_{gs} A_{gs}/V$).

This set of conservation equations will be applied in the subsequent chapters.

Chapter 3

Asymptotic solution for moderately lean mixtures

In this chapter, the method of matched asymptotic expansions is used to solve the problem of a stationary premixed flame in an infinite adiabatic porous medium. The solution is obtained for the case of moderately lean mixtures, where the interphase heat transfer is not intense.

3.1 Introduction

The problem of a stationary flame within an inert porous medium has been studied analytically before. From the earlier analysis, Deshaies and Joulin [74] (semi-infinite burner) and Buckmaster and Takeno [75] (finite length burner) used the high-activation-energy asymptotic method to solve the flame structure considering that the solid-phase temperature is constant and equal to the adiabatic flame temperature. These models divide the flame in a pre-heating region, a thin combustion region and a post-combustion region. The results agreed with the numerical solutions obtained by Takeno and Sato [9] and Takeno et al. [76]. However, these solutions

are restricted to very large solid-phase thermal conductivities. Following these earlier works, Boshoff-Mostert and Viljoen [77] presented an analytical solution for the combustion in a monolith of finite length. The difference from previous work is that their model accounts for the variations of the solid-phase temperature. The flame position within the porous medium is defined as a function of an imposed flame velocity.

The problem of gas combustion in porous inert media exhibits some similarities with the field of filtration combustion. A series of analytical works has been presented by Aldushin, Matkowsky and coworkers [78, 79, 80, 81, 82, 83] covering many aspects of smoldering and self-propagating high temperature synthesis (SHS). In these problems, an oxidant stream filtrates through the porous medium until it reaches the reaction front, where heterogeneous reactions take place. As a result, the combustion develops as a traveling wave. In the case of forward filtration combustion, superadiabatic temperatures are observed. In this situation, Aldushin et al. [81] analyze the conditions that lead to the maximum energy accumulation at the flame. Wahle and Matkowsky [82] and Wahle et al. [83] show that one-equation models for the conservation of energy are only appropriate for the case of slow combustion waves, in which there is enough contact time between the phases and local thermal equilibrium is reached. Two-equation models for the energy transport must be used when the gas velocity is increased beyond the point that the large contact time assumption is violated and local thermal non-equilibrium arises.

Zhdanok et al. [36] investigated analytically and experimentally the filtration combustion of methane-air mixtures within an inert porous medium. The study shows that the superposition of a thermal and a reaction wave can be reached by controlling the filtration rate of the reactants mixture. In this case, high excess

enthalpy is reached at the flame. The superadiabatic effect is amplified when the thermal and reaction waves have close velocities of propagation. Bubnovich et al. [84] proposed an analytical solution for the filtration combustion of lean methane-air mixtures in a semi-infinite inert porous medium with heat loss, considering the local thermal equilibrium approximation. The burner was divided in a pre-heating region, a reaction region and a region filled with combustion products. The closure for the system of equations is obtained by providing an equation for the flame ignition temperature. This equation is developed following the classical free-flame theory, considering that the thickness of the reaction region is of the same order of the pore size. Algebraic expressions for the temperature and concentration profiles and for the velocity of the combustion wave were determined.

McIntosh [85] and McIntosh and Prothero [86] proposed a model for the surface combustion with radiant heat loss, i.e., for a porous burner in which the flame is stabilized on the porous medium surface or just above it. In these burners the flame is cooled by the radiant heat loss, which implies in low NO_x emissions. This work relies on the large-activation-energy asymptotic method to derive an analytical solution for the gas and solid temperatures. The solutions depend on (i) a convective heat transfer parameter, (ii) a radiant loss coefficient and (iii) the ratio of the gas-phase to the solid-phase thermal conductivities, which is imposed to be of the order of unity. As in the previous works the combustion front is divided in three regions and the flame position is a function of a specified flame velocity. The result showed the effect of those three parameters on flame location and allowed for the prediction of the blow-off and flashback conditions.

Here, an asymptotic solution for a stationary flame within an infinite adiabatic

porous burner is proposed. This condition is similar to that of a long insulated burner in which the flame stabilizes deeply within the porous medium. In contrast to the other asymptotic solutions mentioned above, the present model takes advantage from the large difference between the thermal conductivity of the solid and gas phases. This difference allows for the separation of the problem in characteristic length-scales corresponding to the heat conduction in the solid-phase (outer region) and to the heat and mass diffusion in the gas-phase (first inner region). Another characteristic length-scale is associated to the reaction zone (second inner region) and its solution gives a closed form equation for the flame velocity.

This treatment relies on a closer examination of the different characteristic length-scales and of the source of the large local thermal non-equilibrium present in flames within porous media. The scales are assumed to be sufficiently separated such that the asymptotic expansion method can be used to determine the flame structure. Closed form solutions for the gas- and solid-phase temperatures, fuel and oxidant mass fractions, flame speed, flame thickness and heat recirculation efficiency are found as a function of the problem parameters. The effects of the thermal conductivities ratio, equivalence ratio, volumetric porosity and fuel Lewis number on such flames are evidenced.

Although many articles have been published on this subject, to the best of the author's knowledge, none has presented a universal relation connecting the gas- and solid-phase properties with the flame structure and superadiabatic effect. Such relation could be used to improve the understanding regarding the origin of the limiting conditions for flame propagation, the upper limit for the superadiabatic effect and

the combined effects of gas-phase Lewis number, porosity and interfacial heat transfer coefficient on the extent of departure from thermal equilibrium. The main goal here is to evidence the effect of the problem parameters on the flame structure and heat recirculation in a simple explicit form. For this purpose, the large activation energy asymptotic theory is employed. This analysis can suggest new ways to tailor the porous medium and gas-phase to reach the maximum combustion efficiency.

The model developed in this chapter is valid for near-stoichiometric mixtures, a condition where high flame velocities are found. In these cases, the interphase heat transfer in the inner scales of the problem is negligible due to the small contact time between the phases. This will be characterized by small values of an interphase heat transfer parameter N , to be defined in Section 3.3.1. In the next two chapters extensions to the present model to lower equivalence ratios will be presented.

In the following, the physics of the combustion in porous inert media is reviewed with the aim of identifying the characteristic length-scales and their basic properties. Then, the equations for the model are written and solved using the well established asymptotic expansion method [87]. Finally, the obtained results are presented and discussed. A comparison between the analytical model and a numerical solution of the differential equations, providing an assessment of the effect of the simplifying assumptions on the details of the solution obtained, is also presented.

3.2 Length-scales and thermal non-equilibrium

The main difference between flames in porous media and freely propagating flames is the presence of the solid-phase thermally connecting the two sides of the flame. This connection enhances the thermal diffusion from the hot burned gases to the fresh unburned gases. Also, the radiant heat transfer among solid surfaces increases the heat transfer from the hot region to the cold region, specially for porous structures with small optical thicknesses [47]. As a consequence of this heat transfer enhancement (heat recirculation), the flame reaches temperatures higher than those in freely propagating flames, i.e. superadiabatic flame temperatures.

The properties of the gas and solid phases are very dissimilar. The solid-phase thermal conductivity can be several orders of magnitude larger than that of the gas-phase. As a result, in a large region around the flame, significant differences between the temperatures of the two phases are found (local thermal non-equilibrium) leading to interphase heat transfer [4]. This surface convection heat transfer between the phases depends on the interfacial surface area and on the flow field within the porous structure. The region where the heat conduction in the solid-phase prevails over the gas-phase conduction is associated to a characteristic length-scale, which is not present in freely propagating flames. The model developed here relies on a physical description based on separation of characteristic length-scales. This physical description is reviewed next.

Figure 3.1 presents a rendering of a stationary adiabatic plane flame within an infinite inert porous medium. The flame structure can be described in four levels of detail. In a first level, Fig. 3.1a, the flame front propagates with velocity s_F against the unburnt gas. For stationary flames $s_F = u_n$, where u_n is the incoming

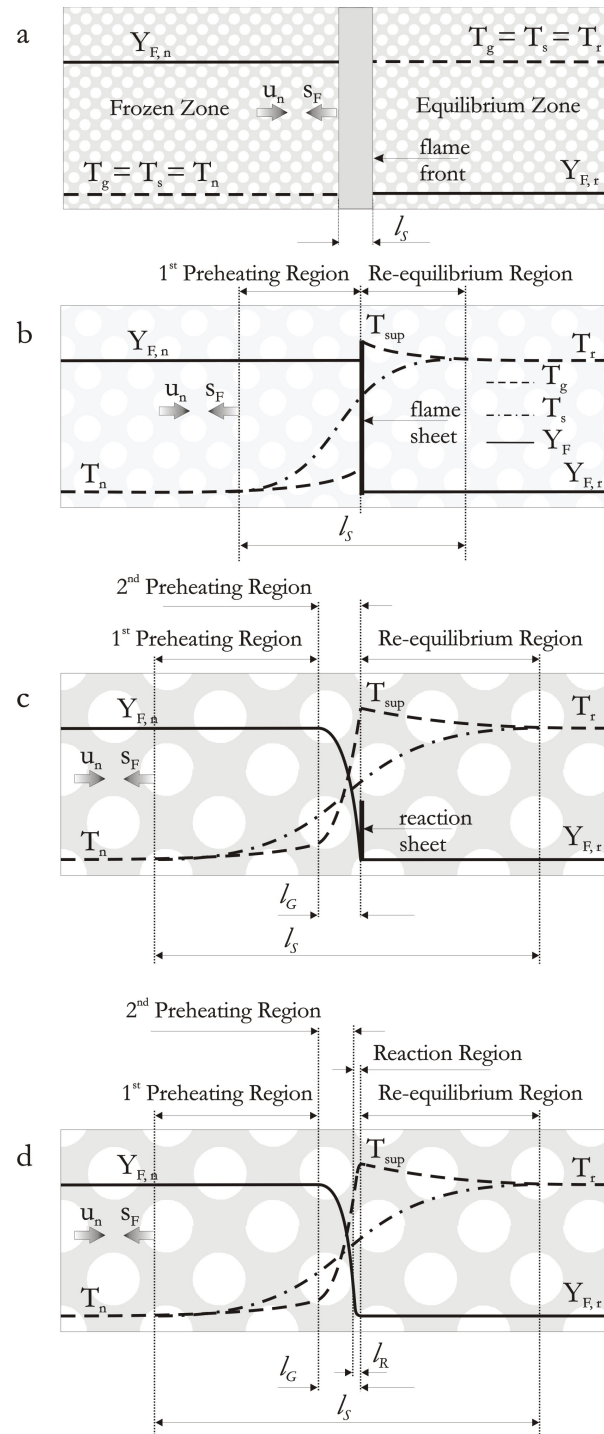


Figure 3.1: Rendering of the temperatures and fuel mass fraction distributions for the different characteristic length-scales of the problem.

(phasic averaged) gas velocity. Note that the Darcean flame speed, s_D , equal to the filtration velocity for stationary flames, is related to the phasic averaged flame speed by $s_D = \varepsilon s_F$, where ε is the volumetric porosity of the matrix. In this first level of detail, the flame front separates two regions where gas and solid are in thermodynamic equilibrium. Upstream from the front, the temperatures of both phases and the fuel mass fraction are equal to their initial values, T_n and Y_{Fn} respectively. Downstream from the front, the temperatures of both phases reach the adiabatic flame temperature T_r , according to the thermodynamic requirement, and the fuel mass fraction jumps down to its final value, Y_{Fr} , which is zero for lean mixtures.

In the second level of detail, Fig. 3.1b, the heat transfer by conduction through the solid-phase, the interphase surface heat transfer and the gas-phase convection (advection) heat transfer control the problem. Frozen flow is assumed upstream and chemical equilibrium flow is assumed downstream from the flame front. However, thermal non-equilibrium between the phases occurs upstream and downstream from the flame sheet, establishing the interphase surface heat transfer. The transport of mass and heat by diffusion in the gas-phase can be neglected in this level. As a result of this assumption, both the gas-phase temperature and the fuel mass fraction distributions are discontinuous across the flame sheet. Upstream from the flame the unburnt gas is heated up by the solid-phase (first pre-heating region) and downstream from the flame the solid-phase is heated up by the burned gas (re-equilibrium region). At the flame sheet the gas temperature reaches the superadiabatic peak, T_{sup} , and then decreases in the re-equilibrium region to the adiabatic flame temperature T_r . The fuel mass fraction is constant and equal to its initial value upstream from the flame and is completely consumed at the flame sheet for lean mixtures. The temperature of

the solid-phase varies smoothly from its initial temperature T_n to its final temperature T_r as a result of heat transfer by conduction and radiation. Then, the extent of this thermally affected region is determined by a balance among the conduction through the solid-phase, the interphase heat transfer and the advection transport in the gas-phase. In the present model, this large region of thermal non-equilibrium is related to a characteristic solid-phase diffusion length-scale, defined as the ratio of the solid-phase conduction to the gas-phase convection, $l_S \equiv (1-\varepsilon)\lambda_s/(\varepsilon\rho_n s_F c_p)$, where $(1-\varepsilon)\lambda_s$ is the solid-phase effective thermal conductivity, ρ_n is the unburnt gas-phase density and c_p is the gas-phase heat capacity. From the volume-averaging theory, this effective solid thermal conductivity must include a tortuosity effect as well as a radiant contribution [63].

In the third level of detail, Fig. 3.1c, the flame sheet is expanded, thus revealing the mass and heat transfer by diffusion in the gas-phase (second pre-heating region). The reaction is a source of thermal energy and a sink for reactants in the gas-phase (a reaction sheet). Thus, near the reaction sheet, the gas temperature increases due to the gas-phase heat conduction and the fuel concentration decreases because of the fuel depletion towards the reaction sheet. In this level of detail, the gas temperature and fuel mass fraction distributions are continuous across the reaction sheet, but their first derivatives are still discontinuous. The solid-phase temperature profile is approximately linear because the interphase heat transfer is expected to be negligible when compared to the gas conduction heat transfer in the second pre-heating region. A characteristic gas-phase diffusion length-scale can be defined as the ratio of the gas-phase conduction to the gas-phase convection, $l_G \equiv \varepsilon\lambda_g/(\varepsilon\rho_n s_F c_p)$, where $\varepsilon\lambda_g$ is the gas-phase effective thermal conductivity. The relation between the solid- and the

gas-phase characteristic diffusion length-scales is expressed by

$$\frac{l_G}{l_S} = \frac{\varepsilon}{(1 - \varepsilon)\Gamma},$$

where Γ is the ratio of the solid and gas thermal conductivities ($\Gamma \equiv \lambda_s/\lambda_g$). Note that for freely propagating flames the gas diffusion length-scale is defined as $l_G^0 \equiv \lambda_g^0/(\rho_n s_F^0 c_p)$, where s_F^0 is the flame velocity for free flames and λ_g^0 is the gas-phase molecular thermal conductivity. The ratio of the gas-phase diffusion length-scale for flames within porous media and that for free flames is $l_G/l_G^0 = (\lambda_g/\lambda_g^0)(s_F^0/s_F)$. Since s_F is expected to be more than two times larger than s_F^0 [47], as a consequence of the heat recirculation, the gas-phase diffusion length-scale for flames within porous media is thinner than that for free flames, $l_G < l_G^0$.

As the porosity of the matrix increases the solid-phase characteristic length-scale becomes shorter. For the case of $\varepsilon/(1 - \varepsilon) \rightarrow \Gamma$ the two length-scales are of the same order of magnitude ($l_G/l_S \rightarrow 1$). Then, $\varepsilon/(1 - \varepsilon) \ll \Gamma$ is the necessary condition to ensure the scale separation. For the case $\varepsilon/(1 - \varepsilon) \sim O(1)$ the ratio between the characteristic length-scales reduces to $l_G/l_S \sim O(1/\Gamma)$. In the present model, this limit is considered.

The limit $\varepsilon \rightarrow 1$, not analyzed in this work, imposes a negligible effect of the solid-phase heat conduction process on the flame, compared to the other processes, leading to thermal equilibrium in a wider region around the flame. In this case, in order to evaluate the contribution of the conduction in the solid-phase on premixed flames in porous media, it would be necessary to analyze the limit $1 - \varepsilon = O(\Gamma^{-1})$.

In the last, and more complete, level of detail, Fig. 3.1d, the reaction sheet is expanded revealing the chemical reaction and the continuous variation of the gas temperature and fuel mass fraction first derivatives. Now, it is of interest to define a

characteristic reaction length-scale l_R . This can be achieved through the continuity of the heat flux at the flame, $\Delta T_R/l_R \sim \Delta T_G/l_G$, where ΔT_R is the gas-phase temperature change across the reaction region and ΔT_G is the gas-phase temperature change across the second pre-heating region ($\Delta T_G = T_r - T_n$, since all the heat of combustion is released within the reaction region). The temperature variation across the reaction region can be approximated by $\Delta T_R \sim (w/(dw/dT))_{T_{sup}}$, where w is the reaction rate. Then, based on the simplest kinetic mechanism of one global step, modeled by an Arrhenius reaction rate model, the relations among the characteristic length-scales are

$$\frac{l_R}{l_G} = \frac{R_u T_{sup}}{E_a} \frac{T_{sup}}{(T_r - T_n)} \equiv \frac{1}{\beta'} \equiv \delta \quad \text{and} \quad \frac{l_R}{l_S} = \frac{\varepsilon}{(1 - \varepsilon)} \frac{1}{\beta' \Gamma} = \frac{\varepsilon}{(1 - \varepsilon)} \frac{\delta}{\Gamma},$$

where β' is a modified Zel'dovich number, R_u is the universal gas constant and E_a is the activation energy. For freely propagating flames, the ratio between the reaction and the gas-diffusion length-scales is $l_R^0/l_G^0 = 1/\beta \equiv \delta^0$, where β is the classical Zel'dovich number ($\beta \equiv E_a (T_r - T_n)/(R_u T_r^2)$) which usually lies between 5 and 15 [87, 88, 89]. Since $T_{sup} > T_r$ and defining $T_{sup} \equiv T_r + T_H$, with $T_H/T_r < 1$, the ratio of the reaction length-scale for flames within porous media to that of freely propagating flames can be estimated as

$$\frac{l_R}{l_R^0} \sim \frac{s_F^0 \lambda_g}{s_F \lambda_g^0} \left[1 + 2 \left(\frac{T_H}{T_r} \right) \right].$$

The expression above shows that the reaction length-scale l_R is expected to be smaller for flames within porous media than for freely propagating flames. Nevertheless, the ratio between the reaction and the gas-diffusion length-scales is larger for flames in porous media, $\delta/\delta^0 \sim 1 + 2(T_H/T_r)$.

For freely propagating flames at 1 atm and reactants at 298 K, the flame thickness

is of the order of 1 mm for hydrocarbon fuels [68]. In porous media, the flame thickness, defined as the sum of the second pre-heating region and the reaction region thicknesses, is expected to be of the same order of magnitude. The typical ceramic foams used as solid matrix in porous burners have pore diameters ranging from 1 to 4 mm. The exceptions are the surface burners where smaller pore diameters are used [32]. Then, the reactions are not expected to spread over several pores but to be confined to a fraction of a single pore. As discussed before, results of direct numerical simulations obtained by Sahraoui and Kaviany [44] and Hackert et al. [51] confirm this hypothesis. Therefore, the description of the structure of premixed gas flames within inert porous media is very similar to that of free flames and we take advantage of this idealization. The main difference is that in the combustion in porous media there is an additional wider region (l_S) of heat exchange between the gas and solid phases leading to higher gas temperatures.

As a consequence, from the asymptotic point of view, the flame structure analysis follows the hypothesis that $l_R \ll l_G \ll l_S$. From the point of view of the use of a continuous treatment for the porous medium [63], it is assumed that $l_S > l_{rev} \gg l_d$, where l_{rev} is the characteristic length of the representative elementary volume over which the volume averaging is done and l_d is the characteristic length of the pores. This means that the solid- and gas-phase temperature variations spread over a large number of pores, that is a reasonable assumption for the porous structures of interest. Since the diffusion of heat and mass in the gas-phase are significant only in a length-scale (l_G) of the order of the pore diameter, the solutions of the second pre-heating region and the reaction region will behave similarly to a sub-grid model for the prediction of the flame speed. This will be evidenced when the heat transfer between

the phases is neglected in both problems of the order of l_G and l_R , showing that the solid-phase temperature solution for these scales do not bring new information to the problem.

3.3 Mathematical formulation

A one-dimensional two-medium model for the conservation of mass, gas-phase energy, solid-phase energy and mass of chemical species, as given by Eqs. (2.39) to (2.43), is considered. In the sequence these equations are non-dimensionalized and solved by asymptotic expansions taking advantage of the differences among the three characteristic length-scales identified.

3.3.1 Non-dimensionalization

Defining the non-dimensional variables [88]

$$y_F \equiv \frac{Y_F}{Y_{Fn}}, \quad y_O \equiv \frac{Y_O}{Y_{On}}, \quad \theta \equiv \frac{c_p(T - T_n)}{Y_{Fn} Q} = \frac{T - T_n}{T_r - T_n} \quad \text{and} \quad \zeta \equiv \int_0^x \frac{\rho_n s_F c_p}{\lambda_s} dx,$$

Eqs. (2.40) to (2.43) become

$$\varepsilon \frac{dy_F}{d\zeta} = \frac{\varepsilon}{Le_F \Gamma} \frac{d^2 y_F}{d\zeta^2} - \varepsilon \Gamma Da \, y_O y_F \exp \left[-\frac{\beta(1 - \theta_g)}{1 - \alpha(1 - \theta_g)} \right], \quad (3.1)$$

$$\varepsilon \frac{dy_O}{d\zeta} = \frac{\varepsilon}{Le_O \Gamma} \frac{d^2 y_O}{d\zeta^2} - \varepsilon \phi \Gamma Da \, y_O y_F \exp \left[-\frac{\beta(1 - \theta_g)}{1 - \alpha(1 - \theta_g)} \right], \quad (3.2)$$

$$\varepsilon \frac{d\theta_g}{d\zeta} = \frac{\varepsilon}{\Gamma} \frac{d^2 \theta_g}{d\zeta^2} + \varepsilon \Gamma Da \, y_O y_F \exp \left[-\frac{\beta(1 - \theta_g)}{1 - \alpha(1 - \theta_g)} \right] + N(\theta_s - \theta_g), \quad (3.3)$$

$$0 = (1 - \varepsilon) \frac{d^2 \theta_s}{d\zeta^2} - N(\theta_s - \theta_g), \quad (3.4)$$

where

$$\Gamma \equiv \frac{\lambda_s}{\lambda_g}, \quad \phi \equiv \frac{Y_{Fn}\nu}{Y_{On}}, \quad \alpha \equiv \frac{(T_r - T_n)}{T_r}, \quad \beta \equiv \frac{E_a(T_r - T_n)}{R_u T_r^2},$$

$$Le \equiv \frac{\lambda_g}{\rho c_p D} \quad \text{and} \quad Da \equiv \frac{A \rho^2 \lambda_g Y_{On} T_g^a \exp(-\beta/\alpha)}{\rho_n^2 s_F^2 c_p},$$

The parameter ϕ is the equivalence ratio, α is the dimensionless heat release, β is the Zel'dovich number, Le is an effective Lewis number that accounts for the thermal and species hydrodynamic dispersions and Da is the Damköhler number.

The parameter N appearing in Eqs. (3.3) and (3.4) is related to the heat transfer between the phases and is defined as

$$N \equiv \frac{\lambda_s h_v}{(\rho_n s_F c_p)^2}. \quad (3.5)$$

In the present model, the interphase heat transfer parameter N is assumed to be of the order of unity. In the next chapters, other limits to the parameter N will be explored.

In the present work, the length-scale l_S is chosen such that the heat conduction through the solid effective medium balances the heat convected by the gas-phase and, therefore, is of the same order of magnitude as the interphase heat transfer [a condition represented by $N \sim O(1)$]. It is worth to note that for intense interphase heat transfer, $N \gg 1$, or for low interphase heat transfer, $N \ll 1$, a new characteristic length-scale can be defined as $l' \sim O(l_S N^{-1/2})$ to capture the thermal non-equilibrium region in a length-scale of the order of unity. Note also that the present solution is constructed under the hypothesis that $\varepsilon/(1 - \varepsilon) \sim O(1)$. Then the parameter ε is not used to define the nondimensional coordinate ζ .

In a region of the order of unity around the flame, the parameter Γ appears dividing the diffusion terms in Eqs. (3.1) to (3.3) and it satisfies the condition $\Gamma \gg 1$. By using this property, it is possible to employ the singular perturbation method to find an analytical solution for the problem [90, 91, 92]. In a region of the order of Γ^{-1} near the flame, the gas-phase temperature reaches its maximum value (the flame temperature). Then, since the non-dimensional gas-phase temperature variation is of the order of unity, but the spatial variation is of the order of Γ^{-1} , the description of the second pre-heating region follows a boundary layer expansion. In a region of the order of $\delta\Gamma^{-1}$ the variables present a small variation of the order of δ and the large-activation-energy asymptotic expansion is employed.

In the following, the order unity problem, corresponding to the solid-phase diffusion length-scale l_S , is solved. Then, the problem of the order of Γ^{-1} , corresponding to the gas-phase diffusion length-scale l_G , is solved. Finally, the problem of the order of $\delta\Gamma^{-1}$, corresponding to the reaction length-scale l_R , is solved.

3.3.2 Outer zone: problem of the order of unity

In the characteristic length-scale $\zeta - \zeta_f = O(1)$, the diffusive terms in the gas-phase are of the order of Γ^{-1} and the reaction is exponentially small. Thus, Eqs. (3.1) to (3.4) take the form

$$\varepsilon \frac{dy_F}{d\zeta} = \frac{\varepsilon}{Le_F \Gamma} \frac{d^2 y_F}{d\zeta^2}, \quad (3.6)$$

$$\varepsilon \frac{dy_O}{d\zeta} = \frac{\varepsilon}{Le_O \Gamma} \frac{d^2 y_O}{d\zeta^2}, \quad (3.7)$$

$$\varepsilon \frac{d\theta_g}{d\zeta} = \frac{\varepsilon}{\Gamma} \frac{d^2 \theta_g}{d\zeta^2} + N(\theta_s - \theta_g), \quad (3.8)$$

$$0 = (1 - \varepsilon) \frac{d^2 \theta_s}{d\zeta^2} - N(\theta_s - \theta_g). \quad (3.9)$$

The solution of Eqs. (3.6) to (3.9) can be written as

$$\left. \begin{aligned} \theta_s &= \theta_s^{(0)} + \Gamma^{-1}\theta_s^{(0)(1)} + o(\Gamma^{-1}) \\ \theta_g &= \theta_g^{(0)} + \Gamma^{-1}\theta_g^{(0)(1)} + o(\Gamma^{-1}) \\ y_O &= y_O^{(0)} + \Gamma^{-1}y_O^{(0)(1)} + o(\Gamma^{-1}) \\ y_F &= y_F^{(0)} + \Gamma^{-1}y_F^{(0)(1)} + o(\Gamma^{-1}) \end{aligned} \right\}. \quad (3.10)$$

Substituting these expansions in Eqs. (3.6) to (3.9) and applying the limit of $\Gamma \rightarrow \infty$, the first approximation for the set of equations of the order of unity is

$$\varepsilon \frac{dy_F^{(0)}}{d\zeta} = 0, \quad (3.11)$$

$$\varepsilon \frac{dy_O^{(0)}}{d\zeta} = 0, \quad (3.12)$$

$$\varepsilon \frac{d\theta_g^{(0)}}{d\zeta} = N(\theta_s^{(0)} - \theta_g^{(0)}), \quad (3.13)$$

$$0 = (1 - \varepsilon) \frac{d^2\theta_s^{(0)}}{d\zeta^2} - N(\theta_s^{(0)} - \theta_g^{(0)}). \quad (3.14)$$

This problem corresponds to the situation described in Fig. 3.1b. Then, we are looking for a solution for the first pre-heating region ($\zeta < \zeta_f$) and for the re-equilibrium region ($\zeta > \zeta_f$). The boundary conditions are $\theta_g^{(0)} = \theta_s^{(0)} = 0$ and $y_F^{(0)} = y_O^{(0)} = 1$ for $\zeta \rightarrow -\infty$ and $\theta_g^{(0)} = \theta_s^{(0)} = 1$ and $y_F^{(0)} = y_O^{(0)} - (1 - \phi) = 0$ for $\zeta \rightarrow +\infty$. The values of the variables at the flame sheet are unknowns to be determined.

The solution for Eqs. (3.11) and (3.12) are

$$y_F^{(0)} = \begin{cases} 1, & \text{for } \zeta \leq \zeta_f, \\ 0, & \text{for } \zeta \geq \zeta_f, \end{cases} \quad (3.15)$$

$$y_O^{(0)} = \begin{cases} 1, & \text{for } \zeta \leq \zeta_f, \\ 1 - \phi, & \text{for } \zeta \geq \zeta_f. \end{cases} \quad (3.16)$$

A relation between the gas-phase temperature $\theta_g^{(0)}$ and the solid-phase temperature $\theta_s^{(0)}$ is found by combining and integrating Eqs. (3.13) and (3.14) giving

$$\theta_g^{(0)} - \frac{(1-\varepsilon)}{\varepsilon} \frac{d\theta_s^{(0)}}{d\zeta} = C^{(0)}, \quad (3.17)$$

with $C^{(0)} = 0$ for $\zeta \leq \zeta_f$ and $C^{(0)} = 1$ for $\zeta \geq \zeta_f$.

Substituting Eq. (3.17) into Eq. (3.14) we obtain

$$\frac{d^2\theta_s^{(0)}}{d\zeta^2} + \frac{N}{\varepsilon} \frac{d\theta_s^{(0)}}{d\zeta} - \frac{N}{(1-\varepsilon)} \theta_s^{(0)} = -\frac{N}{(1-\varepsilon)} C^{(0)}. \quad (3.18)$$

Once Eq. (3.18) is solved, the gas-phase temperature $\theta_g^{(0)}$ is determined from Eq. (3.17). The solution for the solid-phase temperature is given by

$$\theta_s^{(0)} = \begin{cases} \theta_s^{(0)}(\zeta_f) e^{r_1(\zeta-\zeta_f)}, & \text{for } \zeta \leq \zeta_f, \\ 1 - [1 - \theta_s^{(0)}(\zeta_f)] e^{-r_2(\zeta-\zeta_f)}, & \text{for } \zeta \geq \zeta_f, \end{cases} \quad (3.19)$$

where

$$r_1 = \frac{N}{2\varepsilon} \left[-1 + \left(1 + \frac{4\varepsilon^2}{N(1-\varepsilon)} \right)^{1/2} \right]$$

and

$$r_2 = \frac{N}{2\varepsilon} \left[1 + \left(1 + \frac{4\varepsilon^2}{N(1-\varepsilon)} \right)^{1/2} \right].$$

The value of the solid-phase temperature at the flame location $\theta_s^{(0)}(\zeta_f)$ is calculated imposing the continuity of the function and its first derivative (the conduction heat flux), obtaining

$$\theta_s^{(0)}(\zeta_f) = \frac{r_2}{r_1 + r_2} = \frac{1}{2} \left\{ 1 + \left[1 + \frac{4\varepsilon^2}{N(1-\varepsilon)} \right]^{-1/2} \right\}. \quad (3.20)$$

Even out of its range of validity the model can show important tendencies for the flame behavior at the limits for the volumetric porosity. Then, from Eq. (3.20), we observe that for very low values of porosity, $\varepsilon \ll 1$, the solid-phase temperature at

the flame approaches a limiting value equal to unity according to $\theta_s^{(0)}(\zeta_f) \sim 1 - \varepsilon^2/N$. Conversely, for high porosity, $1 - \varepsilon \ll 1$, the solid-phase temperature at the flame approaches a limiting value equal to 1/2 according to $\theta_s^{(0)}(\zeta_f) \sim 1/2 + [N(1 - \varepsilon)]^{1/2}/4$. Thereby, it is possible to conclude that $1/2 < \theta_s^{(0)}(\zeta_f) < 1$ for every possible value of porosity.

Once knowing the leading order term of the solid-phase temperature $\theta_s^{(0)}$, the leading order term of the gas-phase temperature $\theta_g^{(0)}$ can be determined from Eq. (3.17), obtaining

$$\theta_g^{(0)} = \begin{cases} [(1 - \varepsilon)/\varepsilon] r_1 \theta_s^{(0)}(\zeta_f) e^{r_1(\zeta - \zeta_f)}, & \text{for } \zeta \leq \zeta_f, \\ 1 + [(1 - \varepsilon)/\varepsilon] r_2 [1 - \theta_s^{(0)}(\zeta_f)] e^{-r_2(\zeta - \zeta_f)}, & \text{for } \zeta \geq \zeta_f. \end{cases} \quad (3.21)$$

Imposing the condition $\zeta = \zeta_f$ in the solution for the gas-phase temperature, Eq. (3.21), the following values for the upstream and downstream sides of the flame are found respectively by

$$\theta_g^{(0)}(\zeta_f^-) = [(1 - \varepsilon)/\varepsilon] r_1 \theta_s^{(0)}(\zeta_f), \quad (3.22)$$

$$\theta_g^{(0)}(\zeta_f^+) = 1 + [(1 - \varepsilon)/\varepsilon] r_2 [1 - \theta_s^{(0)}(\zeta_f)]. \quad (3.23)$$

Subtracting Eq. (3.22) from Eq. (3.23) and applying the definition of $\theta_s^{(0)}(\zeta_f)$, Eq. (3.20), the difference $\theta_g^{(0)}(\zeta_f^+) - \theta_g^{(0)}(\zeta_f^-)$ reveals the discontinuity of the gas-phase temperature across the flame in the scale of the order of unity, which is

$$\theta_g^{(0)}(\zeta_f^+) - \theta_g^{(0)}(\zeta_f^-) = 1. \quad (3.24)$$

This result was expected since all the heat released by the combustion process is confined to a thin region (the flame sheet in Fig. 3.1b). This means that all the heat recirculated to the gas-phase in the first pre-heating region must result in excess

temperature at the downstream side of the flame, i.e., the difference between the maximum temperature at the flame and the adiabatic flame temperature based on the incoming reactants.

Again, it is worth analyzing the model at the limits for the volumetric porosity. For very low porosities, $\varepsilon \ll 1$, the gas and solid phases are in thermal equilibrium except in a region of the order of Γ^{-1} around the flame. In this case, at the upstream side of the flame, the temperature of both phases can be approximated by $\theta_g^{(0)}(\zeta_f^-) = \theta_s^{(0)}(\zeta_f) \sim 1 - \varepsilon^2/N$ and the value of the gas-phase temperature at the downstream side of the flame can be determined from Eq. (3.24), $\theta_g^{(0)}(\zeta_f^+) \sim 2 - \varepsilon/N^2$. For the other extreme condition, very high porosities, $1 - \varepsilon \ll 1$, the solution tends to a free flame solution. The temperature of the two phases in the region $\zeta \leq \zeta_f$ are equal to zero, except very close to the flame. At this location, the gas-phase temperature is $\theta_g^{(0)}(\zeta_f^-) \sim N^{1/2}(1 - \varepsilon)^{1/2}\theta_s^{(0)}(\zeta_f)$. Then, the gas-phase temperature at the downstream side of the flame differs very little from the adiabatic value, $\theta_g^{(0)}(\zeta_f^+) \sim 1 + N^{1/2}(1 - \varepsilon)^{1/2}\theta_s^{(0)}(\zeta_f)$. Thereby, it is possible to conclude that $1 < \theta_g^{(0)}(\zeta_f^+) < 2$ for every possible value of porosity.

The heat recirculated by the porous medium is equal to the gas pre-heating in the problem of the order of unity. Then, a heat recirculation efficiency can be defined as the ratio between the heat recirculated and the total energy released by the combustion process as

$$\eta_{rec} \equiv \frac{\rho_n s_F c_p (T_{g,f}^- - T_n)}{\rho_n s_F Y_{F,n} Q} = \theta_g^{(0)}(\zeta_f^-), \quad (3.25)$$

where $T_{g,f}^-$ is the flame temperature at the upstream side of the flame. Recalling the definition of the non-dimensional temperature, it is seen that the expression for the heat recirculation efficiency is exactly the non-dimensional gas-phase temperature at

the upstream side of the flame, Eq. (3.22).

Substituting Eqs. (3.20) and (3.22) into (3.25) one finds

$$\eta_{rec} = (1 + N_\varepsilon)^{-1/2}, \quad (3.26)$$

where

$$N_\varepsilon = \frac{4\varepsilon^2}{N(1 - \varepsilon)}. \quad (3.27)$$

Then, Eqs. (3.22), (3.23) and (3.20) can be expressed in the following form:

$$\theta_g^{(0)}(\zeta_f^-) = \eta_{rec}, \quad (3.28)$$

$$\theta_g^{(0)}(\zeta_f^+) = 1 + \eta_{rec}, \quad (3.29)$$

$$\theta_s^{(0)}(\zeta_f) = (1 + \eta_{rec})/2. \quad (3.30)$$

Under the hypothesis considered here, the number N_ε is the parameter that characterizes the flame variables, universalizing the results. This means that different matrix properties and equivalence ratios will lead to the same values of $\theta_s^{(0)}(\zeta_f)$, $\theta_g^{(0)}(\zeta_f^-)$ and $\theta_g^{(0)}(\zeta_f^+)$, provided the parameter N_ε is kept constant. For this reason we choose to call this number the porous-media-flame number.

As a way of interpreting the parameter N_ε , an analogy can be made. By using the N and l_S definitions, N_ε can be written as

$$N_\varepsilon = 4 \left(\frac{h_v l_S}{\varepsilon \rho_n S_F C_p} \right)^{-1}. \quad (3.31)$$

Now, applying the definition of the number of transfer units (NTU) for a porous medium we have

$$NTU = \left(\frac{h}{\rho u c_p} \right) \frac{A_{gs}}{A_u} = \left(\frac{h}{\rho u c_p} \right) \frac{S_{gs} V}{\varepsilon A_T} = \frac{h_v L}{\varepsilon \rho u c_p}, \quad (3.32)$$

where A_{gs} is the interphase surface area, A_u is the transversal area of the fluid phase, S_{gs} is the interphase surface area density (m^2/m^3) and V , A_T and L are respectively the total volume, total transversal area and total length of the porous medium. Then, the parameter N_ε is a particular case of the reciprocal of the number of transfer units based on the length-scale l_S and on the flame velocity s_F ,

$$N_\varepsilon = 4/NTU_S \quad \text{and} \quad NTU_S = \frac{h_v l_S}{\varepsilon \rho_n s_F c_p}. \quad (3.33)$$

By making use of the universal description of the flame properties with N_ε , it is seen explicitly that the solid-phase temperature at the flame in the considered conditions is equal to the half of the gas-phase temperature, $\theta_s^{(0)}(\zeta_f) = \theta_g^{(0)}(\zeta_f^+)/2$.

In the next section, the second pre-heating region is analyzed.

3.3.3 Inner zone: problem of the order of Γ^{-1}

In this zone, the variation of the non-dimensional gas-phase temperature and fuel and oxidant mass fractions are of the order of unity along a characteristic length of the order of Γ^{-1} around the flame. Since there is no chemical source in the energy conservation equation for the solid-phase, the variations of the solid-phase temperature are of the order of Γ^{-1} . The solution in this thin zone is denoted by $y_F^{(*)}$, $y_O^{(*)}$, $\theta_g^{(*)}$ and $\theta_s^{(*)}$. The thin region around the flame, defined by the length-scale Γ^{-1} , is analyzed imposing the conditions that near the flame, more precisely at $\Gamma(\zeta - \zeta_f) = \xi$, the reactants mass fractions vary according to $1 \geq y_F^{(*)} \geq 0$, $1 \geq y_O^{(*)} \geq (1 - \phi)$ and $\theta_g^{(0)}(\zeta_f^-) \leq \theta_g^{(*)} \leq \theta_g^{(0)}(\zeta_f^+)$.

By re-scaling the spatial coordinate, and remembering that the reaction is exponentially small, the governing equations become

$$\varepsilon \frac{dy_F^{(*)}}{d\xi} = \frac{\varepsilon}{Le_F} \frac{d^2 y_F^{(*)}}{d\xi^2}, \quad (3.34)$$

$$\varepsilon \frac{dy_O^{(*)}}{d\xi} = \frac{\varepsilon}{Le_O} \frac{d^2 y_O^{(*)}}{d\xi^2}, \quad (3.35)$$

$$\varepsilon \frac{d\theta_g^{(*)}}{d\xi} = \varepsilon \frac{d^2 \theta_g^{(*)}}{d\xi^2} + \frac{N}{\Gamma} (\theta_s^{(*)} - \theta_g^{(*)}), \quad (3.36)$$

$$0 = (1 - \varepsilon) \frac{d^2 \theta_s^{(*)}}{d\xi^2} - \frac{N}{\Gamma^2} (\theta_s^{(*)} - \theta_g^{(*)}). \quad (3.37)$$

This problem corresponds to the second pre-heating region as described in Fig. 3.1c. The boundary conditions are determined when the solution corresponding to the problem of the order of Γ^{-1} is matched with the problem of the order of unity. Thus, for $\xi \rightarrow -\infty$ (upstream from the flame), $\theta_g^{(*)} \rightarrow \theta_g^{(0)}$, $\theta_s^{(*)} \rightarrow \theta_s^{(0)}$, $y_F^{(*)} \rightarrow y_F^{(0)} = 1$ and $y_O^{(*)} \rightarrow y_O^{(0)} = 1$. At the flame, $\theta_g^{(*)}$ is given by Eq. (3.23), $\theta_s^{(*)}$ by Eq. (3.20), $y_F^{(*)} = 0$ and $y_O^{(*)} = 1 - \phi$. Since the gas-phase temperature gradient at the downstream side of the flame is small when compared to the gradient at the upstream side, the solutions for $\xi \rightarrow \infty$ coincide with the solutions for the problem of the order of unity and do not bring new information.

The solution of Eqs. (3.34) and (3.35) for $\xi \leq \xi_f$ are

$$y_F^{(*)} = 1 - e^{Le_F(\xi - \xi_f)}, \quad (3.38)$$

$$y_O^{(*)} = 1 - \phi e^{Le_O(\xi - \xi_f)}. \quad (3.39)$$

An analysis of Eqs. (3.36) and (3.37) reveals that an approximated solution in

terms of an expansion on Γ^{-1} can be written as

$$\left. \begin{aligned} \theta_s^{(*)} &= \theta_s^{(*) (0)} + \Gamma^{-1} \theta_s^{(*) (1)} + \Gamma^{-2} \theta_s^{(*) (2)} + o(\Gamma^{-2}) \\ \theta_g^{(*)} &= \theta_g^{(*) (0)} + \Gamma^{-1} \theta_g^{(*) (1)} + \Gamma^{-2} \theta_g^{(*) (2)} + o(\Gamma^{-2}) \end{aligned} \right\}. \quad (3.40)$$

The temperature profiles are determined by the substitution of Eq. (3.40) into Eqs. (3.36) and (3.37) in the limit $\Gamma \rightarrow \infty$. Then, the equations for the leading order of the gas and solid phases are

$$\varepsilon \frac{d\theta_g^{(*) (0)}}{d\xi} = \varepsilon \frac{d^2 \theta_g^{(*) (0)}}{d\xi^2}, \quad (3.41)$$

$$(1 - \varepsilon) \frac{d^2 \theta_s^{(*) (0)}}{d\xi^2} = 0. \quad (3.42)$$

Analyzing Eqs. (3.40) and (3.42) we find that $\theta_s^{(*) (0)} = C_1^{(*)}$ and $\theta_s^{(*) (1)} = C_2^{(*)} \xi$, in which the value of $C_1^{(*)}$ and $C_2^{(*)}$ are determined matching the solution $\theta_s^{(*)}$ with $\theta_s^{(0)}$. The matching implies that, for $\xi \rightarrow -\infty$, the function must be continuous and the heat flux in the solid-phase $d\theta_s^{(*)}/d\xi$ is equal to the heat flux $\Gamma^{-1} d\theta_s^{(0)}/d\zeta$ at $\zeta = \zeta_f$. Then, $C_1^{(*)} = \theta_s^{(0)}(\zeta_f)$ and $C_2^{(*)} = d\theta_s^{(0)}/d\zeta|_{\zeta=\zeta_f}$.

The solution of equation Eq. (3.41) is $\theta_g^{(*) (0)}(\xi) = C_3^{(*)} e^\xi + C_4^{(*)}$. The constants are determined by the matching with the profile of $\theta_g^{(0)}$ at $\zeta = \zeta_f$. Thus, as $\xi \rightarrow -\infty$, $\theta_g^{(*) (0)} \rightarrow \theta_g^{(0)}(\zeta_f^-)$ leading to $\theta_g^{(*) (0)}(\xi) = C_3^{(*)} e^\xi + \theta_g^{(0)}(\zeta_f^-)$. The value of $C_3^{(*)}$ is specified applying the condition at the flame, $\theta_g^{(*) (0)}(\xi = 0) = \theta_g^{(0)}(\zeta_f^+)$, then, recalling that $\theta_g^{(0)}(\zeta_f^+) - \theta_g^{(0)}(\zeta_f^-) = 1$, we have

$$\theta_g^{(*) (0)}(\xi) = \theta_g^{(0)}(\zeta_f^-) + e^{(\xi - \xi_f)}. \quad (3.43)$$

The flame position ξ_f is determined by the coordinate system.

To reach the continuity of the first derivative of the gas-phase temperature at $\xi \rightarrow -\infty$ the correction $\theta_g^{(*) (1)}$ has to be solved. Then, substituting Eq. (3.40) into

Eq. (3.36), passing to the limit $\Gamma \rightarrow \infty$ and collecting the terms of the order of Γ^{-1} one finds

$$\frac{d}{d\xi} \left(e^{-\xi} \frac{d}{d\xi} \theta_g^{(*) (1)} \right) = \frac{N}{\varepsilon} \{ 1 + [\theta_g^{(0)}(\zeta_f^-) - \theta_s^{(0)}(\zeta_f)] e^{-\xi} \}, \quad (3.44)$$

whose solution is

$$\theta_g^{(*) (1)} = \frac{N}{\varepsilon} \{ e^\xi (\xi - 1) - e^{\xi_f} (\xi_f - 1) + [\theta_s^{(0)}(\zeta_f) - \theta_g^{(0)}(\zeta_f^-)] (\xi - \xi_f) \}, \quad (3.45)$$

after imposing the condition $\theta_g^{(*) (1)} = 0$ at $\xi = \xi_f$ and the matching condition

$$d\theta_g^{(*) (1)} / d\xi \Big|_{\xi \rightarrow -\infty} \rightarrow \Gamma^{-1} d\theta_g^{(0)} / d\zeta \Big|_{\zeta_f}.$$

The present solution assumes that $N \ll \Gamma$. Then, the heat transfer between the phases is negligible at the gas-phase diffusion length scale. This is not true for small equivalence ratios. In these cases, the small flame velocities increase the heat transfer parameter N and the heat transfer between the phases becomes relevant.

3.3.4 Inner zone: reaction region $O(\delta\Gamma^{-1})$

This problem corresponds to the situation described in Fig. 3.1d, where, in a region of the order of $\delta\Gamma^{-1}$ around the flame, the variables present a variation of the order of δ . The solution follows [87], which demands

$$\left. \begin{aligned} \theta_s &= \theta_{sf}^{(*)} + \delta \theta_s^{(1)} + o(\delta) \\ \theta_g &= \theta_{gf}^{(*)} - \delta (\theta_g^{(1)} + m\eta + p) + o(\delta) \\ y_O &= y_{Of}^{(*)} + \delta d_O Le_O y_O^{(1)} + o(\delta) \\ y_F &= 0 + \delta d_F Le_F y_F^{(1)} / \gamma + o(\delta) \\ Da &= Da_f + \delta Da^{(1)} + o(\delta) \\ \zeta &= \bar{\zeta}_f + \delta \Gamma^{-1} (\eta + p/m) / \gamma + o(\delta) \end{aligned} \right\}, \quad (3.46)$$

where $\theta_{sf}^{(*)}$ is given by Eq. (3.20), $\theta_{gf}^{(*)}$ is given by Eq. (3.23), $y_{0f}^{(*)} = 1 - \phi$, d_O and d_F are the oxidant and fuel diffusive fluxes at the flame sheet, δ is the non-dimensional reaction region thickness and $\bar{\zeta}_f = \zeta_f + \Gamma^{-1}\xi_f$.

Although the parameters m , γ and p will be defined latter, it is possible to mention that they provide translations and rotations in the coordinate system. This is done to normalize the equations and boundary conditions, simplifying the analytical solution.

Substituting Eq. (3.46) into the conservation equations Eqs. (3.1) to (3.4) and taking the limit $\delta \rightarrow 0$, the description of the reaction zone is governed by

$$\varepsilon \frac{d^2 y_F^{(1)}}{d\eta^2} = \varepsilon \bar{D}a_f y_F^{(1)} \exp[-(\theta_g^{(1)} + m\eta + p)], \quad (3.47)$$

$$\varepsilon \frac{d^2 y_O^{(1)}}{d\eta^2} = \varepsilon \phi \frac{d_F}{d_O} \bar{D}a_f y_F^{(1)} \exp[-(\theta_g^{(1)} + m\eta + p)], \quad (3.48)$$

$$\varepsilon \frac{d^2 \theta_g^{(1)}}{d\eta^2} = \varepsilon \frac{d_F}{\gamma} \bar{D}a_f y_F^{(1)} \exp[-(\theta_g^{(1)} + m\eta + p)] - \frac{\delta N}{\gamma^2 \Gamma} (\theta_{sf}^{(*)} - \theta_{gf}^{(*)}), \quad (3.49)$$

$$0 = (1 - \varepsilon) \frac{d^2 \theta_s^{(1)}}{d\eta^2} - \frac{\delta N}{\gamma^2 \Gamma^2} (\theta_{sf}^{(*)} - \theta_{gf}^{(*)}), \quad (3.50)$$

in which

$$\bar{D}a_f = Da_f \left(\frac{\delta^2 Le_F (1 - \phi)}{\gamma^2} \right) \exp \left\{ \frac{-\beta (1 - \theta_{gf}^{(*)})}{1 - \alpha (1 - \theta_{gf}^{(*)})} \right\},$$

and

$$\delta = \frac{[1 + \alpha (\theta_{gf}^{(*)} - 1)]^2}{\beta}.$$

Recalling that for free flames $\delta_0 = 1/\beta$ and recognizing that $\theta_{gf}^{(*)} = \theta_g^{(0)}(\zeta_f^+) = 1 + \eta_{rec}$, the ratio between the reaction length-scale for flames within porous media to that for free flames, considering $\lambda_g = \lambda_g^0$, is

$$\frac{l_R}{l_R^0} = \frac{s_F^0}{s_F} [1 + \alpha \eta_{rec}]^2. \quad (3.51)$$

As already discussed in the section describing the length-scales, the reaction region in flames within porous media is shorter than that for free flames. This is due to the increased gas-phase temperatures at the flame found in the combustion within porous media, resulting in higher reaction rates.

In the characteristic length-scale of the order of $\delta\Gamma^{-1}$ around the flame, the heat transfer from the gas-phase to the solid-phase is negligible ($\delta N/\gamma^2\Gamma \ll 1$) compared to the heat transfer in the solid-phase from the equilibrium zone to the frozen zone. Therefore, $\theta_s^{(1)} = C^{(1)}\eta$ and, from the energy conservation, $C^{(1)} = C_2^{(*)}/\gamma\Gamma$.

Following [87], an analysis of the system of equations (3.47) to (3.50) leads to the choice $\gamma = d_F$ and $p = \ln(2\bar{D}a_f)$. Then, this system of equations can be written as

$$\frac{1}{\phi} \frac{d_O}{d_F} \frac{d^2 y_O^{(1)}}{d\eta^2} = \frac{d^2 y_F^{(1)}}{d\eta^2} = \frac{d^2 \theta_g^{(1)}}{d\eta^2} = \frac{1}{2} y_F^{(1)} \exp[-(\theta_g^{(1)} + m\eta)]. \quad (3.52)$$

The mass fluxes d_F and d_O are defined for the upstream side as

$$-\left. \frac{1}{Le_F} \frac{dy_F^{(*)}}{d\xi} \right|_{\xi_f^-} = d_F \quad \text{and} \quad \left. \frac{1}{Le_O} \frac{dy_O^{(*)}}{d\xi} \right|_{\xi_f^-} = d_O,$$

and for the downstream side as

$$\left. \frac{1}{Le_F} \frac{dy_F^{(*)}}{d\xi} \right|_{\xi_f^+} = 0 \quad \text{and} \quad \left. \frac{1}{Le_O} \frac{dy_O^{(*)}}{d\xi} \right|_{\xi_f^+} = 0.$$

The heat flux at both sides of the flame, d_θ^- and d_θ^+ are defined as

$$\left. \frac{d\theta_g^{(*)}}{d\xi} \right|_{\xi_f^-} = d_\theta^- \quad \text{and} \quad \left. \frac{d\theta_g^{(*)}}{d\xi} \right|_{\xi_f^+} = -d_\theta^+.$$

The solution of the $O(\delta\Gamma^{-1})$ problem has to match the solution of the $O(\Gamma^{-1})$ problem, then, as $\eta \rightarrow -\infty$,

$$\frac{dy_F^{(1)}}{d\eta} = -1, \quad \frac{dy_O^{(1)}}{d\eta} = -1/\gamma, \quad \text{and} \quad \frac{d(\theta_g^{(1)} + m\eta)}{d\eta} = -d_\theta^-/\gamma, \quad (3.53)$$

and as $\eta \rightarrow \infty$,

$$\frac{dy_F^{(1)}}{d\eta} = 0, \quad \frac{dy_O^{(0)}}{d\eta} = 0 \quad \text{and} \quad \frac{d(\theta_g^{(1)} + m\eta)}{d\eta} = d_\theta^+/\gamma. \quad (3.54)$$

By choosing appropriately the value of $m = d_\theta^+/\gamma$, the heat flux is normalized, then

$$\left. \frac{d\theta_g^{(1)}}{d\eta} \right|_{\eta \rightarrow -\infty} = -1 \quad \text{and} \quad \left. \frac{d\theta_g^{(1)}}{d\eta} \right|_{\eta \rightarrow \infty} = 0. \quad (3.55)$$

From the conservation of energy at the flame $d_\theta^+ + d_\theta^- = d_F = \gamma$, then

$$m = d_\theta^+/(d_\theta^+ + d_\theta^-). \quad (3.56)$$

Combining the gas-phase energy and fuel conservation equations, Eq. (3.52), and applying the boundary conditions Eqs. (3.53) to (3.55), we obtain $\theta_g^{(1)} = y_F^{(1)}$. Thus, the problem in the reaction region reduces to finding the solution of

$$\frac{d^2 y_F^{(1)}}{d\eta^2} = \frac{1}{2} y_F^{(1)} \exp[-(y_F^{(1)} + m\eta)], \quad (3.57)$$

with the boundary conditions given by Eqs. (3.53) and (3.55). Since these boundary conditions impose only the derivatives of the function, the solution has to suffer a displacement in the coordinate axis in order to match with the solution of the second pre-heating region. By integrating Eq. (3.53), this displacement n is given by

$$n = \lim_{\eta \rightarrow -\infty} (y_F^{(1)} + \eta).$$

The displacement n has to be equal to the translation imposed in Eq. (3.46), $n = -p/m$. Then, from the definition of p , we have

$$\ln(2\bar{D}a_f) = -mn.$$

Substituting the Damköhler definition in the last expression and isolating s_F , we found the first-order estimative for the flame speed as follows

$$s_F^2 = \frac{2A\rho_f^2\lambda_g Y_{O_n} T_{gf}^a \exp(-\beta/\alpha)}{(\rho_n^2 c_p)} \left(\frac{\delta^2 L e_F (1 - \phi)}{d_F^2} \right) \times \exp \left\{ \frac{-\beta(1 - \theta_{gf}^{(*)})}{1 - \alpha(1 - \theta_{gf}^{(*)})} + m n \right\}, \quad (3.58)$$

in which

$$m n = 1.344m - 4m^2(1 - m)/(1 - 2m) + 3m^3 - \ln(1 - 4m^2), \quad \text{for } -0.2 < m < 0.5. \quad (3.59)$$

Equation (3.59) is an approximation of the numerical solution of Eq. (3.57) with the boundary conditions given by Eqs. (3.53) and (3.54) - see [87] for details. The value of m can be found from the solutions for the gas-phase temperature and is equal to

$$m = \frac{(1 + \eta_{rec})/2}{\varepsilon\Gamma/N + 1} = \frac{(1 + \eta_{rec})/2}{N_\varepsilon[\Gamma(1 - \varepsilon)/\varepsilon]/4 + 1}. \quad (3.60)$$

From Eq. (3.56), is possible to see that the parameter m is the ratio of the energy flux downstream from the flame, d_θ^+ , to the total energy released by the combustion process, $(d_\theta^- + d_\theta^+)$. Note that in combustion within a porous-medium, the value of m is bounded by $0 \leq m \leq 0.5$. The limit $m = 0$ corresponds to a freely propagating flame where there is no excess enthalpy. Thus, the excess of enthalpy requires $m > 0$. The limit $m = 0.5$ corresponds to a situation in which the heat loss to the equilibrium zone is equal to that to the frozen zone and under this condition the flame is not stable, i.e., there is extinction.

An expression for the flame velocity s_F divided by the laminar free-flame velocity

s_F^0 [Eq. (3.58) with $m = 1 - \varepsilon = 1 - \theta_{gf}^{(*)} = 0$] is obtained as

$$\left(\frac{s_F}{s_F^0}\right)^2 = (1 + \alpha\eta_{rec})^{a+2} \exp\left(\frac{\beta\eta_{rec}}{1 + \alpha\eta_{rec}} + mn\right). \quad (3.61)$$

In this compact result, the effect of the porous media on the flame velocity is found to be a function of N_ε , Γ and ε only. The effect of ϕ and Le_F is included in the free-flame parameters s_F^0 , α and β .

3.3.5 Model summary

A closed form approximate solution for the structure and propagation velocity of adiabatic stationary premixed flames in porous inert media is obtained. The temperature profile of the solid-phase is given by Eq. (3.19), in which the temperature of the solid-phase at the flame, given by Eq. (3.20) is used. The temperature profile of the gas-phase is described by Eqs. (3.21), (3.40), (3.43) and (3.45). The fuel and oxidant consumption profiles are given by Eqs. (3.38) and (3.39). The heat recirculation efficiency is given by Eq. (3.25). The flame velocity is evaluated by Eq. (3.58), in which Eqs. (3.59) and (3.60) are used. Under the considered hypothesis, a parameter that universalizes the flame properties for the premixed combustion in porous media is given by Eq. (3.27).

This set of equations predicts, under the simplifying assumptions used, the main characteristics of flames in porous media for $N \ll \Gamma$ and $\varepsilon/(1 - \varepsilon) \sim O(1)$. In the next section the model will be explored to evaluate the influence of the equivalence ratio, the ratio of the solid-phase thermal conductivity to that of the gas-phase, the porosity of the medium and the fuel Lewis number on such flames.

3.4 Discussion

The reaction rate parameters were adjusted to give a reasonable agreement with measured laminar flame speeds for methane-air free flames with equivalence ratios ranging from 0.6 to 0.8 [93]. A constant volumetric heat transfer coefficient h_v is estimated following Fu et al. [21]. The gas-phase properties were approximated by the air properties evaluated at 1300 K. The heat of reaction was adjusted to reproduce the adiabatic flame temperature for $\phi = 0.8$. Transport and geometric properties of the solid-phase are typical of porous burners [2, 26]. Table 3.1 shows the parameters and properties used in the calculations. Results for $\phi = 0.8$, $\Gamma = 60$, $\varepsilon = 0.8$ and $Le_F = 1$ are also shown as an example. For simplicity, the fuel Lewis number is equal to unity for all the calculated results, except when its effect on the heat recirculation efficiency is analyzed.

The model is valid for $\varepsilon/(1 - \varepsilon) \sim O(1)$. Nevertheless, good results are found even for porosities as high as 0.8, as will be shown in this section. Another condition imposed is $N \ll \Gamma$. This will not hold for extremely lean mixtures where lower flame velocities are found and the interphase heat transfer at the gas-phase diffusion length-scale becomes important. This is the reason why the discussion will be restricted to $\phi \geq 0.6$. The model fails for equivalence ratios near unity because, in this case, the oxidant concentration $(1 - \phi)$ in Eq. (3.58) tends to zero. In order to reach the stoichiometric mixture it would be necessary to solve the first correction for the oxidant mass fraction $y_O^{(1)}$. This is the reason why the discussion will be additionally restricted to $\phi \leq 0.8$.

Table 3.1: Properties and parameters used in the calculations and results for $\varepsilon = 0.8$, $\phi = 0.8$, $\Gamma = 60$ and $Le = 1$.

Properties and Parameters			Results		
R_u	8.314	$\text{J}(\text{mol K})^{-1}$	λ_s	4.783	$\text{W}(\text{m K})^{-1}$
E_a	1.77×10^5	J mol^{-1}	T_r	1996	K
A	2.20×10^{12}	$\text{m}^3(\text{kg s})^{-1}$	T_{gf-}	698	K
a	0		T_{gf+}	2388	K
Q	4.525×10^7	J kg^{-1}	T_{sf}	1343	K
c_p	1187	$\text{J}(\text{kg K})^{-1}$	s_F	0.82	m s^{-1}
λ_g	0.0797	$\text{W}(\text{m K})^{-1}$	α	0.85	
ρ_n	1.185	kg m^{-3}	β	9.07	
h_v	2.0×10^5	$\text{W}(\text{m}^3 \text{K})^{-1}$	N	0.718	
T_n	298	K	N_ε	17.83	
ε	0.8		\overline{Da}_f	0.494	
ϕ	0.8		m	9.06×10^{-3}	
Γ	60		n	1.344	
Le_F	1		η_{rec}	0.2304	
			δ	0.1577	

3.4.1 Flame structure

Figure 3.2 shows the flame structure for $\phi = 0.8$, $\Gamma = 60$ and $\varepsilon = 0.8$ as a function of the transformed space coordinate ζ . The range used for the spatial scale represents the solution of the problem of $O(1)$, in which the solid conduction, the gas convection and the interphase heat transfer are the dominant processes. The flame can be seen as a sheet where the fuel mass fraction and gas temperature profiles are discontinuous. Upstream from the flame there is the first pre-heating region and downstream from the flame there is the re-equilibrium region. For these conditions the gas temperature exceeds the adiabatic limit by 23%, which corresponds to the heat recirculation efficiency given by Eq. (3.25). Figure 3.3 shows the same result as Fig. 3.2 with a

range for the spatial scale that represents the solution of the problem of $O(\Gamma^{-1})$. It is possible to observe the solution in the second pre-heating region connecting the discontinuous profiles of $\theta_g^{(0)}$ and $y_F^{(0)}$ across the flame. Note that the first derivatives of both curves are discontinuous since the solution of the innermost scale provides an expression for the flame velocity only. Comparing Figs. 3.2 and 3.3 it is seen that the thermal affected region, i.e., the sum of the lengths of the first pre-heating region and the re-equilibrium region (which corresponds to l_S), is much larger than the second pre-heating region (l_G), as a consequence of the high thermal conductivity of the solid matrix.

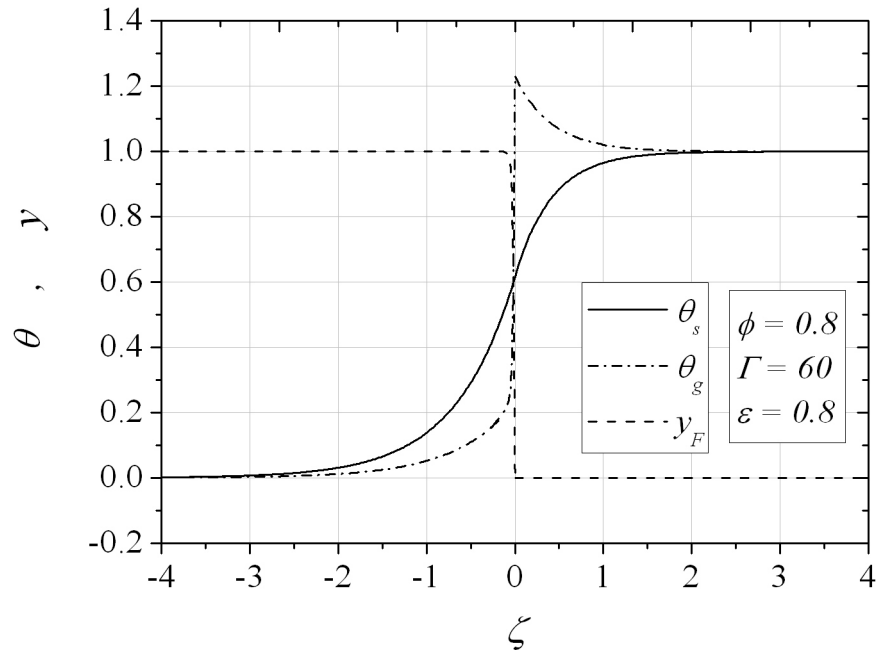


Figure 3.2: Non-dimensional gas- and solid-phase temperatures and fuel mass fraction profile (solution of the $O(1)$ problem).

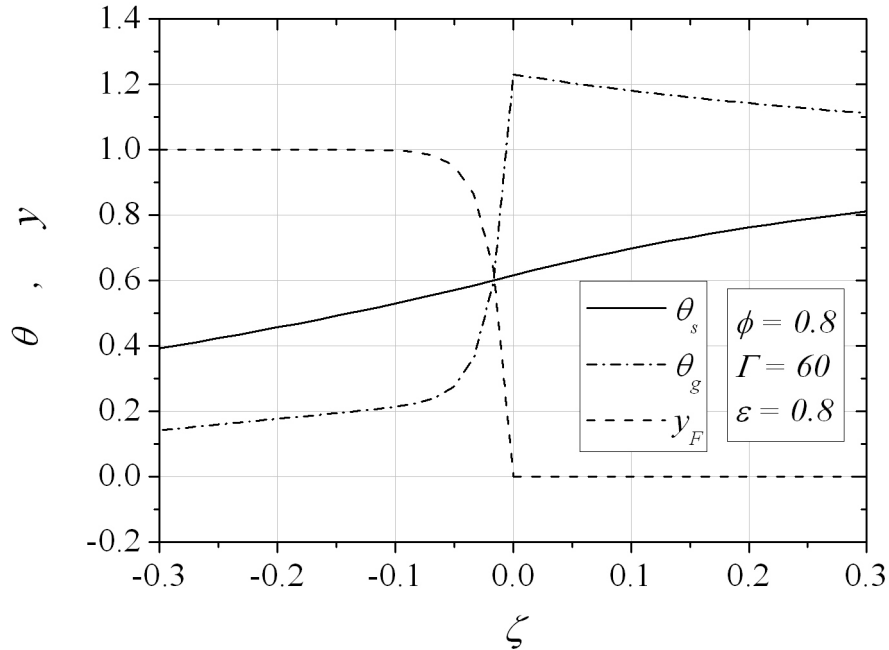


Figure 3.3: Non-dimensional gas- and solid-phase temperatures and fuel mass fraction profile (solution of the $O(\Gamma^{-1})$ problem).

3.4.2 Influence of the equivalence ratio and Γ

Figure 3.4 shows the interphase heat transfer parameter N as a function of Γ and ϕ for $\varepsilon = 0.8$. The increase of N with the increasing values of Γ is in accordance with the definition of N , since the heat transfer parameter is proportional to Γ via the solid-phase conductivity λ_s . Also, for any Γ , the heat transfer parameter N decreases as ϕ increases. This can be understood by recalling that N is proportional to $1/s_F^2$ and that higher flame velocities are found for higher equivalence ratios. Then, higher values of N are found for leaner mixtures and higher solid-phase thermal conductivities. Note, however, that for $\Gamma = 20$ and $\varepsilon = 0.8$ the results are at the limit for the validity of the model.

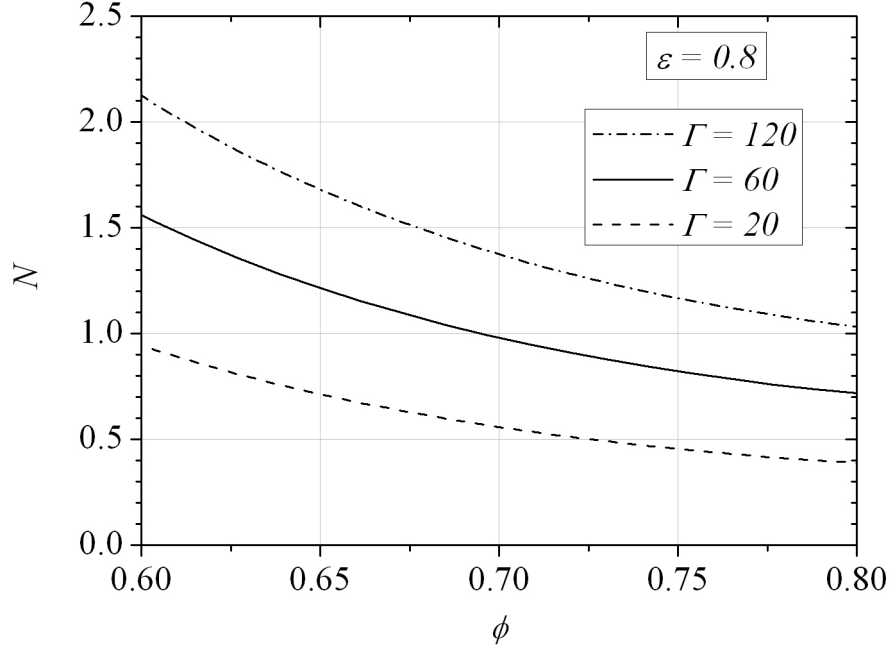


Figure 3.4: Interphase heat transfer parameter N as a function of ϕ and Γ .

Figures 3.5 to 3.8 show the effect of Γ and ϕ on other flame parameters. The solid-phase temperature at the flame $\theta_s^{(0)}(\zeta_f)$, depicted in Fig. 3.5, is proportional to \sqrt{N} according to Eq. (3.20). Then, $\theta_s^{(0)}(\zeta_f)$ also increases for leaner mixtures and higher solid-phase thermal conductivities. In the range of analysis, it varied from 0.59 to 0.69, agreeing with the limits $1/2 < \theta_s^{(0)}(\zeta_f) < 1$, as already pointed out.

The heat recirculation efficiency η_{rec} , shown in Fig. 3.6, is also proportional to \sqrt{N} , according to Eqs. (3.26) and (3.27). Then, η_{rec} increases as Γ increases and as ϕ decreases. Note that η_{rec} also represents the gas-phase temperature at the upstream side of the flame, $\theta_g^{(0)}(\zeta_f^-)$, or the excess temperature in the gas-phase at the downstream side of the flame, $\theta_g^{(0)}(\zeta_f^+) = 1 + \eta_{rec}$ as stated by Eqs. (3.28) and (3.29). In the range of analysis, the maximum gas temperature at the flame is 17 to 38%

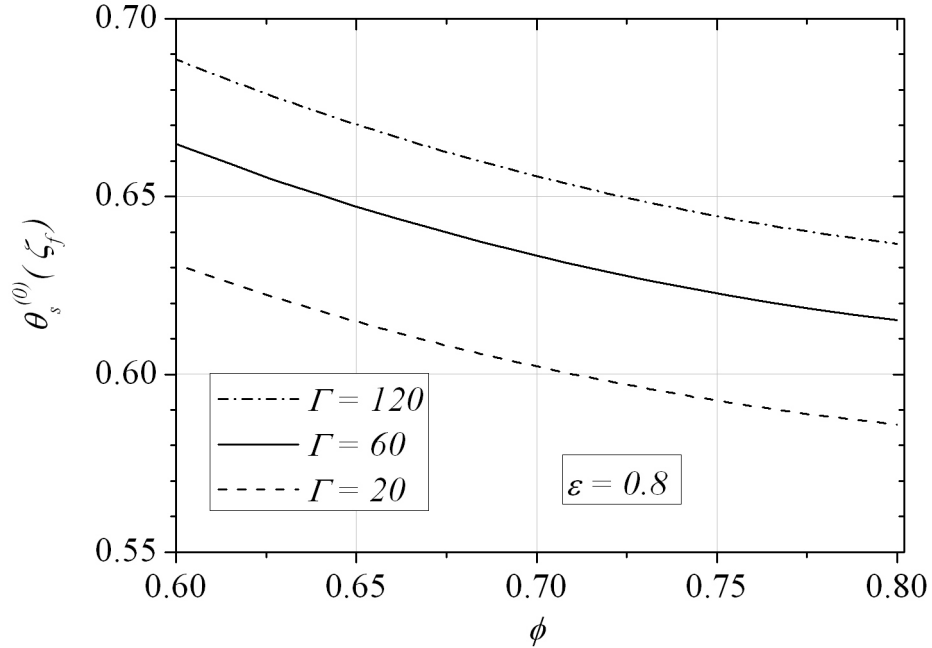


Figure 3.5: Non-dimensional solid-phase temperature at the flame $\theta_s^{(0)}(\zeta_f)$ as a function of ϕ and Γ .

higher than the adiabatic flame temperature, or, in other words, 17 to 38% of the total energy released by the combustion process has been recirculated to the unburnt gases. Previous works [70, 69] have shown that the use of one-step global mechanisms for the chemical kinetics over-predicts the superadiabatic flame temperatures for equivalence ratios near stoichiometry. For leaner mixtures such mechanisms yield better results.

The same trends are found for the ratio s_F/s_F^0 , Eq. (3.61), shown in Fig. 3.7. The ratio s_F/s_F^0 increases as the equivalence ratio is decreased since higher recirculation efficiencies are found. This occurs since, due to higher heat recirculation, the flame reaches (proportionally) higher gas-phase temperatures with respect to the adiabatic limit, leading to higher flame velocities with respect to the laminar free-flame velocity

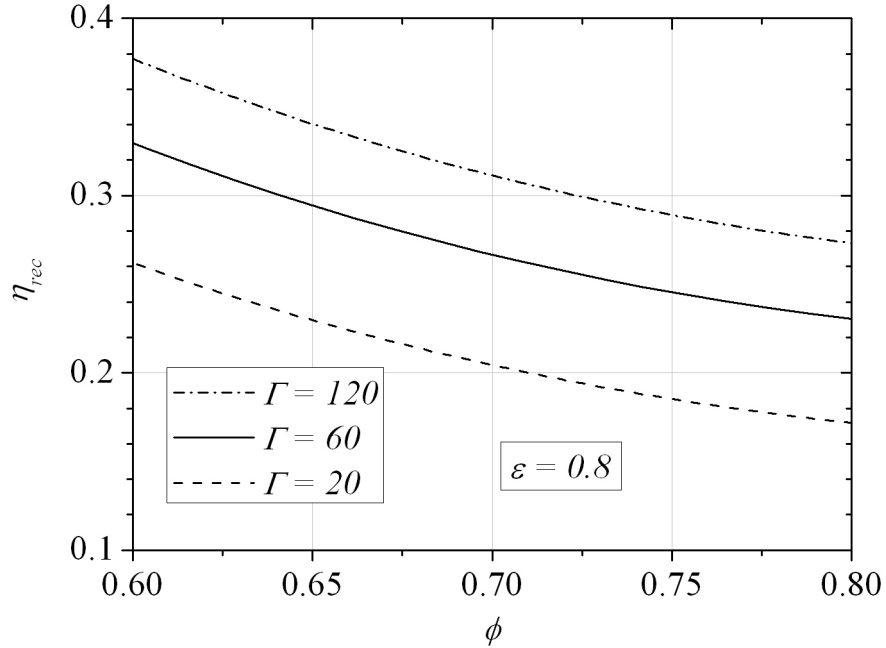


Figure 3.6: Heat recirculation efficiency η_{rec} as a function of ϕ and Γ .

s_F^0 . In the range of analysis, s_F is 2.3 to 6.5 times larger than the corresponding free flame velocity. Note that, in order to calculate the mass flow rate for flames in porous media, m_g , one must consider the effect of the reduced area to the gas-phase flow through the solid matrix. Then, $m_g/m_g^0 = \varepsilon s_F/s_F^0$, where m_g^0 is the mass flow rate for free flames.

Figure 3.8 shows the ratio l_R/l_R^0 , i.e., the reaction length-scale for flames within porous media non-dimensionalized by the reaction length-scale for free flames, as a function of ϕ and Γ . The reaction region for flames within porous media is shorter when the heat recirculation is higher as a result of the increase in the flame velocity (one should remember that in Eq. (3.51) s_F increases with η_{rec}). In the range of analysis, l_R varies between 26 to 57% of l_R^0 .

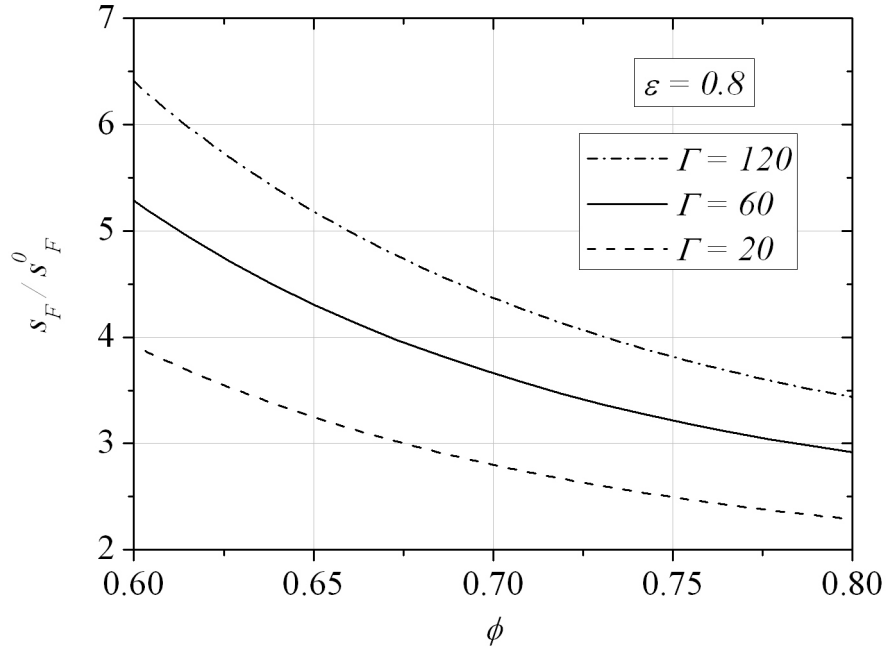


Figure 3.7: Ratio s_F / s_F^0 as a function of ϕ and Γ .

3.4.3 Influence of the matrix porosity

Figures 3.9 and 3.10 show the effect of the porosity ε on the flame parameters for $\phi = 0.8$ and $\Gamma = 60$. As ε is decreased, the effect of the solid-phase becomes more important since there is more solid-phase in the matrix. As a consequence, more heat is transported by the solid, thus increasing the heat recirculated, as depicted in Fig. 3.9. This can be seen examining the dependence of η_{rec} with ε in Eqs. (3.26) and (3.27). When ε tends to unity, η_{rec} tends to zero and when ε tends to zero η_{rec} tends to unity. Nevertheless, when ε tends to unity the intramedium radiation heat transfer becomes more important and the Rosseland approximation could not be assumed. Since the heat recirculation increases for lower porosities, l_R decreases and $\theta_s^{(0)}(\zeta_f)$

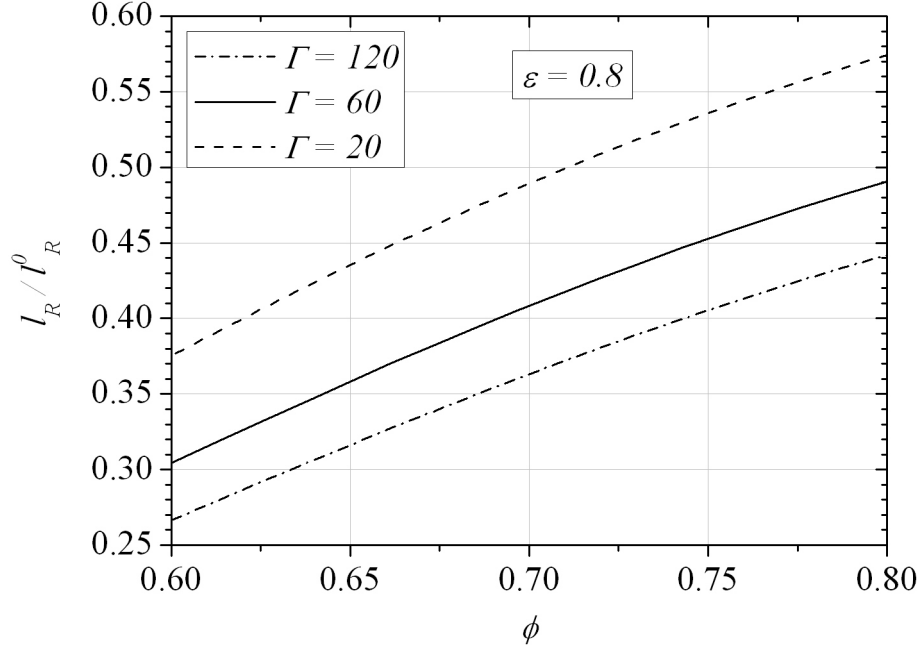


Figure 3.8: Ratio l_R/l_R^0 as a function of ϕ and Γ .

increases. The same tendency is found for the ratio s_F/s_F^0 in Fig. 3.10, i.e., the flame velocity increases as ε decreases as a result of the higher heat recirculation. The heat transfer parameter N decreases when the porosity is decreased since it is proportional to $1/s_F^2$.

When $\varepsilon \rightarrow 1$ the model tends to the free flame solution, i.e., the temperature at the downstream side of the flame, $\theta_g^{(0)}(\zeta_f^+)$, is unity over the entire range of ϕ , $\theta_s^{(0)}(\zeta_f)$ is $1/2$, its lower value according to Eq. (3.20), the flame velocity equals the adiabatic free flame velocity ($s_F = s_F^0$), the reaction length-scale equals the free flame reaction length-scale ($l_R = l_R^0$) and, as was already seen above, η_{rec} tends to zero. Nevertheless, in this limit, the solid temperature and the heat recirculation are

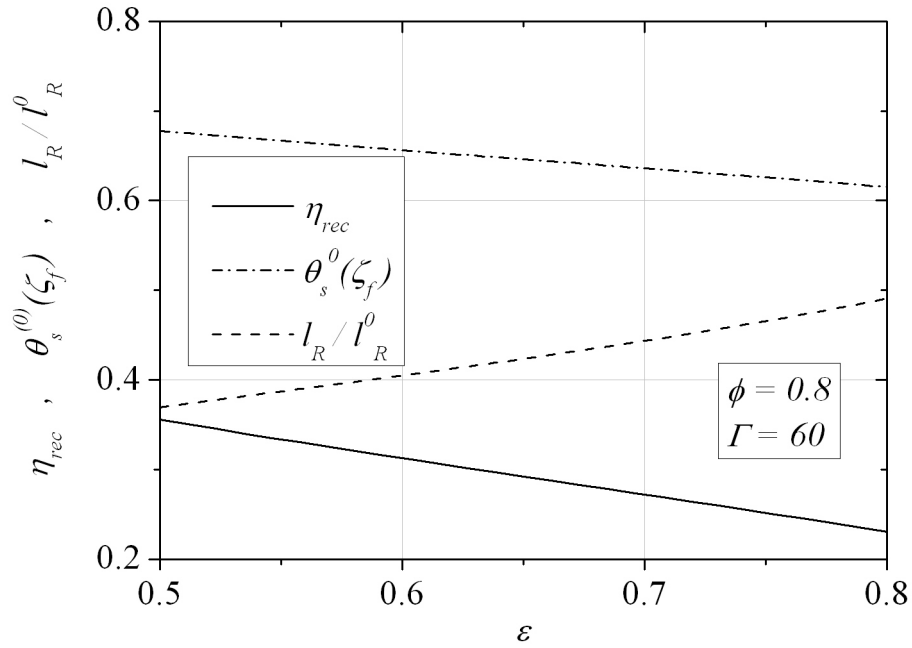


Figure 3.9: Dependence of η_{rec} , $\theta_s^{(0)}(\zeta_f)$ and l_R/l_R^0 on ε .

meaningless since there is no interphase heat exchange. Although these tendencies are correct, the model is not valid in this limit.

3.4.4 Influence of the Lewis number

Until now the discussion was restricted to $Le_F = 1$. The effect of a different fuel Lewis number on the heat recirculation efficiency is shown in Fig. 3.11. The heat recirculation efficiency slightly increases as Le_F decreases. This occurs because s_F decreases as Le_F is decreased, according to Eq. (3.58), thus leading to higher values of N and η_{rec} .

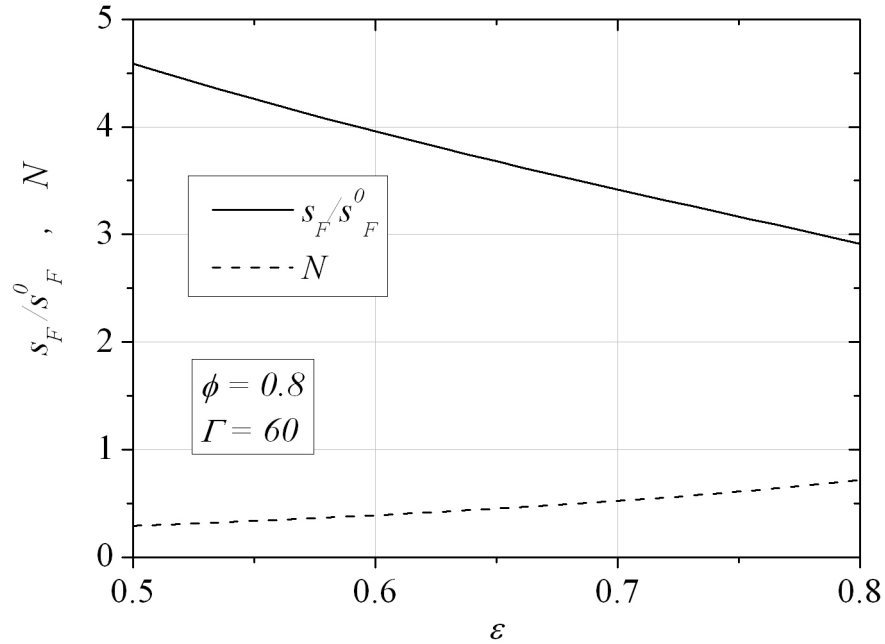


Figure 3.10: Dependence of the ratio s_F/s_F^0 and N on ε .

3.4.5 The porous-media-flame number

Therefore, in the range of analysis, the characteristics of the superadiabatic combustion in porous media will be more pronounced for lower equivalence ratios, higher solid-phase conductivities, lower matrix porosities and lower fuel Lewis numbers. Combinations among these four parameters define the heat recirculation induced by the matrix and, consequently, the superadiabatic effect. Under the hypotheses considered, the porous-media-flame number N_ε , given by Eq. (3.27), summarizes these effects and defines the state of reacting flows within porous media. Figure 3.12 shows the variation of ε with Γ and ϕ for $N_\varepsilon = 20$. As indicated at the caption, the data shown in the figure have identical values of the variables at the flame,

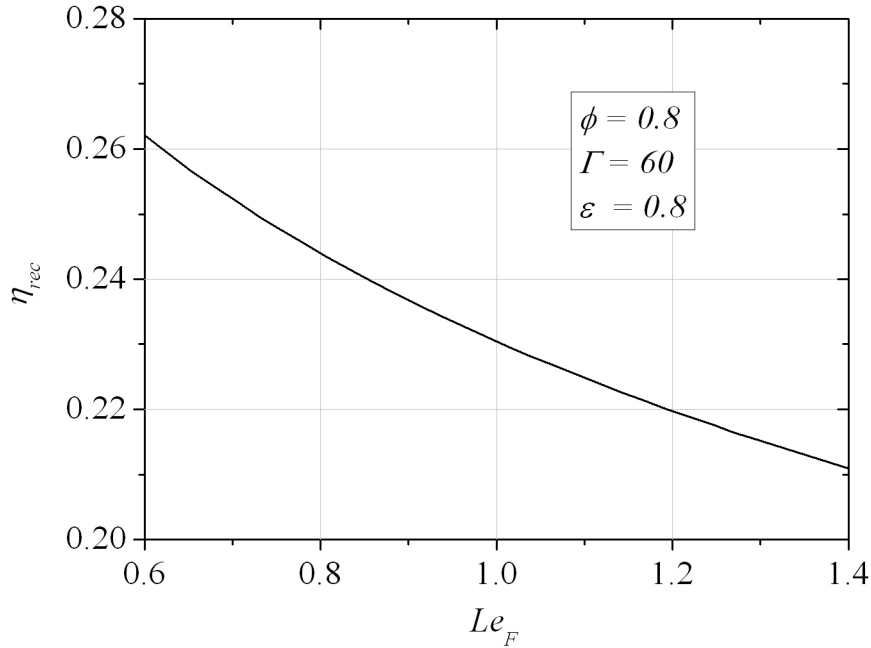


Figure 3.11: Heat recirculation efficiency η_{rec} as a function of Le_F .

$$\eta_{rec} = \theta_g(\zeta_f^-) = 0.218, \theta_g(\zeta_f^+) = 1.218 \text{ and } \theta_s(\zeta_f) = 0.609.$$

3.4.6 Comparison with a numerical solution

Figure 3.13 shows a comparison between the present model and a numerical solution of Eqs. (2.39) to (2.43) for $\phi = 0.8$, $\Gamma = 60$, $\varepsilon = 0.8$ and $Le_F = 1$. The numerical solution was obtained using a finite-volume method, with non-uniform adapting grid and steps were taken to accelerate convergence to steady-state [94]. The flame speed (eigenvalue) was obtained from the overall mass balance. The algorithm used the same properties and parameters listed in Table 3.1. From Fig. 3.13, it is observed that the asymptotic model overestimates the heat recirculation and the gas-phase

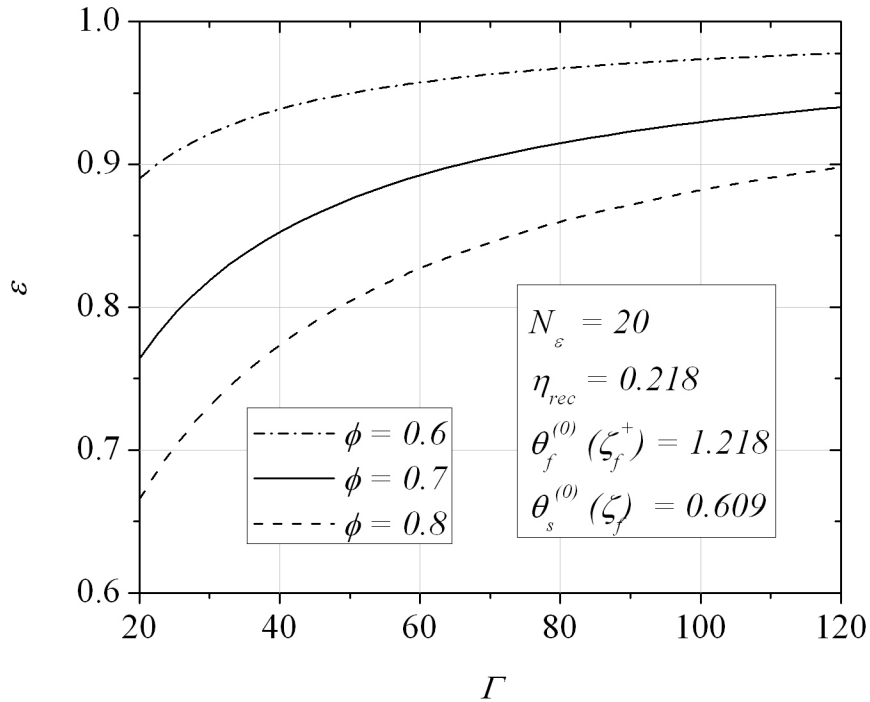


Figure 3.12: Variation of ε with Γ and ϕ for $N_\varepsilon = 20$.

temperature at the flame. The flame velocity calculated numerically is 25% larger than the analytical prediction. The discrepancies between the two solutions are due to the simplifications assumed in the asymptotic model. For instance, in the problem of the order of unity, the thermal diffusion is neglected in the gas-phase. This approximation fails near the flame, where considerable temperature gradients occur, and could explain the observed discrepancies. As a result of this simplification, the temperature of the gas-phase in the upstream side of the flame and, consequently, the heat recirculation, are over-estimated by the analytical model. Furthermore, in the problem of the order of Γ^{-1} , the surface convection has been neglected, then, at the downstream side of the flame, the gas-phase temperature is also over-estimated

because of the high heat recirculation and the reduced heat loss to the solid-phase. Nevertheless, even with a higher temperature at the flame, the analytical model predicts a lower flame velocity. This may be due to the simplifications inherent to the high activation energy asymptotic method employed to analyze the reaction region. In the framework of the simple one-step reaction model, a rough approximation of the flame velocity could be expected only. Nevertheless, the analytical model is able to qualitatively follow the main characteristics of the flame. Note also that in Fig. 3.13 the profiles are shown against the non-dimensional spatial variable ζ , that is a function of the flame velocity. Figure 3.14 brings the comparison in dimensional variables, showing that the solid-phase temperature is fairly well predicted by the analytical model. The quality of the solution could be improved by solving additional terms of the asymptotic expansion Eq. (3.10). Nevertheless, this improvement is of minor interest in the context of the present work. An extension of this work with a more detailed model for the chemical kinetics, e.g., a four-step kinetic model, would improve the results.

3.5 Conclusions

This chapter presented an asymptotic solution for an infinite, adiabatic porous burner considering three different characteristic length-scales: the solid-phase diffusion length-scale (l_S), where the solid-phase heat conduction, gas-phase convection and interphase heat transfer dominate the problem, the gas-phase diffusion length-scale (l_G), where the gas-phase convection and diffusion dominate the problem, and the reaction length-scale (l_R), where reaction and gas-phase diffusion dominate the problem. Explicit solutions for the gas and solid temperatures and for the fuel and oxidant consumption

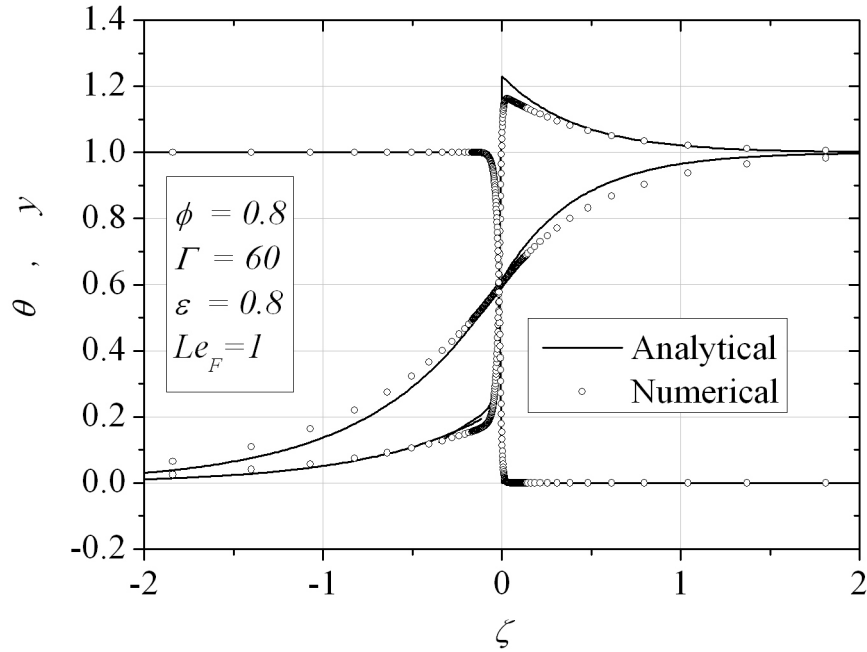


Figure 3.13: Comparison of the present model to a numerical solution.

were found as function of the problem parameters for the l_S and l_G characteristic length-scales. The description of the problem in the reaction length-scale leads to an approximated expression for the flame velocity.

The model was used to analyze the influence of the equivalence ratio ϕ , the conductivities ratio Γ , the matrix porosity ε and the fuel Lewis number Le_F on the flame structure. The combinations among these four parameters define the heat recirculation induced by the matrix and, consequently, the superadiabatic effect. The results showed that the influence of the porous medium on the flame is to increase its temperature and velocity. That influence is more pronounced for leaner mixtures, higher solid-phase thermal conductivities (higher Γ), lower porosities and lower fuel Lewis numbers. Under the hypotheses considered in this work, a number that brings

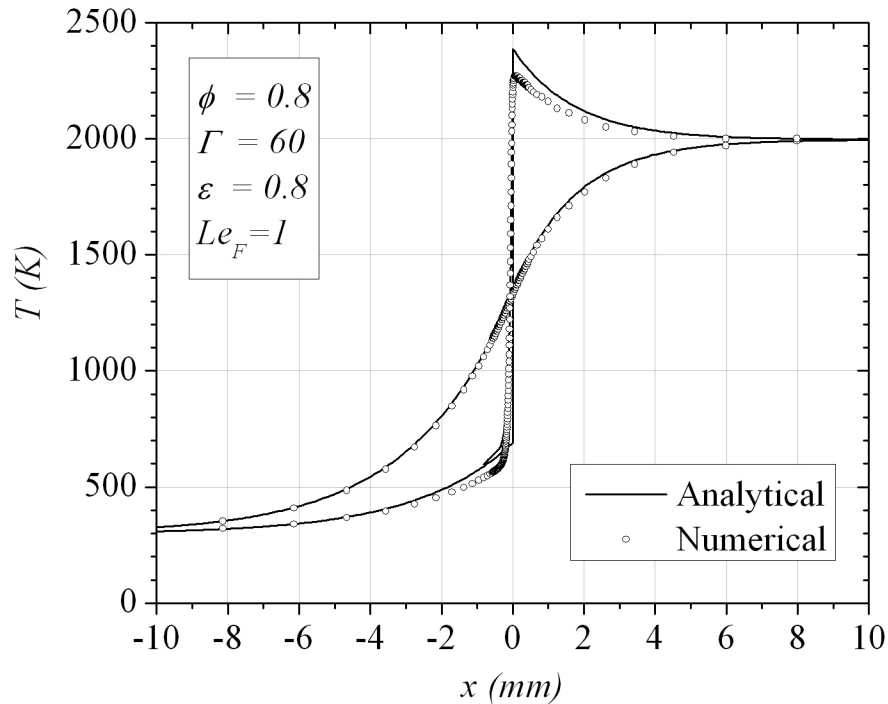


Figure 3.14: Comparison of the present model to a numerical solution in dimensional variables.

together the effects of all these parameters, characterizing the flame variables and universalizing the results, is identified. For this reason, this number is called the porous-media-flame number.

The thermal affected region (l_S) is larger than the gas-phase diffusion length-scale (l_G) as a result of the high thermal conductivity of the solid matrix. For example, maximum gas-phase temperatures up to 38% above the corresponding adiabatic free-flame temperature and flame velocities up to 6.5 times the corresponding adiabatic free-flame velocity are found for $\phi = 0.6$, $\Gamma = 120$, $\varepsilon = 0.8$ and $Le_F = 1$. It is also shown that the reaction region is shorter in flames within porous media, $l_R < l_R^0$,

since higher flame temperatures are found.

Due to the simplifications assumed by the model, the solution fails for extremely lean mixtures, when the heat transfer parameters N is large, for equivalence ratios near unity, because of the simplified solution for the reaction region, and for very high porosities ($\varepsilon \rightarrow 1$), since, in this case, the scale separation assumed by the model is not applicable. These limits will be addressed in the next chapters.

Chapter 4

Asymptotic solution for ultra-lean mixtures

In this chapter, the method of matched asymptotic expansions is employed to the case of extremely lean mixtures, where the interphase heat transfer is intense.

4.1 Introduction

Ultra-lean premixed flames within infinite adiabatic porous inert media are characterized by low flame velocities that result in intense interphase heat transfer, which in turn leads to thermal equilibrium between the gas and solid phases in a wide region around the flame. The present analysis will show that this thermal equilibrium limits the superadiabatic effect and will reveal thermal aspects of the lean flammability limit for the flame propagation in porous inert media.

There is a lack of studies concerning the steady-state ultra-lean operation of porous burners [5]. In an experimental and numerical study of radiant porous burners performance, Hsu et al. [13] obtained stable flames at equivalence ratios as low as 0.41 for methane-air flames, which is smaller than the lean flammability limit for free

methane-air flames, $\phi = 0.46$ [68]. The results showed that there is a decreasing flow rate range where stable flames can be sustained as the mixture is made leaner. Below a certain value of the equivalence ratio ($\phi \leq 0.55$) the burner heat loss was the dominating factor in determining the minimum flow rate for stable flames. In these cases, the flame did not present flash-back, instead, it just extinguished when the flow rate was decreased. Although the experiments could not reach the flammability limit, the authors hypothesized that at this limit there is only one flow rate that leads to a stable flame. For this flow rate, the energy released by the combustion process is just large enough to yield the temperature required to maintain the chemical reactions. This means that, for the ultra-lean operation of radiant burners, the lean flammability limit is determined by a balance between heat losses and heat recirculation. Experimental and numerical studies report stable flames below the standard free-flame lean flammability limit [12, 17, 51, 95]. It is expected that, for perfectly adiabatic burners, the lean limit for the flame propagation will be found for much lower equivalence ratios than in radiant burners. Other experimental works report ultra-lean combustion in porous inert media [8, 11, 96], but some kind of external heat recirculation is used.

Ultra-lean combustion is also achieved in low-velocity forward filtration combustion in porous inert media [36, 97]. In these cases the reaction front propagates at low velocities (less than 1 mm/s) and the flame can be sustained for equivalence ratios as low as 0.15. The interaction of the combustion wave with the thermal wave can lead the flame to reach temperatures as high as 2.8 times the corresponding adiabatic flame limit [36]. This is not the case for stationary flames. As it will be shown in the present analysis, the nondimensional flame temperature based on the thermodynamic

limit decreases as the flammability limit is approached.

In the ultra-rich side of the equivalence ratio range, Schoegl and Ellzey [98] developed an analytical model for the combustion of methane-air mixtures in conducting tubes of finite length. Co-flow and counterflow configurations in parallel tubes were evaluated. Stable solutions were obtained for equivalence ratios up to 2.8 in the counter-flow case, which is far beyond the standard rich flammability limit for methane-air flames ($\phi = 1.64$ [68]). Two solutions were obtained, one corresponding to high flame velocities and the other corresponding to slow flames velocities. The rich flammability limit for the two configurations was not determined, but the results showed that the range of flow rates in which stable flames are obtained decreases as the equivalence ratio is increased.

In the previous chapter, an asymptotic solution was proposed for equivalence ratios ranging from 0.60 to 0.80. The upper bound was the result of the simplifications involved in the one-step kinetic mechanism used. The lower bound is related to interphase heat transfer parameter that was not allowed to increase, i.e., $N \ll \Gamma$. For small values of N , the interphase heat transfer at the gas-phase and at the reaction length-scales is negligible. Then, the flame structure at the inner scales is similar to that of a free-flame. This will not hold for extremely lean mixtures where lower flame velocities are found.

This chapter aims to extend the previous results to lower equivalence ratios where the condition $N \sim O(\Gamma)$ prevails. Higher values of N result in local thermal equilibrium between the phases in a wide region around the flame. This intense interphase heat transfer limits the superadiabatic effect, showing that the superadiabatic flame temperature should have a maximum at the lean side of the equivalence ratio range.

The model also provides a first approximation for the lean flammability limit for the flame propagation in adiabatic porous inert media based on thermal considerations. In this case, since there is no influence of heat losses, the lean flammability limit is determined only by the heat recirculation that is a function of the solid- and gas-phase properties.

4.2 Length scales

Figure 4.1 shows a schematic representation of the problem under consideration. Since we are dealing with extremely lean mixtures with very low flame velocities, the gas and solid phases have enough contact time to reach thermal equilibrium in a wide region around the flame. This region corresponds to the characteristic solid-phase diffusion length-scale l_S . In a thin region around the flame there is still considerable thermal nonequilibrium between the phases. This region corresponds to the characteristic gas-phase diffusion length-scale l_G . The ratio between these two scales is $l_G/l_S = \varepsilon/\Gamma(1-\varepsilon)$. As in the previous work, the present model is restricted to $\varepsilon/(1-\varepsilon) \sim O(1)$, ensuring the scales separation ($l_G/l_S = 1/\Gamma$).

As the equivalence ratio decreases, the large contact time between the phases causes an intense heat transfer from the gas-phase to the solid-phase at the length-scale l_G . Then, contrary to the previous model, the nondimensional flame temperature decreases as the mixture is made leaner. Since the flame velocity is proportional to the Lewis number, the same results are found when the Lewis number is decreased. These behaviors are particular of ultra-lean premixed combustion in porous inert media. This is due to a change in the direction of the interphase heat transfer. In the previous model, the interphase heat transfer is important just at the solid-phase

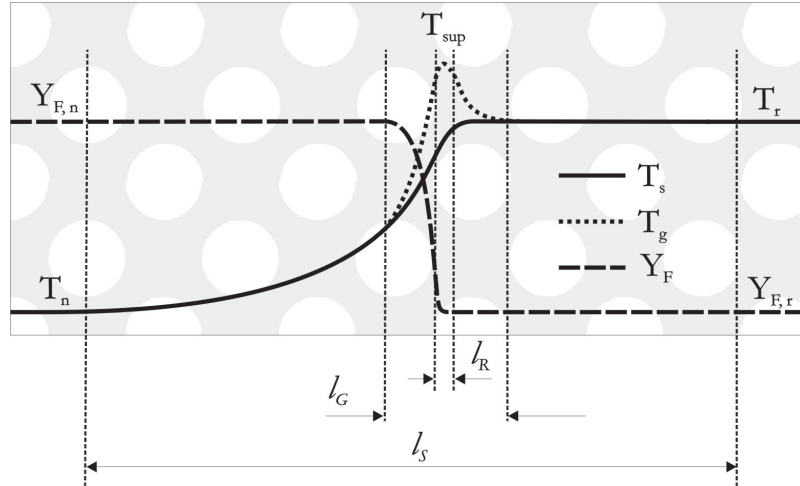


Figure 4.1: Schematic representation of the temperatures and fuel mass fraction distributions and the different characteristic length-scales of the problem.

length-scale l_S where the solid-phase loses heat to the gas-phase. In the present model, the interphase heat transfer in the gas-phase length-scale l_G is not negligible, and now is the gas-phase that loses heat to the solid-phase. This change in the heat transfer direction is the origin of the particular behavior of the ultra-lean combustion in porous inert media.

The description of the reaction region l_R is identical to the previous model since the interphase heat transfer in this region is still negligible. As in the previous model, the two innermost scales behave as a subgrid model, with the difference that now the interphase heat transfer at the gas-phase scale is no longer negligible.

4.3 Mathematical formulation

The nondimensional conservation equations obtained in the previous chapter, Eqs. (3.1) to (3.4), are the starting point of the present analysis.

4.3.1 Outer zone: problem of the order of unity

In the characteristic length scale $\zeta - \zeta_f \sim O(1)$, the diffusive terms in the gas-phase are of the order of Γ^{-1} , the interphase heat transfer parameter N is of the order of Γ and the reaction is exponentially small. Thus, Eqs. (3.1) to (3.4) take the form

$$\varepsilon \frac{dy_F}{d\zeta} = \frac{\varepsilon}{Le_F \Gamma} \frac{d^2 y_F}{d\zeta^2}, \quad (4.1)$$

$$\varepsilon \frac{dy_O}{d\zeta} = \frac{\varepsilon}{Le_O \Gamma} \frac{d^2 y_O}{d\zeta^2}, \quad (4.2)$$

$$\varepsilon \frac{d\theta_g}{d\zeta} = \frac{\varepsilon}{\Gamma} \frac{d^2 \theta_g}{d\zeta^2} + N(\theta_s - \theta_g), \quad (4.3)$$

$$0 = (1 - \varepsilon) \frac{d^2 \theta_s}{d\zeta^2} - N(\theta_s - \theta_g). \quad (4.4)$$

The solution of Eqs. (4.1) to (4.4) can be written as

$$\left. \begin{aligned} y_F &= y_F^{(0)} + \Gamma^{-1} y_F^{(1)} + o(\Gamma^{-1}) \\ y_O &= y_O^{(0)} + \Gamma^{-1} y_O^{(1)} + o(\Gamma^{-1}) \\ \theta_s &= \theta_s^{(0)} + \Gamma^{-1} \theta_s^{(1)} + o(\Gamma^{-1}) \\ \theta_g &= \theta_g^{(0)} + \Gamma^{-1} \theta_g^{(1)} + o(\Gamma^{-1}) \end{aligned} \right\}. \quad (4.5)$$

Substituting Eq. (4.5) into Eq. (4.1) to (4.4) and applying the limit $\Gamma \rightarrow \infty$ ($N \rightarrow \infty$), the first approximation for the set of equations of the order of unity is

$$\frac{dy_F^{(0)}}{d\zeta} = 0, \quad (4.6)$$

$$\frac{dy_O^{(0)}}{d\zeta} = 0, \quad (4.7)$$

$$\theta_s^{(0)} = \theta_g^{(0)} = \theta^{(0)}. \quad (4.8)$$

The boundary conditions for $\zeta \rightarrow -\infty$ are $\theta^{(0)} = 0$ and $y_F^{(0)} = y_O^{(0)} = 1$ and for $\zeta \rightarrow +\infty$ are $\theta^{(0)} = 1$ and $y_F^{(0)} = y_O^{(0)} - (1 - \phi) = 0$. The solution for Eqs. (4.6) and (4.7) are $y_F^{(0)} = y_O^{(0)} = 1$ for $\zeta < \zeta_f$ and $y_F^{(0)} = 0$ and $y_O^{(0)} = 1 - \phi$ for $\zeta > \zeta_f$.

Summing up Eq. (4.3) and (4.4) with thermal equilibrium, Eq. (4.8), one finds

$$\frac{d\theta^{(0)}}{d\zeta} = \left(\frac{1 - \varepsilon}{\varepsilon} \right) \frac{d^2\theta^{(0)}}{d\zeta^2}. \quad (4.9)$$

Equation (4.9) is equivalent to the one-equation model for the energy conservation with effective properties [44]. Integrating Eq. (4.9) and applying the proper boundary conditions, one finds the first approximation for the temperature profile in the region with thermal equilibrium between the two phases

$$\theta^{(0)} = \begin{cases} \exp\{(\zeta - \zeta_f) [\varepsilon/(1 - \varepsilon)]\}, & \text{for } \zeta \leq \zeta_f, \\ 1, & \text{for } \zeta \geq \zeta_f. \end{cases} \quad (4.10)$$

Note that, since local thermal equilibrium is assumed in this scale, superadiabatic flame temperatures are not possible. This solution is similar to a free-flame solution with the mean properties of an homogeneous medium composed by the gas and the solid phases. Equation (4.10) is the kind of solution obtained when the one-equation model for the energy conservation is employed to solve the problem of combustion within porous inert media.

Now, collecting the terms of the order of Γ^{-1} one finds the equation for the first correction for the temperature as

$$\left(\frac{1 - \varepsilon}{\varepsilon} \right) \frac{d^2\theta^{(1)}}{d\zeta^2} - \frac{d\theta^{(1)}}{d\zeta} = -\frac{d^2\theta^{(0)}}{d\zeta^2}, \quad (4.11)$$

where the condition $\theta_g^{(1)} = \theta_s^{(1)} = \theta^{(1)}$ is still valid since $N \rightarrow \infty$.

The boundary conditions for the first correction are $\theta^{(1)} \rightarrow 0$ in $\zeta \rightarrow -\infty$ and $\theta^{(1)} \rightarrow 0$ in $\zeta \rightarrow +\infty$. Integrating Eq. (4.11) with Eq. (4.10) the solution for the first correction gives

$$\theta^{(1)} = \begin{cases} -[\varepsilon/(1 - \varepsilon)]^2 (\zeta - \zeta_f) \exp\{[\varepsilon/(1 - \varepsilon)] (\zeta - \zeta_f)\}, & \text{for } \zeta \leq \zeta_f, \\ 0, & \text{for } \zeta \geq \zeta_f. \end{cases} \quad (4.12)$$

4.3.2 Inner zone: problem of the order of Γ^{-1}

In this thin region gas and solid phases do not have enough contact time to reach thermal equilibrium. Superadiabatic temperatures are expected to arise, but are limited by the intense interphase heat transfer.

In this zone, the variation of the nondimensional variables is of the order of unity along a characteristic length of the order of Γ^{-1} around the flame, except for the solid-phase temperature that presents just a small variation of the order of Γ^{-1} . The variables in this thin zone are denoted by $y_F^{(*)}$, $y_O^{(*)}$, $\theta_s^{(*)}$ and $\theta_g^{(*)}$.

The expansion for the variables can be written as

$$\left. \begin{aligned} y_F^{(*)} &= y_F^{(*) (0)} + \Gamma^{-1} y_F^{(*) (1)} + o(\Gamma^{-1}) \\ y_O^{(*)} &= y_O^{(*) (0)} + \Gamma^{-1} y_O^{(*) (1)} + o(\Gamma^{-1}) \\ \theta_s^{(*)} &= 1 - \Gamma^{-1} \theta_s^{(*) (1)} + o(\Gamma^{-1}) \\ \theta_g^{(*)} &= \theta_g^{(*) (0)} + \Gamma^{-1} \theta_g^{(*) (1)} + o(\Gamma^{-1}) \end{aligned} \right\}. \quad (4.13)$$

Note that the solid-phase temperature has been approximated to the unity at the leading order. To justify this choice, the limit $N \rightarrow \infty$ is taken in Eq. (3.20), resulting in $\theta_s^{(*)} \sim 1$ at the flame. This means that the present model is valid for flames in which the solid-phase at the flame presents a small deviation from the adiabatic limit. With this assumption, the two phases are decoupled at the leading order for this length-scale, as will be seen next.

By rescaling the spatial coordinate as $\Gamma(\zeta - \zeta_f) = \xi$, defining $N \equiv N_0 \Gamma$ with N_0 being a parameter of the order of unity, substituting the asymptotic expansions (4.13) into the conservation equations (3.1) to (3.4) and collecting the higher order terms, the governing equations become

$$\varepsilon \frac{dy_F^{(*) (0)}}{d\xi} = \frac{\varepsilon}{Le_F} \frac{d^2 y_F^{(*) (0)}}{d\xi^2}, \quad (4.14)$$

$$\varepsilon \frac{dy_O^{(*)}(0)}{d\xi} = \frac{\varepsilon}{Le_O} \frac{d^2 y_O^{(*)}(0)}{d\xi^2}, \quad (4.15)$$

$$\varepsilon \frac{d\theta_g^{(*)}(0)}{d\xi} = \varepsilon \frac{d^2 \theta_g^{(*)}(0)}{d\xi^2} + N_0(1 - \theta_g^{(*)}(0)), \quad (4.16)$$

$$0 = (1 - \varepsilon) \frac{d^2 \theta_s^{(*)}(1)}{d\xi^2} - N_0(1 - \theta_g^{(*)}(0)). \quad (4.17)$$

The boundary conditions are determined when the solution corresponding to the problem of the order of unity ($\zeta - \zeta_f = O(1)$) is matched with the problem of the order of Γ^{-1} . Thus, in the unburned region, i.e., upstream from the flame, for $\xi \rightarrow -\infty$, $d\theta_g^{(*)}/d\xi$ and $d\theta_s^{(*)}/d\xi$ are equal to $\Gamma^{-1}d\theta^{(0)}/d\zeta$ evaluated at ζ_f . Then, in first approximation, $d\theta_g^{(*)}(0)/d\xi \sim \Gamma^{-1}\varepsilon/(1 - \varepsilon) \sim 0$ and $d\theta_s^{(*)}(1)/d\xi \sim -\varepsilon/(1 - \varepsilon)$. Analogously, $y_F^{(*)} = y_O^{(*)} \rightarrow 1$ as $\xi \rightarrow -\infty$. In the burned region, i.e., downstream from the flame, for $\xi \rightarrow \infty$, $\theta_g^{(*)} = \theta_s^{(*)} \rightarrow 1$, $y_F^{(*)} = 0$ and $y_O^{(*)} = 1 - \phi$. At the flame, the gas- and solid-phase temperatures, $\theta_{gf}^{(*)}$ and $\theta_{sf}^{(*)}$, are unknowns to be determined.

The solution of Eqs. (4.14) and (4.15) are

$$y_F^{(*)}(0) = \begin{cases} 1 - e^{Le_F(\xi - \xi_f)}, & \text{for } \xi \leq \xi_f, \\ 0, & \text{for } \xi \geq \xi_f, \end{cases} \quad (4.18)$$

$$y_O^{(*)}(0) = \begin{cases} 1 - \phi e^{Le_O(\xi - \xi_f)}, & \text{for } \xi \leq \xi_f, \\ 1 - \phi, & \text{for } \xi \geq \xi_f. \end{cases} \quad (4.19)$$

Equation (4.16) can be written as

$$\frac{d^2 \bar{\theta}}{d\xi^2} - \frac{d\bar{\theta}}{d\xi} - \frac{N_0}{\varepsilon} \bar{\theta} = 0, \quad (4.20)$$

where $\bar{\theta} = (\theta_g^{(*)}(0) - 1)$.

Equation (4.20) is independent of the solid-phase temperature and can be integrated. The solution of (4.20) is $\bar{\theta} = C_1 e^{r_1 \xi} + C_2 e^{-r_2 \xi}$. Applying the proper boundary conditions one finds

$$\theta_g^{(*) (0)} = \begin{cases} 1 + \left(\theta_{gf}^{(*) (0)} - 1 \right) e^{r_1 (\xi - \xi_f)}, & \text{for } \xi \leq \xi_f, \\ 1 + \left(\theta_{gf}^{(*) (0)} - 1 \right) e^{-r_2 (\xi - \xi_f)}, & \text{for } \xi \geq \xi_f, \end{cases} \quad (4.21)$$

in which $\theta_{gf}^{(*) (0)}$ is the gas-phase temperature at the flame, yet to be determined, and

$$r_1 = \frac{1}{2} \left[\left(1 + 4 \frac{N_0}{\varepsilon} \right)^{1/2} + 1 \right],$$

and

$$r_2 = \frac{1}{2} \left[\left(1 + 4 \frac{N_0}{\varepsilon} \right)^{1/2} - 1 \right].$$

With the knowledge of the leading order term of the gas solution, $\theta_g^{(*) (0)}$, equation (4.17) can be integrated giving

$$\theta_s^{(*) (1)} = \begin{cases} \theta_{sf}^{(*) (1)} \left[1 + (r_2/r_1)^2 (e^{r_1 (\xi - \xi_f)} - 1) \right] \\ \quad - (\varepsilon/(1 - \varepsilon)) (\xi - \xi_f), & \text{for } \xi \leq \xi_f, \\ \theta_{sf}^{(*) (1)} e^{-r_2 (\xi - \xi_f)}, & \text{for } \xi \geq \xi_f, \end{cases} \quad (4.22)$$

in which the the first correction for the solid-phase temperature at the flame, $\theta_{sf}^{(*) (1)}$, is given by

$$\theta_{sf}^{(*) (1)} = \frac{N_0 \left(\theta_{gf}^{(*) (1)} - 1 \right)}{r_2^2 (1 - \varepsilon)} \quad (4.23)$$

and is found by applying $\xi = \xi_f$ in Eq. (4.22).

Now, applying the continuity of the heat flux in the solid-phase at the flame, $\partial \theta_s^{(*) (1)} \partial \xi |_{\xi_f^-} = \partial \theta_s^{(*) (1)} \partial \xi |_{\xi_f^+}$, one finds

$$\theta_{gf}^{(*) (0)} = 1 + \theta_{sup}, \quad (4.24)$$

$$\theta_{sup} = (1 + N_\varepsilon)^{-1/2}, \quad (4.25)$$

$$N_\varepsilon = 4N_0/\varepsilon, \quad (4.26)$$

$$\theta_{sf}^{(*) (1)} = \left(\frac{\varepsilon}{1 - \varepsilon} \right) \frac{\theta_{sup}(1 + \theta_{sup})}{(1 - \theta_{sup})}. \quad (4.27)$$

Equation (4.24) is the first approximation for the gas-phase temperature at the flame, where θ_{sup} , Eq. (4.25), is the excess temperature at the flame, i.e., the temperature above the adiabatic limit, which is similar to the heat recirculation efficiency defined in Eq. (3.25). It is possible to verify that θ_{sup} depends only on the parameter N_ε . Then, the superadiabatic effect is more pronounced for lower values of N_0 , i.e., less heat transfer between the phases, and higher values of ε . Equations (4.24) to (4.26) show that, in a first approximation, the flame temperature does not depend on the solid conductivity. This happens because the solid temperature at the length scale l_G is unity in a first approximation. Therefore, under the conditions considered in this analysis, ($N \sim \Gamma \gg 1$), the interphase heat transfer is the limiting process that defines the flame properties.

As in the previous model, the parameter N_ε universalizes the results at the flame in the leading order term, since Eq. (4.24) maintains an explicit dependence only on N_ε and $\theta_{sf}^{(*) (0)} = 1$. Then, the parameter N_ε , called porous media flame number, is the parameter that defines the leading order problem. As in the previous chapter, an analogy between the parameter N_ε and the number of transfer units can be made

$$N_\varepsilon = 4NTU_G \quad \text{and} \quad NTU_G = \frac{h_v l_G}{\varepsilon \rho_n s_F c_p}. \quad (4.28)$$

Note that, in the present model, the NUT is based on the gas-phase length-scale l_G (NUT_G) and that N_ε is directly proportional to NTU_G . The dependence on l_G is expected since, in the present model, this is the length-scale where the interphase

heat transfer is important. The inversion of the dependence of N_ε with NTU - note that in the previous chapter they were inversely proportional - is a result of the intense interphase heat transfer of the present model, a condition that limits the superadiabatic effect, as will be seen in the results.

Now, collecting the terms of the order of Γ^{-1} for the gas-phase one finds

$$\varepsilon \frac{d\theta_g^{(*)}(1)}{d\xi} = \varepsilon \frac{d^2\theta_g^{(*)}(1)}{d\xi^2} - N_0(\theta_s^{(*)}(1) + \theta_g^{(*)}(1)), \quad (4.29)$$

where the boundary conditions are $d\theta_g^{(*)}(1)/d\xi = \varepsilon/(1-\varepsilon)$ for $\xi \rightarrow -\infty$ and $\theta_g^{(*)}(1) = 0$ for $\xi \rightarrow \xi_f$. Then, the first correction of gas-phase temperature, for $\xi \leq \xi_f$, can be determined as

$$\theta_g^{(*)}(1) = \left\{ \theta_{sf}^{(*)}(1) \left[\left(\frac{r_2}{r_1} \right)^2 - 1 \right] + \frac{N_0}{1-\varepsilon} \right\} (1 - e^{r_1(\xi-\xi_f)}) + \left(\frac{\varepsilon}{1-\varepsilon} \right) (\xi - \xi_f). \quad (4.30)$$

4.3.3 Inner zone: reaction region $O(\delta\Gamma^{-1})$

In a region of the order of $\delta\Gamma^{-1}$ around the flame, the variables present a variation of the order of δ . The solution follows the same steps already discussed in the previous solution for higher equivalence ratios (section 3.3.4). The flame velocity is given by Eq. (3.58), in which the approximation of Eq. (3.59) is still valid. The value of m , the downstream nondimensional gas-phase conduction heat flux, can be determined from the gas temperature profile given by Eqs. (4.13), (4.21), (4.24) and (4.30) resulting in

$$m = \frac{r_2}{r_1 + r_2} = (1 - \theta_{sup})/2. \quad (4.31)$$

Note that, since for $m \rightarrow 1/2$ there is extinction, as was discussed in the preceding chapter, the flame temperature needs to be above the adiabatic free-flame temperature for the flame propagation to be possible, i.e., $\theta_{sup} > 0$.

4.3.4 Model summary

A closed form approximated solution for the structure and propagation velocity of ultra-lean adiabatic stationary premixed flames in porous inert media is obtained. The temperature profile of both phases for the region of thermal equilibrium is given by Eqs. (4.5), (4.8), (4.10) and (4.12). In the region of thermal nonequilibrium, the temperature profile of the gas-phase is described by Eqs. (4.13), (4.21), (4.24) and (4.30) and the temperature profile of the solid-phase is described by Eqs. (4.13), (4.22) and (4.23). The fuel and oxidant mass fraction profiles are given by Eqs. (4.18) and (4.19). The flame velocity is evaluated by Eq. (3.58), in which Eqs. (3.59) and (4.31) are used.

This set of equations is able to qualitatively predict, under the limitations imposed by the kinetic mechanism of one global step, the main characteristics of flames in porous media for heat transfer parameters N of the order of Γ . Another condition imposed in this solution is $\varepsilon/(1 - \varepsilon) \sim O(1)$, which ensures the separation of the length-scales of the problem. The model is also restricted to the conditions where the solid-phase temperature at the flame presents small deviations from the adiabatic limit. In the next section the model will be explored to evaluate the influence of the problem parameters on such flames.

4.4 Discussion

The reaction rate parameters were adjusted to yield a reasonable agreement with measured laminar flame speeds for free flames with equivalence ratios ranging from

0.5 to 0.6. The heat of reaction was adjusted to reproduce the adiabatic flame temperature for $\phi = 0.5$ [93]. The gas-phase properties were approximated by the air properties evaluated at 1000 K. The volumetric heat transfer coefficient h_v is modeled following Fu et al. [21], which uses a volumetric Nusselt number, $Nu_v = C' Re^{m'}$, where $Nu_v = h_v d_m^2 / \lambda_g$ and Re is the Reynolds number, $Re = \rho_n u_n d_m / \mu_n$. The mean pore diameter is modeled as $d_m = \left(\sqrt{4\varepsilon/\pi} \right) / (39.37\varphi)$, which is a uniform pore distribution model, where φ is the linear pore density given in pores per inch (ppi). Note that, contrary to the previous model, the variations of h_v are expressive for extremely lean mixtures and the present analysis must take it into account. The used transport and geometric properties of the solid-phase are typical of porous burners [2, 26]. Table 4.1 shows the parameters and properties used in the calculations and some of the results obtained.

4.4.1 Influence of the equivalence ratio

Figure 4.2 shows the flame velocity s_F as a function of ϕ . The upper branch of the curve corresponds to the physical solution and the lower branch corresponds to a non-physical solution ($N \ll \Gamma$). Below $\phi = 0.217$ the parameter m reaches the limiting value 0.5 and the steady state flame propagation is not possible. Then, the present model indicates that there is a flammability limit for the premixed methane-air combustion within porous media. For the porous medium under analysis this limit is found around $\phi = 0.217$. All the subsequent analysis will be restricted to the physical branch of the solution.

Figure 4.3 shows the parameter $N_0 = N/\Gamma$ as a function of ϕ . The model is constructed for $N_0 \sim O(1)$, then, we see that the solution is valid for a small range

Table 4.1: Properties and parameters used in the calculations and results for $\phi = 0.225$, $\Gamma = 60$, $\varepsilon = 0.8$, $\varphi = 50$ *ppi* and $Le_F = 1$.

Properties and Parameters			Results		
R_u	8.314	$\text{J}(\text{mol K})^{-1}$	λ_s	4.041	$\text{W}(\text{m K})^{-1}$
E_a	1.2×10^5	J mol^{-1}	h_v	1.476×10^4	$\text{W}(\text{m}^3 \text{K})^{-1}$
A	1.0×10^{10}	$\text{m}^3(\text{kg s})^{-1}$	T_r	838	K
a	0		T_{gf}	1052.1	K
Q	4.759×10^7	J kg^{-1}	T_{sf}	805.0	K
c_p	1141	$\text{J}(\text{kg K})^{-1}$	s_F	2.252	cm s^{-1}
λ_g	0.06735	$\text{W}(\text{m K})^{-1}$	N_0	1.072	
ρ_n	1.185	kg m^{-3}	α	0.64	
T_n	298	K	β	11.1	
C'	0.146		Da_f	42.74	
m'	0.83		\overline{Da}_f	0.3706	
ε	0.8		m	0.3017	
ϕ	0.225		n	0.9926	
φ	50	<i>ppi</i>	δ	0.1421	
Γ	60		N	64.31	
Le_F	1		θ_{gf}	1.397	

of equivalence ratios around $\phi = 0.225$. Since N_0 is proportional to $1/s_F^2$, for leaner mixtures the corresponding lower flame velocities result in higher values of N_0 and for higher equivalence ratios the higher flame velocities result in lower values of N_0 .

Figure 4.4 shows the gas and solid-phase temperatures at the flame as a function of ϕ . Contrary to the previous model, for the condition $N \sim O(1)$, the non-dimensional flame temperature, $\theta_{gf}^{(*)}$, increases as ϕ is increased. This is a consequence of Eq. (4.24), in which $\theta_{gf}^{(*)0}$ varies with $N_0^{-1/2}$. Physically, the reason for this behavior is the intense heat transfer from the gas-phase to the solid phase that occurs at the gas-phase length-scale for leaner mixtures. Lower values of ϕ result in lower flame velocities, thus, there is more time for the interphase heat transfer and the gas-phase

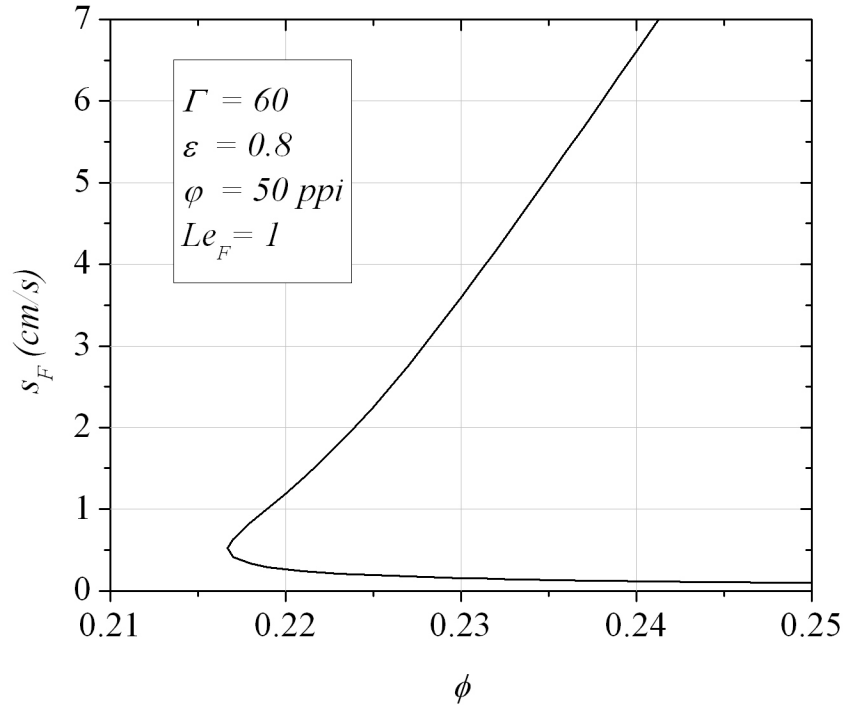


Figure 4.2: The flame velocity s_F as function of ϕ . The upper branch corresponds to the physical solution.

temperature is limited by the intense heat loss to the solid matrix. As ϕ is further decreased there is a point in which the temperatures at the flame are not high enough to sustain the flame and a flammability limit is found. As the superadiabatic flame temperature decreases, i.e., as θ_{sup} decreases, the heat flux to the downstream side of the flame becomes more important and the parameter m tends to the limiting value of 0.5, according to Eq.(4.31). Then, one can conclude that, to sustain flames at ϕ smaller than the free-flame flammability limit it is necessary to reach a minimum superadiabatic flame temperature, i.e., $\theta_{sup} > 0$, as discussed in relation to Eq. 4.31. For the conditions considered in Fig. 4.4, the temperature at the flame must be at

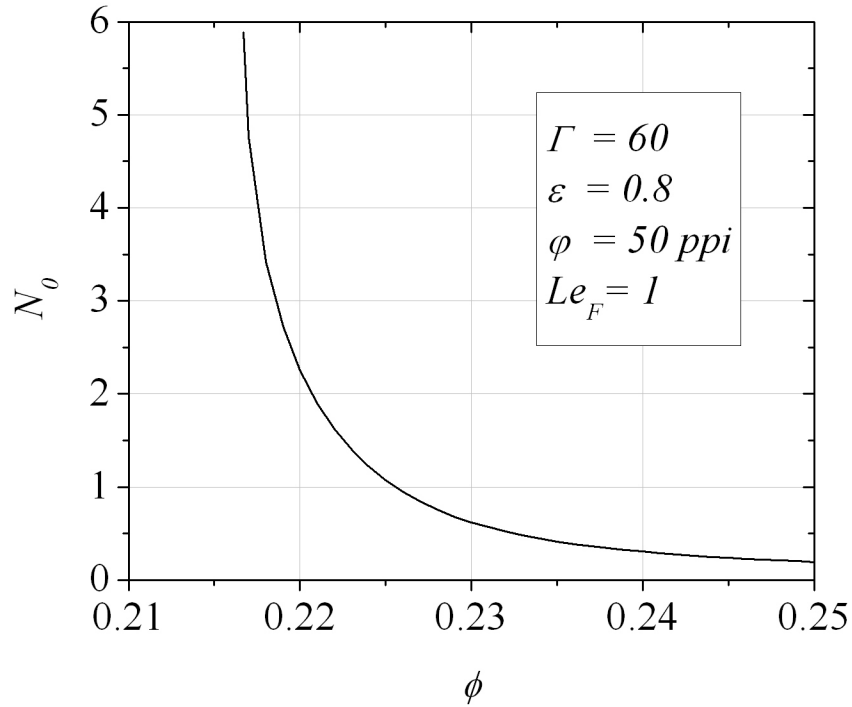


Figure 4.3: The parameter N_0 as a function of ϕ .

least 20% above the adiabatic free-flame temperature.

It is important to recall that, although the present model is based on the one-step reaction mechanism, this approximation is adequate for this first theoretical approach since it permits the adjustment of a few chemical parameters to agree with experiments. Despite this and other simplifying assumptions, the results reveal the strong dependence of the flammability limit for premixed methane-air combustion in porous inert media on the gas phase temperature at the flame and the matrix properties. To improve this prediction, at least a four-step reaction mechanism should be considered and experiments should be carried out to correctly determine the volumetric interphase heat transfer coefficient h_v at the flow rates and temperatures of interest.

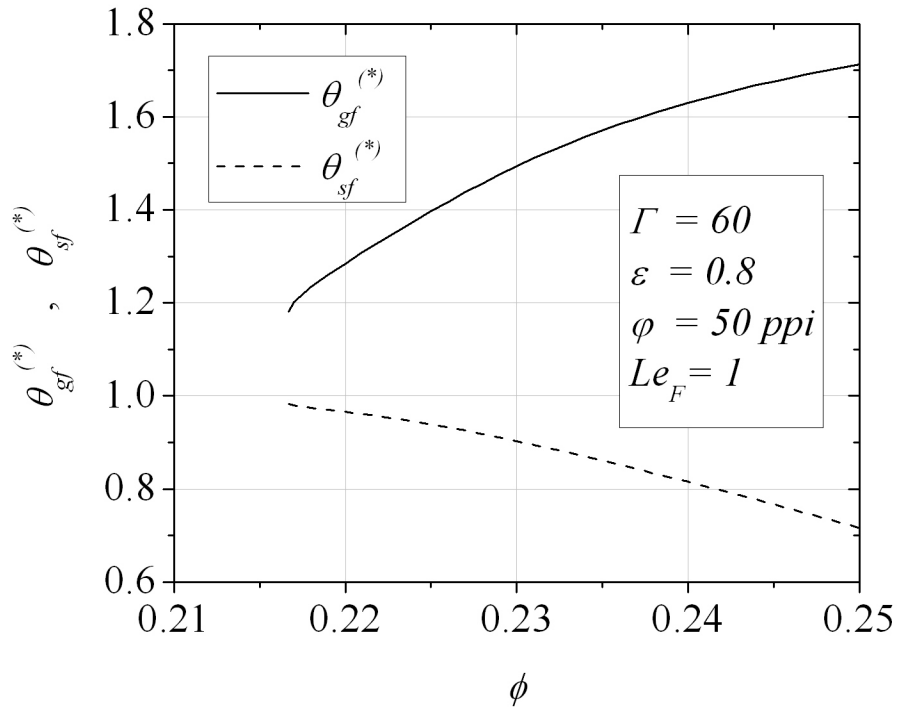


Figure 4.4: Gas and solid-phase temperatures at the flame as a function of ϕ .

Additionally, since in the flammability limit the value of N_0 is much higher than one, the precise determination of this limit requires a model considering the condition $N \gg \Gamma$.

It is worth to recall that, for moderately lean mixtures the nondimensional superadiabatic flame temperature increases when ϕ is decreased, whereas for the ultra-lean mixtures the superadiabatic flame temperature decreases when ϕ is decreased. Then, we expect to find a point of maximum nondimensional superadiabatic flame temperature in the lean side of the equivalence ratio range. This can be understood by considering two limiting cases. For $N \rightarrow 0$ the two equations for the conservation

of energy are decoupled and the flame structure has the same structure of a free-flame. The solid-phase plays no role in the solution and superadiabatic temperatures are not possible. For $N \rightarrow \infty$ the two phases are in local thermal equilibrium and the problem reduces to a one-equation model, i.e., a free-flame like structure for a homogeneous medium with effective properties and again superadiabatic flame temperatures are not possible. For intermediate values of N thermal non-equilibrium between the phases and superadiabatic flame temperatures are found and a point of maximum nondimensional superadiabatic flame temperature must exist.

An interesting characteristic of the model is that Eqs. (4.24) and (4.27) do not depend on Γ , i.e., in a first approximation the solid thermal conductivity λ_s does not influence the gas- and solid-phases temperatures at the flame. This is due to the fact that the heat conduction is not the limiting process responsible for the gas-phase preheating ($\theta_{sf}^{(*) (0)} = 1$). Then, the interphase heat transfer and the convective-diffusive balance in the gas phase are the controlling process that define the properties at the flame. Nevertheless, the solid-phase conductivity impacts the extension of the total flame thickness, l_S . For ultra lean mixtures, the solid-phase diffusion length-scale is very large. For example, the total length of the flame (pre-heating and reaction regions) reaches 20 cm for $\phi = 0.225$. This occurs because the low flame velocities of these extremely lean mixtures allow a wide thermal penetration.

According to Eq. (4.13), the solid-phase temperature at the flame is found by $\theta_{sf}^{(*)} = 1 - \Gamma^{-1} \theta_{sf}^{(*) (1)}$. According to Eq. (4.23), $\theta_{sf}^{(*) (1)}$ varies with $N_0^{-1/2}$, and since N_0 increases as ϕ decreases, the solid-phase temperature at the flame $\theta_{sf}^{(*)}$ is expected to increase for lower values of ϕ . This is a consequence of the intense interphase heat transfer found in extremely lean mixtures. As N_0 increases, the solid- and gas-phase

temperatures at the flame becomes closer, approaching the adiabatic limit.

4.4.2 Influence of the matrix properties

Figure 4.5 shows the dependence of N_0 , $\theta_{gf}^{(*)}$, $\theta_{sf}^{(*)}$ and s_F on ε . The effect of decreasing ε , for a constant φ , is to decrease the mean pore diameter d_m , thus resulting in a large heat transfer coefficient h_v and, consequently, in a large value of N_0 . Again, the effect of increasing N_0 is to decrease the superadiabatic effect. According to Eq. (4.24), the gas-phase temperature at the flame varies as $\varepsilon^{1/2}$. The flame velocity follows the gas-phase temperature at the flame and increases with increasing values of ε . As N_0 increases the solid-phase temperature at the flame approaches the limiting value of unity.

When the linear density of pores φ is increased while maintaining a constant porosity ε the mean pore diameter decreases. This leads to a solid matrix with a large specific superficial area (m^2/m^3) increasing the interphase heat transfer coefficient h_v and the parameter N_0 . The behavior of the flame variables when increasing φ is shown in Fig.4.6 and is similar to that of decreasing the porosity, i.e., for higher values of N_0 the superadiabatic effect decreases.

It is interesting to note that decreasing φ the condition of $N_0 \sim O(1)$ is obtained for decreasing values of ϕ , i.e., the decrease in h_v caused by the larger pores has to be balanced by the lower flame velocities obtained for leaner mixtures. This, in turn, leads to decreasing values for the lean flammability limit as shown in Fig.4.7. This result shows that, for premixed combustion within porous inert media, the lean flammability limit is no longer a property of the reactants mixtures only, but it is also dependent on the solid matrix properties. Additionally, at the lean flammability

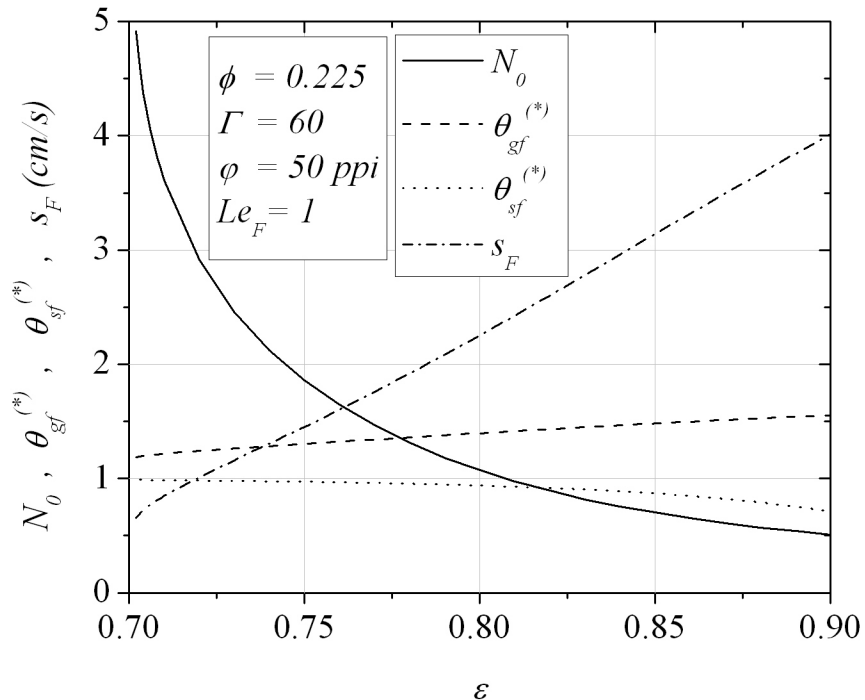


Figure 4.5: Dependence of N_0 , $\theta_{gf}^{(*)}$, $\theta_{sf}^{(*)}$ and s_F on ε .

limit, the reaction length-scale l_R is of the order of the pore diameter l_d , showing that, in this limit, the interphase heat transfer tends to be important even at the innermost length-scale.

4.4.3 Influence of the Lewis number

Figure 4.8 shows the effect of fuel Lewis number Le_F on the flame variables. Since, according to Eq. (3.58), lower flame velocities s_F are found for lower values of Le_F , the interphase heat transfer is intensified due to the longer contact time between the phases and, consequently, the superadiabatic effect decreases.

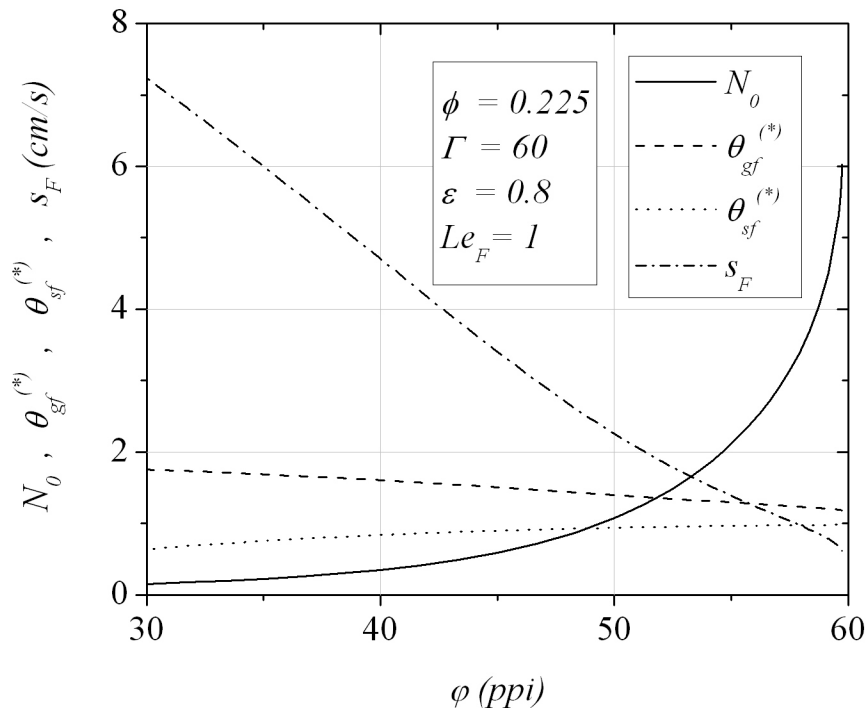


Figure 4.6: Dependence of N_0 , $\theta_{gf}^{(*)}$, $\theta_{sf}^{(*)}$ and s_F on φ .

4.4.4 Flame structure

Figure 4.9 shows the flame structure for $\phi = 0.225$, $\Gamma = 60$, $\varepsilon = 0.8$, $\varphi = 50$ ppi and $Le_F = 1$. The profile of the solid temperature at the gas scale presents a displacement in relation to the solution at the solid scale. This happens because in the solution of the problem at the gas-phase diffusion length-scale only the continuity of the energy flux through the solid-phase is required as a matching condition. There is no matching condition that requires the continuity of the temperature. Then, the results are consistent even with this gap in the solid solution. This kind of gap between the inner and outer solutions is present in other asymptotic solutions [99].

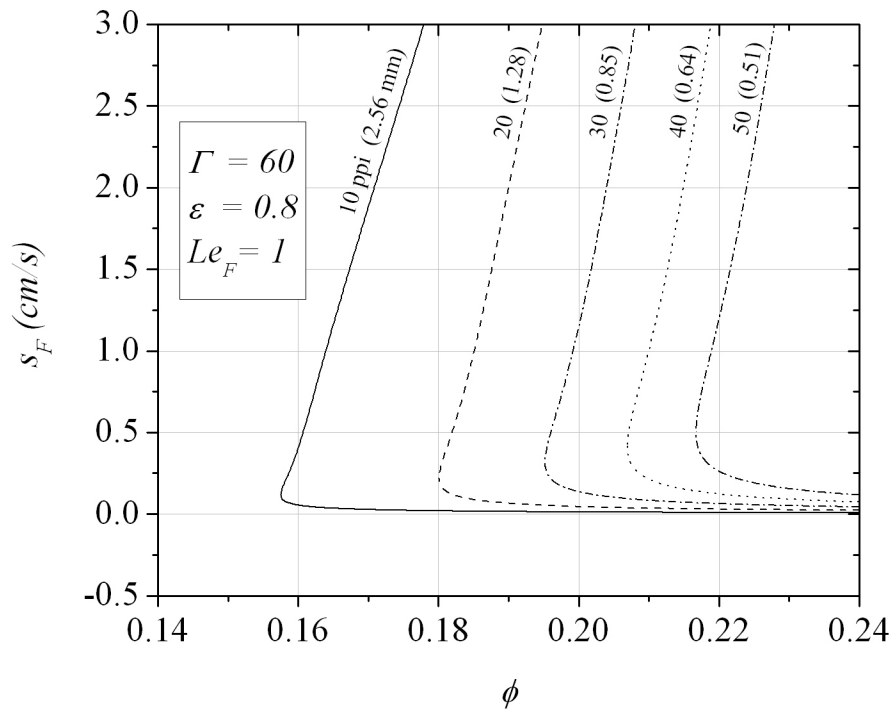


Figure 4.7: The flame velocity s_F as function of ϕ for different values of φ . The numbers in parenthesis are the corresponding mean pore diameters.

The present solution shows that, even though we are dealing with a problem that presents local thermal equilibrium in a wide region around the flame, the choice to model the problem with the one-equation model for the conservation of energy would neglect the existence of superadiabatic flame temperatures in a thin region around the flame. These superadiabatic flame temperatures decrease as the interphase heat transfer is increased, however, there should exist a small region of thermal nonequilibrium around the flame where superadiabatic flame temperatures will be found, in order for the flame to be sustained. This result cannot be obtained with the models that assume local thermal equilibrium between the phases over the entire domain of solution.

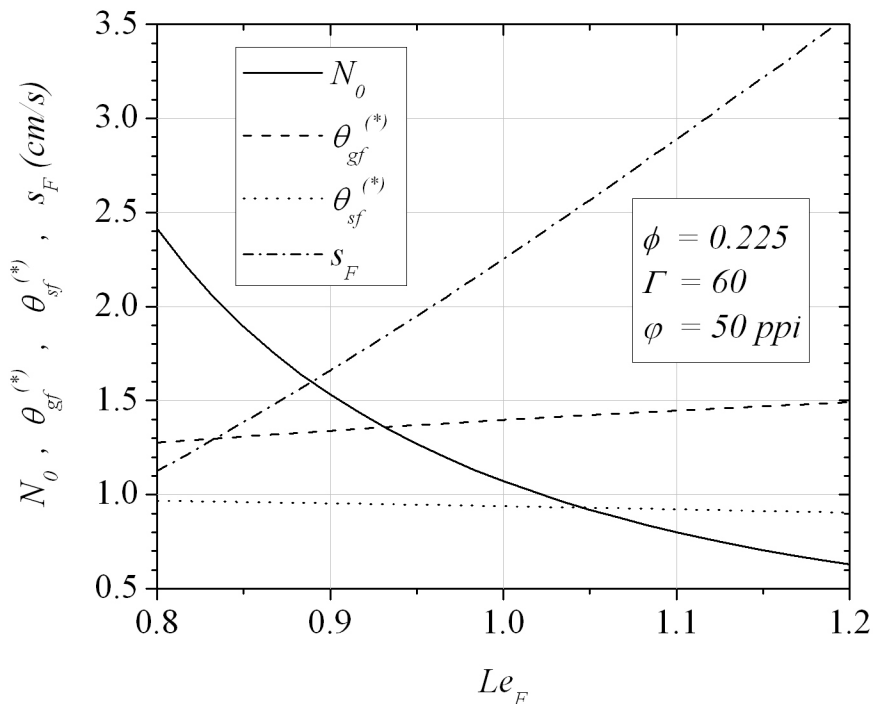


Figure 4.8: Dependence of N_0 , $\theta_{gf}^{(*)}$, $\theta_{sf}^{(*)}$ and s_F on Le_F .

4.5 Conclusions

An analysis of adiabatic stationary planar premixed flames within inert porous media is proposed for the conditions of $N \sim O(\Gamma)$ and $\varepsilon/(1 - \varepsilon) \sim O(1)$. The condition $N \sim O(\Gamma)$ is characterized by an intense interphase heat transfer and is found for extremely lean mixtures. These flames present a wide region of local thermal equilibrium between the phases and the superadiabatic effect is limited by the intense interphase heat transfer at the gas-phase diffusion length-scale.

The superadiabatic effect is less pronounced for lower values of ε and higher values of φ . This behavior is related to the increase in the interphase heat transfer coefficient

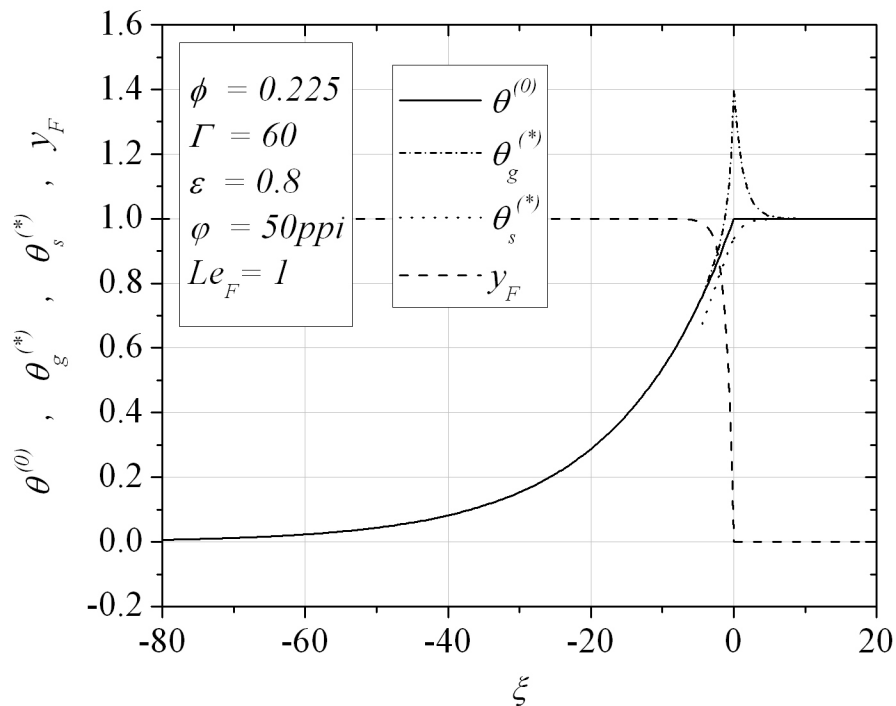


Figure 4.9: Flame structure for $\phi = 0.225$, $\Gamma = 60$, $\varepsilon = 0.8$, $\varphi = 50$ ppi and $Le_F = 1$.

h_v . The superadiabatic effect is also less pronounced for lower values of Le_F , a behavior which is connected to the lower flame velocities observed for decreasing values of Le_F .

The analysis shows that the superadiabatic flame temperature decreases as ϕ is decreased, i.e., as the interphase heat transfer becomes more intense. Since in a previous model, valid for higher equivalence ratios, the superadiabatic flame temperature increases when ϕ is decreased, a maximum nondimensional superadiabatic flame temperature in the lean side of the equivalence ratio range is expected to exist.

For extremely lean mixtures the gas-phase temperature at the flame must reach a minimum superadiabatic flame temperature for the flame propagation to be possible.

Thus, the model shows the existence of a flammability limit for ultra-lean mixtures. For methane-air flames, considering $Le_F = 1$, and with $\Gamma = 60$, $\varepsilon = 0.8$ and $\varphi = 50$ ppi, the present analysis predicts the lean flammability limit to occur around $\phi = 0.217$ with a gas-phase temperature at the flame 20% above the adiabatic limit. A better determination of this limit would require the use of, at least, a four-steps kinetic mechanism and the solution of the problem of $N_0 \gg 1$. These results cannot be obtained with the models that assume local thermal equilibrium between the phases over the entire domain of solution because these models do not allow superadiabatic flame temperatures to arise.

Chapter 6

A Level-set model for the numerical simulation of porous burners

In this chapter, the level-set method for flame simulations is presented and then employed in conjunction with the flame speed expression obtained in the previous chapters to build a model for three-dimensional numerical simulations. A 1D version of the model is employed to solve two test problems and the model limitations are discussed.

6.1 Introduction

The level-set method is an interesting tool for the predicting the main thermal aspects of the combustion in porous media and could be used as basis for building an efficient, low computational cost, design tool for porous burners with complex three-dimensional shapes. The model can be based on the G -equation for the flame movement in combination with the analytical expression for the flame velocity obtained in the previous chapters. The main idea is to use a macroscopic volume-averaged

model to describe the problem of heat transfer between the gas and solid phases at the large scale l_S (macroscale model) and a premixed flame model for the local flame consumption speed (microscale model) as a form of multiscale treatment for reaction in porous media [58].

Van Oijen and de Goey [56] developed a flamelet-generated-manifold method (FGM) where a higher dimensional flame is considered as an ensemble of one-dimensional flames. This model is divided in three parts: the first part describes the fluid motion and mixing process, the second part describes the front motion through a kinematic G -equation (level-set) and the third part consists of a set of 1D flamelet equations, using a local coordinate adapted to the flame sheet, governing the inner flame structure and local mass burning rate. The flamelet equations are solved by treating the system as an 1D adiabatic premixed flame. These solutions form a manifold that can be used in subsequent simulations. To test this method, they simulated a ceramic-foam surface burner in a radiating furnace and compared the results with temperature measurements at the gas-phase above the burner [57]. The small differences between computed and measured temperatures were found to lie within the experimental errors. It is worth mentioning that, in this application, the flame is stabilized above the burner surface.

Nevertheless, their method is not directly applicable to volumetric burners, i.e., porous burners in which the flame is stabilized within the solid matrix. In this case, the 1D set of flamelet equations must include the solid-phase energy equation and the reaction region cannot be considered as an adiabatic region. As seen in the previous chapters, the downstream gas-phase heat conduction [related to the parameter m in Eq. (3.58)] has a central role in determining the flame velocity and is a direct result

of the interaction between the gas-phase and the solid matrix. Additionally, since the solid-phase length-scale, l_S , is large, the flame is influenced by the heat losses far upstream or far downstream from the flame, which brings new difficulties in building a FGM version for volumetric burners.

In the next section, the level-set method applied to premixed combustion problems is reviewed. Then, a simplified model for three-dimensional simulations of porous burners is proposed and a microscale model for the premixed flame velocity in porous inert media is formulated based on the results of the previous chapters. Finally, results of the present level-set model are presented and compared to a conventional model, i.e., one that solves the full set of volume-averaged conservation equations, including global chemical kinetics, for the entire domain. The model limitations are evaluated and the multidimensional implementation is discussed.

6.2 Level-set method

The level-set method is based on a transport equation for a non-reacting scalar, G , that describes the propagation of the flame front. The flame thickness is assumed to be small and the problem is reduced to a thin reactive sheet separating unburnt and burnt gases. The flame is located at $G = G_0$ and the flame front displacement depends on the local balance between the flow velocity and the flame propagation velocity (consumption speed). The dynamics of this reactive sheet is described by the G -equation [60].

Consider a scalar field of a non-reacting scalar G . An isoplane of G is defined as the surface where $G(t, \mathbf{x}) = \text{constant}$. The kinematic equation that describes the

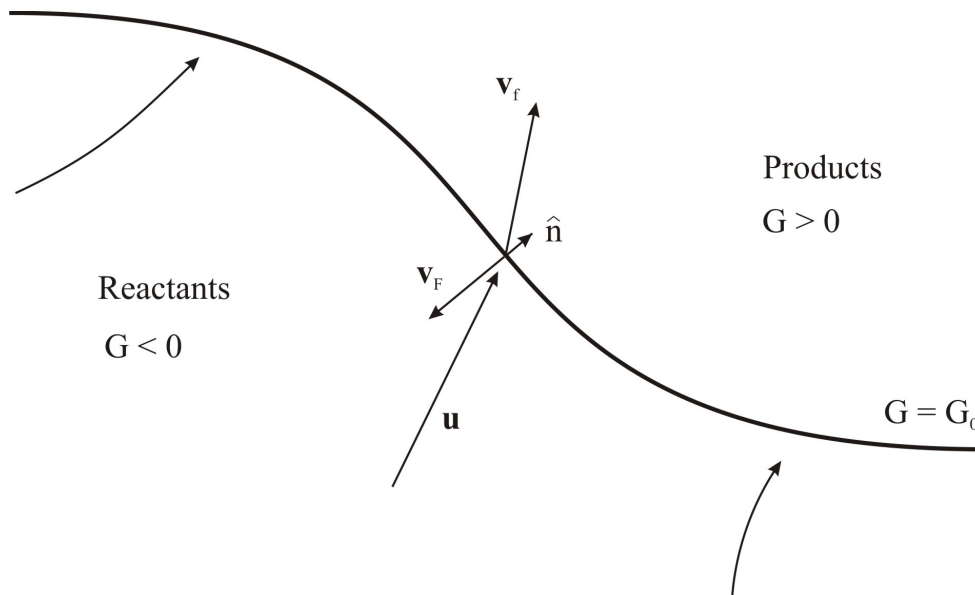


Figure 6.1: Velocity balance at the flame surface.

motion of such an iso-surface is given by

$$\frac{DG}{Dt} \equiv \frac{\partial G}{\partial t} + \mathbf{v}_f \cdot \nabla G = 0, \quad (6.1)$$

where \mathbf{v}_f is the iso-surface absolute velocity vector, with respect to the laboratory frame. The left hand side of Eq. (6.1) is the material derivative of the scalar field G . A point on a given iso-surface will remain at this surface for all t . The normal vector on an iso-surface is defined as

$$\hat{\mathbf{n}} = \frac{\nabla G}{|\nabla G|}, \quad (6.2)$$

pointing to the burnt side of the flame.

Figure 6.1 shows a schematic representation of the velocity vectors of interest. The isoplane velocity \mathbf{v}_f is the result of a balance between the local flow field velocity \mathbf{u} and the local flame displacement velocity v_F , with respect to the flow velocity, as

$$\mathbf{v}_f = \mathbf{u} - v_F \hat{\mathbf{n}}. \quad (6.3)$$

Note that the tangential component of the flow velocity and of the isoplane velocity are equal ($u_t = v_{f,t}$). Then, the amount of mass effectively consumed by the flame is $\rho(\mathbf{u} - \mathbf{v}_f) \cdot \hat{\mathbf{n}}$.

Now, substituting Eqs.(6.2) and (6.3) into (6.1) we find the G -equation

$$\frac{\partial G}{\partial t} + \mathbf{u} \cdot \nabla G = v_F |\nabla G|. \quad (6.4)$$

This scalar equation describes the surface displacement as the result of a balance between the flow advection and the front propagation.

The G -equation has meaning at the flame front only, where the propagation velocity v_F is defined. Outside this surface, the form of the G -function can be arbitrarily defined and the results are not to be affected by this choice. Then, a convenient definition for the G -function is

$$|\nabla G| = 1, \quad (6.5)$$

thus G is a signed distance function in relation to the flame surface, i.e., the value of G at each point in the solution domain is equal to the distance from this point to the closest point along the flame surface. Then, the flame front is the zeroth level of the G -function. Note that the solution of the G -field is independent of the form of the G -function outside $G = G_0$ because there are no diffusion terms in Eq. (6.4).

A problem that arises in the solution of Eq. (6.4) is that the G -function may become distorted and large or small gradients around the flame surface may be created. To overcome this difficulty it is usual to periodically replace the resulting G -field with $|\nabla G| = 1$, maintaining the same zero level set. This is usually called reinitialization step. Some authors proposed ways of accurately performing this task [101, 102].

Another problem in solving Eq. (6.4) is the formation of cusps when the flame velocity is assumed to be constant. Level-set models with flame velocity expressions

that account for the effects of flame curvature and flame strain are presented in the literature [54, 103]

The coupling between the G -equation and the energy equation is a key-point in the level-set modeling. Three approaches have been proposed in the literature: 1) a flame-front tracking, which through geometric considerations identifies the front displacement and calculates the volume of reagents consumed by the flame [104, 105], 2) a temperature reconstruction technique, where the temperature field is directly reconstructed from the G -field, independent of any energy balance equation [54, 106], and 3) an estimate of the heat release based on the G -field to determine the source term to be included in the energy equation [106].

In the next section, a simplified model to multidimensional simulations of premixed flames in porous inert media based on the level-set method is presented.

6.3 Mathematical formulation

6.3.1 Macroscopic-level model

With the use of the G -equation for the flame movement and a proper model for the flame velocity (microscopic-level model), a simplified model for the simulation of premixed flames in porous media can be constructed. The flame velocity model is obtained from the results of the preceding chapters and will be summarized in the next section.

In the macroscopic-level problem, the reaction region is assumed to be a thin surface separating fresh and burned gases. Then, the species conservation equations do not need to be solved and the heat release term in the gas-phase energy equation

is substituted by a local source term to be modeled. A steady-state two-medium model is now written for the conservation of total mass, momentum, gas-phase and solid-phase energy as

$$\varepsilon \frac{\partial \rho_g \mathbf{u}}{\partial t} + \varepsilon \nabla \cdot \rho_g \mathbf{u} = 0, \quad (6.6)$$

$$\begin{aligned} \frac{\rho_g}{\varepsilon} \left(\frac{\partial \mathbf{u}}{\partial t} + \mathbf{u} \cdot \nabla \mathbf{u} \right) = -\nabla p + \rho_g \mathbf{f} \\ + \frac{\mu}{\varepsilon} \nabla^2 \mathbf{u} - \frac{\mu}{\mathbf{K}} \mathbf{u} - \frac{C_E}{\mathbf{K}^{1/2}} \rho_g |\mathbf{u}| \mathbf{u}, \end{aligned} \quad (6.7)$$

$$\varepsilon (\rho c_p)_g \frac{\partial T_g}{\partial t} + \varepsilon (\rho c_p)_g \mathbf{u} \cdot \nabla T_g = \nabla \cdot \varepsilon \lambda_g \nabla T_g + \dot{s}_r + h_v (T_s - T_g), \quad (6.8)$$

$$(1 - \varepsilon) (\rho c_p)_s \frac{\partial T_s}{\partial t} = \nabla \cdot (1 - \varepsilon) \lambda_s \nabla T_s - h_v (T_s - T_g), \quad (6.9)$$

In Eq. (6.8), the term \dot{s}_r is the heat source due to the homogeneous reactions. It can be modeled as a concentrated heat source at the flame surface or can be distributed around the flame based on the G -field. A one-dimensional example of a distribution implementation is presented in the Section 6.3.4. The flame movement is modeled by the G -equation presented in the previous section, Eq. (6.4).

6.3.2 Microscopic-level model

In the previous chapters, asymptotic solutions were proposed for stationary adiabatic premixed flames in porous inert media taking advantage of the large difference between the thermal conductivity of the solid and gas phases. For completeness, the main length-scales identified in the previous analysis are presented below and

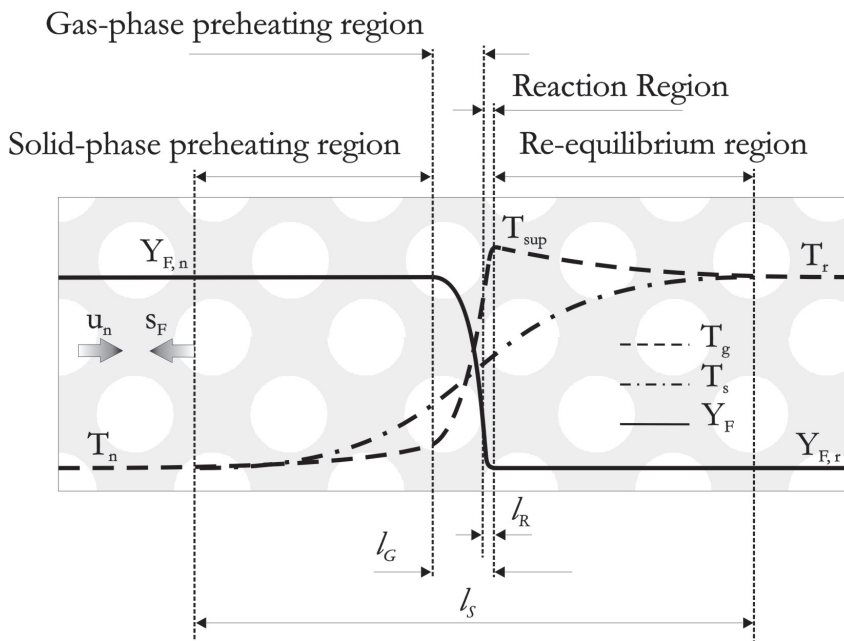


Figure 6.2: Schematic representation of the temperatures and fuel mass fraction distributions for the different characteristic length-scales of the problem.

sketched in figure 6.2,

$$\frac{l_G}{l_S} = \frac{\varepsilon}{(1 - \varepsilon)\Gamma} \quad \text{and} \quad \frac{l_R}{l_G} \equiv \delta,$$

with $l_G \equiv \varepsilon \lambda_g / (\varepsilon \rho_n S_F c_p)$.

The extent of the thermally affected region, l_S , is determined by a balance among the conduction through the solid-phase, the interphase heat transfer and the advection transport in the gas-phase. As shown in Chapter 4, this region tends to the local thermal equilibrium when the mixture is extremely lean, in which case the gas-phase thermal diffusion is also important. The reactions are restricted to a region l_R that is a fraction of the gas-phase length-scale, l_G .

A first-order estimate for the flame speed for premixed flames in porous inert media was derived in Chapter 3, Eq. (3.58). In Chapter 4 it is shown that the same

expression for the flame velocity is valid even for extremely lean mixtures.

The model in Chapter 3 was not valid for $\phi \rightarrow 1$ due to the reaction expression dependance on the oxidant mass fraction. Here it is used a fuel decomposition model of the form

$$w_r = A\rho Y_F T_g^a e^{-E_a/R_u T_g}. \quad (6.10)$$

Then, the new flame speed expression obtained is

$$s_F^2 = \frac{2A \rho_f \lambda_g T_{gf}^a L e_F \delta^2 \exp(-\beta/\alpha)}{(\rho_n^2 c_p)} \exp \left\{ \frac{\beta \eta_{rec}}{1 + \alpha \eta_{rec}} + m n \right\}. \quad (6.11)$$

The nondimensional reaction region thickness, δ , the heat recirculation efficiency, η_{rec} , and the term $m n$ are given by

$$\delta = \frac{[1 + \alpha \eta_{rec}]^2}{\beta}, \quad (6.12)$$

$$\eta_{rec} \equiv \frac{\varepsilon \rho_n s_F c_p (T_{gf} - T_r)}{\varepsilon \rho_n s_F Y_{F,n} Q} = \frac{(T_{gf} - T_r)}{(T_r - T_n)}, \quad (6.13)$$

$$m n = 1.344m - 4m^2(1 - m)/(1 - 2m) + 3m^3 - \ln(1 - 4m^2), \quad \text{for } -0.2 < m < 0.5, \quad (6.14)$$

As shown in Chapter 3, Eq. (6.14) is an approximation to the numerical solution of the 1D energy and species conservation equations at the reaction region for a premixed free-flame obtained by Liñán [87], n is a displacement on the coordinate axis imposed to match asymptotically the solution in the reaction length-scale to that in the gas-phase diffusion length-scale and m is the ratio of the thermal energy conducted downstream from the flame (normal to the flame surface) to the total energy release.

For adiabatic combustion, approximate expressions for m are available in the previous chapters. An estimate for intermediate to stoichiometric values of the equivalence ratio can be obtained from Eq. (5.15) as

$$m = \frac{\eta_{rec}}{2} \frac{N_e}{\Gamma_e} \left[(1 + 4/N_e)^{1/2} - 1 \right], \quad (6.15)$$

where Γ_e is the effective thermal conductivities ratio [$\Gamma_e = (1 - \varepsilon) \lambda_s / \varepsilon \lambda_g$] and N_e is the effective heat transfer parameter (NTU based on l_S and s_F) given by

$$N_e = \frac{(1 - \varepsilon) \lambda_s h_v}{(\varepsilon \rho_n s_F c_p)^2}. \quad (6.16)$$

For ultra-lean mixtures, an approximation for m is given by Eq. (4.31). This expression can be written as a function of η_{rec} as

$$m = 1 - \eta_{rec}/2, \quad (6.17)$$

Note that η_{rec} is related to the macroscopic solution via T_{gf} .

An alternative choice is to calculate m directly from the macroscopic field of T_g as

$$m = \frac{(-\varepsilon \lambda_g \nabla T_g)_{f+}}{\varepsilon \dot{m}_g'' c_p (T_r - T_n)}, \quad (6.18)$$

where the term $(-\varepsilon \lambda_g \nabla T_g)_{f+}$ is the downstream gas-phase conduction heat flux normal to the flame surface and \dot{m}_g'' is the local mass flux of reactants per unit area. The advantage of this option is that Eq. (6.18) is valid even for non-adiabatic conditions.

As was noted in Chapter 3, in combustion within porous-media, the value of m is bounded by $0 \leq m \leq 0.5$, with the limit $m = 0$ corresponding to a freely propagating flame and the limit $m = 0.5$ corresponding to flame extinction. Then, the parameter m can be used as an indication of how close a flame is from extinction. Note also that the flame velocity expression given by Eq. (6.11) is dependent on the flame surface

through the flame temperature T_{gf} , then, curvature effects are already incorporated in the model, in a first approximation.

The separation of the length-scales of the problem, $l_R \ll l_S$, permits the use of Eqs. (6.11) to (6.18) as a subgrid model to compute the flame velocity of premixed flames within porous inert media. The subgrid model relates the flame speed (microscale model) to the flame temperature that is a result of the energy balance between the phases (macroscale model).

6.3.3 Model validation

To validate the proposed model, a one-dimensional steady-state problem is analyzed. The level-set model proposed here and the conventional model are presented below.

Level-set model.

The steady-state 1D version of the macroscopic Eqs. (6.6) to (6.9) is written as

$$\varepsilon \rho u = \varepsilon \rho_n s_F, \quad (6.19)$$

$$\varepsilon \rho_n s_F c_p \frac{dT_g}{dx} = \varepsilon \lambda_g \frac{d^2 T_g}{dx^2} + \dot{s}_r + h_v (T_s - T_g), \quad (6.20)$$

$$0 = (1 - \varepsilon) \lambda_s \frac{d^2 T_s}{dx^2} - h_v (T_s - T_g), \quad (6.21)$$

where ρ and c_p are gas-phase properties.

The heat source is modeled as

$$\dot{s}_r = \begin{cases} \varepsilon \rho_n u_n Y_{F,n} Q / l_R, & \text{for } x = x_f, \\ 0, & \text{for } x \neq x_f, \end{cases} \quad (6.22)$$

where $\rho_n u_n$ is the mass flow of the reactants, $Y_{F,n}$ is the initial mass fraction of the fuel and Q is the heat of reaction based on the mass of fuel. Equation (6.22) indicates that the energy is released at the flame sheet, $x = x_f$, only. In fact, it is distributed in a length-scale that is thinner than the mesh size, as will be shown in the next section.

The 1D version of Eq.(6.4) is

$$\frac{\partial G}{\partial t} + u \frac{\partial G}{\partial x} = v_F \left| \frac{\partial G}{\partial x} \right|, \quad (6.23)$$

with u being the x component of the velocity vector \mathbf{u} . Since Eq.(6.23) is valid at the flame position only, the flow velocity and the flame velocity are defined at that location as $v_F = s_F(\rho_n/\rho_f)$ and $u = u_n(\rho_n/\rho_f)$. Additionally, with the $|\nabla G| = 1$ condition, Eq. (6.23) reduces to

$$\frac{\partial G}{\partial t} = (s_F - u_n) \frac{\rho_n}{\rho_f}. \quad (6.24)$$

Note that the temporal derivative of the level-set equation is maintained in this formulation since the G -Equation will be used to move the flame from its initial position to its final stabilized position in a transient (distorted) calculation. Then, at steady state, Eq. (6.10) is reduced to $s_F = u_n$.

No formal derivation of the volume-averaged level-set equation is presented here. Then, the G -Equation is viewed heuristically as

$$\frac{\partial \langle G \rangle^g}{\partial t} = (\langle s \rangle_F^g - \langle u \rangle_n^g) \frac{\langle \rho \rangle_n^g}{\langle \rho \rangle_f^g}. \quad (6.25)$$

Conventional model.

The results of the level-set approach are compared to a model, here named conventional, based on the simultaneous solution of total mass, species and thermal energy equations with a one-step kinetic mechanism,

$$\varepsilon \rho u = \varepsilon \rho_n s_F, \quad (6.26)$$

$$\varepsilon\rho_n s_F \frac{dY_F}{dx} = \varepsilon\rho D_F \frac{d^2Y_F}{dx^2} - \varepsilon A\rho Y_F T_g^a e^{-E_a/R_u T_g}, \quad (6.27)$$

$$\varepsilon\rho_n s_F c_p \frac{dT_g}{dx} = \varepsilon\lambda_g \frac{d^2T_g}{dx^2} + \varepsilon Q A\rho Y_F T_g^a e^{-E_a/R_u T_g} + h_v(T_s - T_g), \quad (6.28)$$

$$0 = (1 - \varepsilon)\lambda_s \frac{d^2T_s}{dx^2} - h_v(T_s - T_g), \quad (6.29)$$

Two test problems will be considered with different boundary conditions:

Test problem 1: Adiabatic combustion in an infinite medium.

In this case, the boundary conditions for the fuel mass fraction and for the gas- and solid-phase temperatures are Dirichlet conditions at the inlet ($T_g = T_s = T_n$ and $Y_F = Y_{F,n}$) and Neumann conditions at the outlet ($\partial/\partial x = 0$). The G -equation is not necessary since the flame position is imposed. The problem is aimed at the evaluation of the effect of a concentrated heat source on the flame velocity prediction. Note that for the conventional model, the flame velocity (eigenvalue) is obtained from the integration of the fuel mass conservation equation.

Test problem 2: Flame stabilization in a porous radiant burner.

In the second case, the porous medium is finite ($L = 10$ mm) and radiant heat losses are allowed at both ends. Then, the boundary conditions at the inlet ($x = 0$) are

$$-(1 - \varepsilon)\lambda_s \left. \frac{dT_s}{dx} \right|_{x=0} = -\sigma_{SB}\epsilon(T_{s,0}^4 - T_\infty^4), \quad (6.30)$$

$$-\varepsilon\lambda_g \left. \frac{dT_g}{dx} \right|_{x=0} = -\varepsilon\rho_n u_n c_p (T_{g,0} - T_\infty), \quad (6.31)$$

and the boundary conditions at the outlet ($x = L$) are

$$-(1 - \varepsilon)\lambda_s \left. \frac{dT_s}{dx} \right|_{x=L} = \sigma_{SB}\epsilon(T_{s,L}^4 - T_\infty^4), \quad (6.32)$$

$$-\varepsilon\lambda_g \left. \frac{dT_g}{dx} \right|_{x=L} = 0. \quad (6.33)$$

where σ_{SB} is the Stefan-Boltzmann constant, ϵ is the solid-phase total hemispherical emissivity, $T_{s,0}$ and $T_{s,L}$ are respectively the solid-phase temperature at the inlet and outlet, $T_{g,0}$ is the inlet gas-phase temperature and T_∞ is the ambient temperature. In this problem, the inlet velocity is imposed and the flame is allowed to find its stabilization position.

When solving the fuel conservation equation in the conventional model, the boundary conditions are Dirichlet conditions at the inlet and Neumann conditions at the outlet.

6.3.4 Numerical method

The conservation equations are discretized in a standard finite volume form as discussed by Patankar [94]. The power-law scheme is used for the approximation of the total flux (convection and diffusion). A uniform mesh is used for the calculations, except for the conventional model in the test problem 1, where a refined grid at the flame is employed. Steps are taken to accelerate convergence to steady-state.

In the present implementation, a distribution scheme of the heat release based on geometrical considerations is used. The heat source is distributed in the characteristic reaction length-scale ($l_R = \delta l_G$) that is thinner than the computational mesh size. Then, the heat release is effectively modeled as a concentrated source. Nevertheless,

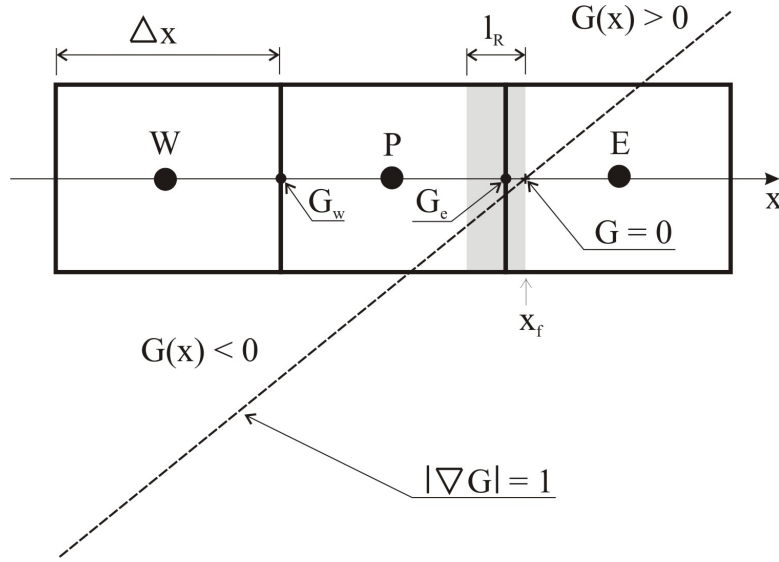


Figure 6.3: Source term distribution in the computational mesh.

this distribution allows a smooth transition of the flame front between two adjacent cells. Figure 6.3 shows a schematic representation of the computational grid, with the shadowed area representing the region where the heat release is to be distributed. This is done comparing the value of G in the cell interfaces with the reaction length-scale l_R

$$\dot{s}_{r,i} = \begin{cases} 0, & \text{for } G_e < -l_R \text{ or } G_w > 0, \\ \dot{s}_r (l_R + G_w + \Delta x), & \text{for } G_w < -l_R < G_e, \\ \dot{s}_r (-G_w), & \text{for } G_w < 0 < G_e, \\ \dot{s}_r, & \text{for } G_w < -l_R \text{ and } G_e > 0. \end{cases} \quad (6.34)$$

where, $\dot{s}_{r,i}$ is the heat release term of the i^{th} cell, $\dot{s}_r = \varepsilon \rho_n u_n Y_{F,n} Q / l_R$ is the total heat release ($\dot{s}_r = \sum \dot{s}_{r,i}$), G_w and G_e are the values of the G -field at the left and right cell interfaces respectively ($G(x) = x - x_f$) and Δx is the mesh size.

The flame velocity, s_F , is calculated based on Eqs. (6.11) to (6.14), but the heat

recirculation efficiency expression, Eq. (6.13), is modified to

$$\eta_{rec} = C \frac{(T_{gf} - T_r)}{(T_r - T_n)}, \quad (6.35)$$

where C is an adjustable parameter. This parameter is introduced here to correct a small discrepancy between the flame velocity predicted by the conventional model and the one predicted by the level-set model. The parameter m is evaluated directly from the T_g field as

$$m = \frac{-\varepsilon \lambda_g (dT_g/dx)_{f+}}{\varepsilon \rho_n u_n c_p (T_r - T_n)}. \quad (6.36)$$

For the test problem 2, the solution algorithm can be summarized as:

1. The flame is initiated at an arbitrary position x_f with hyperbolic tangents for initial (guessed) gas- and solid-phase temperatures,
2. The G -field is imposed to be a signed distance function in relation to the flame front in a direct form, i.e., $G(x) = x - x_f$
3. The heat source is distributed as described by Eq. (6.34),
4. The conservation equations, Eqs. (6.19) to (6.21), are solved for a limited number of iterations (10 iterations are sufficient),
5. The flame velocity, Eq. (6.11), is calculated based on the flame temperature $T_{g,f}$ obtained from the solution of the conservation equations, with m given by Eq. (6.36) and η_{rec} given by Eq. (6.35),
6. A time step is advanced and the level-set equation, Eq. (6.25), is solved resulting in a new G distribution.
7. The flame position is identified as $x_f = x(G = 0)$,

8. Return to step 2.

This process is repeated until the G -equation solution results in a stationary flame, i.e., when $s_F = u_n$. The solution was considered converged when the relative errors for the global energy balance across the burner were smaller than 1×10^{-6} .

The reaction rate parameters for the one-step model considered were adjusted to give a reasonable agreement with measured laminar flame speeds for methane-air free flames [93] for equivalence ratios ranging from 0.5 to 1.0 (relative errors smaller than 8%). The heat of reaction was adjusted to reproduce the adiabatic flame temperature, which is approximated by a polynomial function [107]. A constant volumetric heat transfer coefficient h_v is estimated following Fu et al. [21]. The gas-phase properties were approximated by the air properties evaluated at 1300 K. Transport and geometric properties of the solid-phase are typical of porous burners [2, 26]. Table 6.1 shows the parameters and properties used in the calculations. For the numerical solution of the conventional model, the flame speed (eigenvalue) was obtained from the overall mass balance.

6.4 Discussion

In the following, the premixed flame within an adiabatic infinite medium is computed, then, the model is employed to study the flame stabilization in a finite medium with radiant heat losses at both ends.

Table 6.1: Properties and parameters used in the calculations.

Parameter	Value	Unit
A	1.0×10^8	s^{-1}
a	0	
c_p	1187	$\text{J}(\text{kg K})^{-1}$
E_a	1.41×10^9	J mol^{-1}
h_v	2.0×10^5	$\text{W}(\text{m}^3 \text{K})^{-1}$
Le_F	1	
R_u	8.314	$\text{J}(\text{mol K})^{-1}$
T_∞	298.15	K
ε	0.8	
λ_g	0.0797	$\text{W}(\text{m K})^{-1}$
λ_s	4.783	$\text{W}(\text{m K})^{-1}$
ρ_n	1.185	kg m^{-3}

6.4.1 Adiabatic combustion in an infinite medium

In this section, the present model is compared to the conventional solution for an infinite adiabatic medium. Figure 6.4 shows the flame speeds predicted by the two models for equivalence ratios ranging from 0.5 to 1. The level-set model presents a good agreement with the conventional model. The relative error of the flame velocity predicted by the present model to that calculated by the conventional one ranges from 0.5% for $\phi = 1$ to 4% for $\phi = 0.5$.

Figure 6.5 shows the comparison of the gas and solid-phase reduced temperatures for the two models for $\phi = 1$. The level-set model is able to reproduce both phases temperature distributions with discrepancies smaller than 3%.

The errors in the temperature distributions are found to increase as ϕ decreases. Figure 6.6 shows the temperature profiles for $\phi = 0.5$ for both models. Indeed, the error in the flame temperature prediction is around 5%, decreasing to less than 3% far

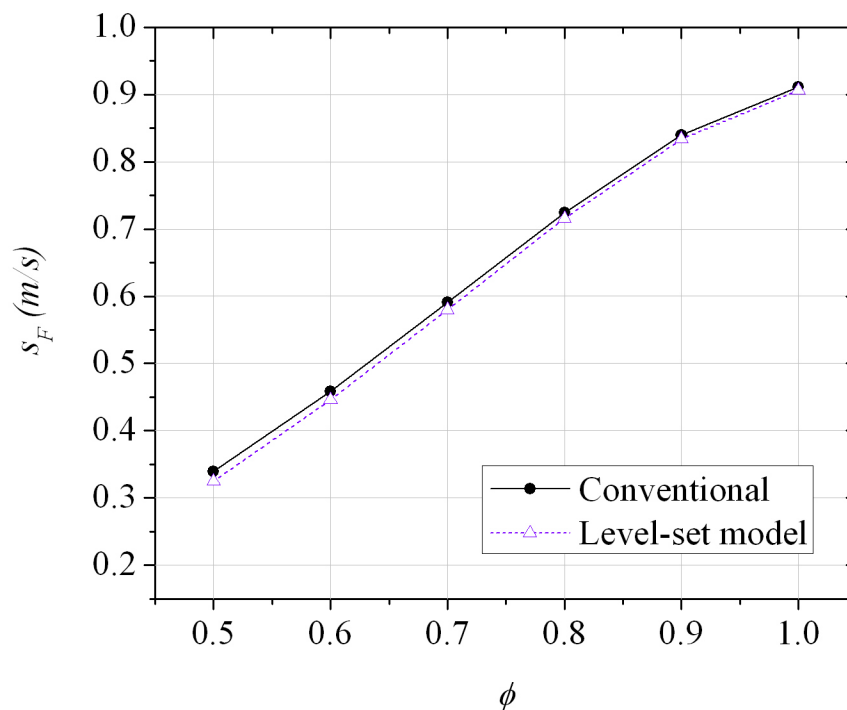


Figure 6.4: Comparison of the predicted flame velocity for the conventional model and the level-set model with concentrated heat release.

from the flame. These increasing discrepancies are due to the fact that the level-set model concentrates the heat release in a thin region around the flame position. In the conventional solution, the heat release is spread over a wider region (of the order of l_G). Since, for leaner mixtures, l_G becomes increasingly wider, the assumption of a concentrated heat release becomes less valid.

The parameter C in Eq. (6.35) can be adjusted to match the level-set results for the flame velocities with that obtained with the conventional model. This adjustment varies from 1 to 5% as can be seen in Fig. 6.7. This small adjustment could be important in determining the flame position in a finite length burner, in particular

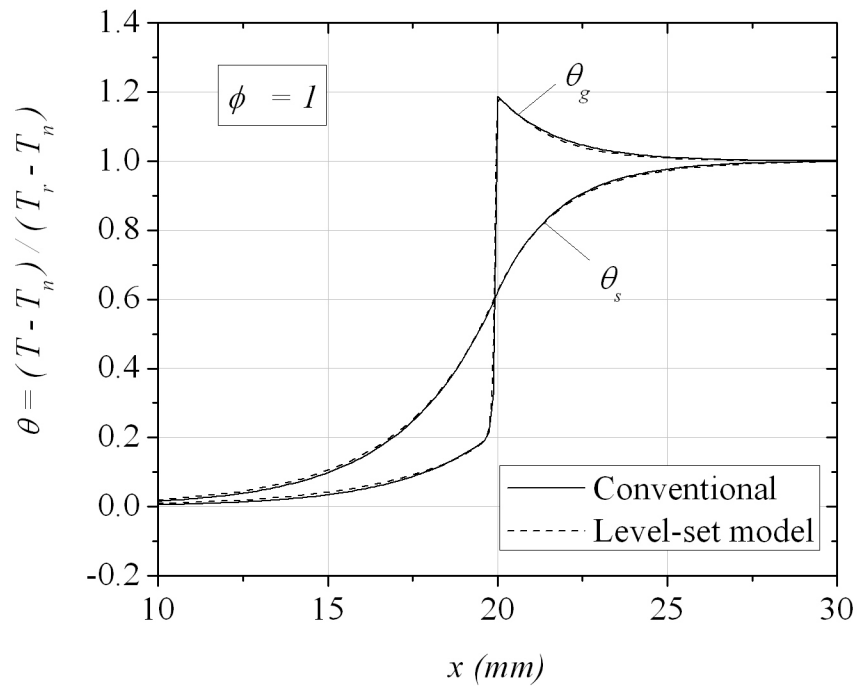


Figure 6.5: Comparison of the gas- and solid-phase temperatures between a conventional model and the level-set model for $\phi = 1$.

for flames near the blow-off limit, as will be shown in the next section.

6.4.2 Flame stabilization in a porous radiant burner

Stability results

In this section the level-set model is used to evaluate the flame stabilization in a porous radiant burner of finite length with radiant heat losses at the inlet and outlet ends. In this case, there is a range of flow rates in which the flame stabilization is

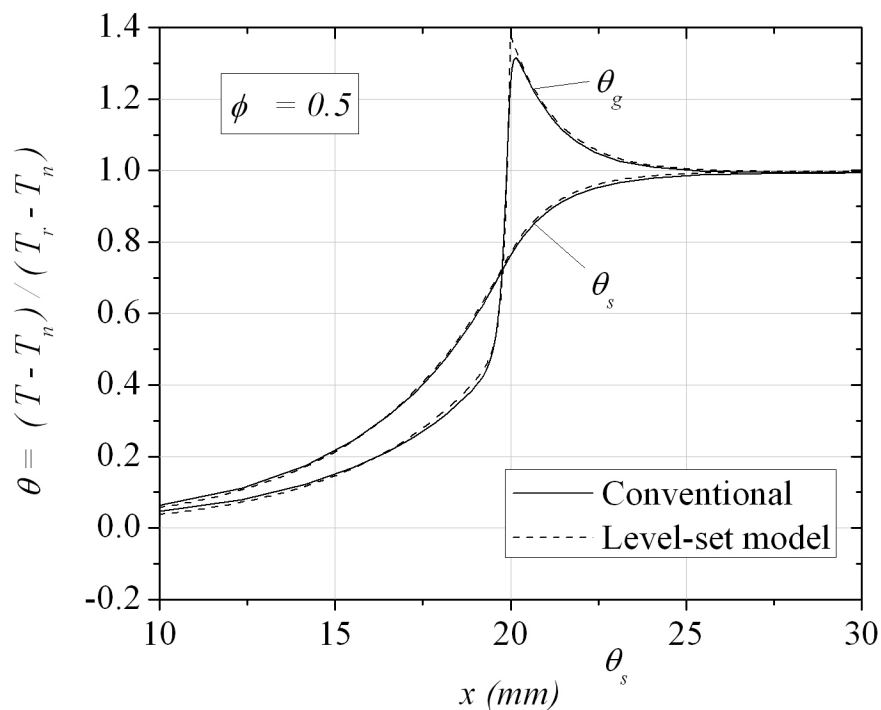


Figure 6.6: Comparison of the gas- and solid-phase temperatures between a conventional model and the level-set model for $\phi = 0.5$.

possible [13]. In the numerical solution, the flame position is not imposed, instead, it is the outcome from the balance between the flow convection and the flame propagation. Stable solutions are found for flames located near the inlet surface of the burner, a condition in which an increase of the flow velocity results in an increase of the flame temperature [48].

Figure 6.8 shows the gas-phase temperature predicted by both models as a function of the inlet flow velocity, u_n , for $\phi = 1$. The flame stabilization range was determined by varying u_n with 0.1 m/s increments until the blow-off or flash-back limits were

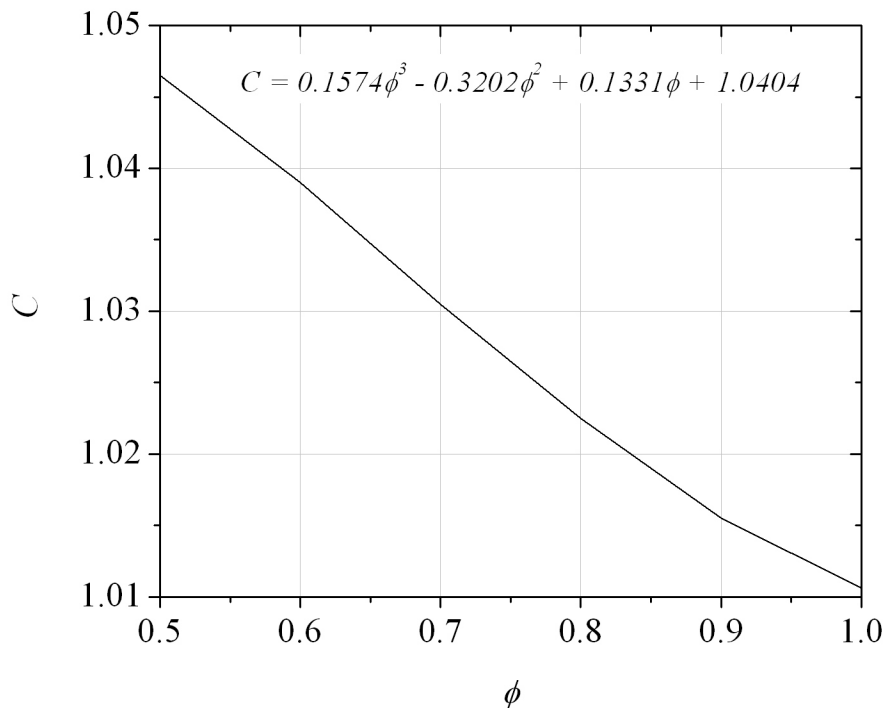


Figure 6.7: Adjustment of the parameter C in Eq. (6.35).

found. The level-set model presents a good agreement with the conventional one. For both models the stabilization is not possible for $u_n > 0.86$ m/s. On the other hand, the level-set model predicts stable flames for inlet flow velocities as low as 0.43 m/s, whereas in the conventional model this limit is found for 0.51 m/s.

Figure 6.9 shows the flame temperature (maximum gas-phase temperature) and inlet velocity, which is equal to the flame velocity, $s_F = u_n$, as a function of the flame position. The blow-off limit is found in the region where flame temperature is nearly constant with increasing inlet velocities, or, in other words, when the derivative of the flame temperature with respect to the flame position tends to zero ($\partial\theta_{g,f}/\partial x_f \rightarrow 0$).

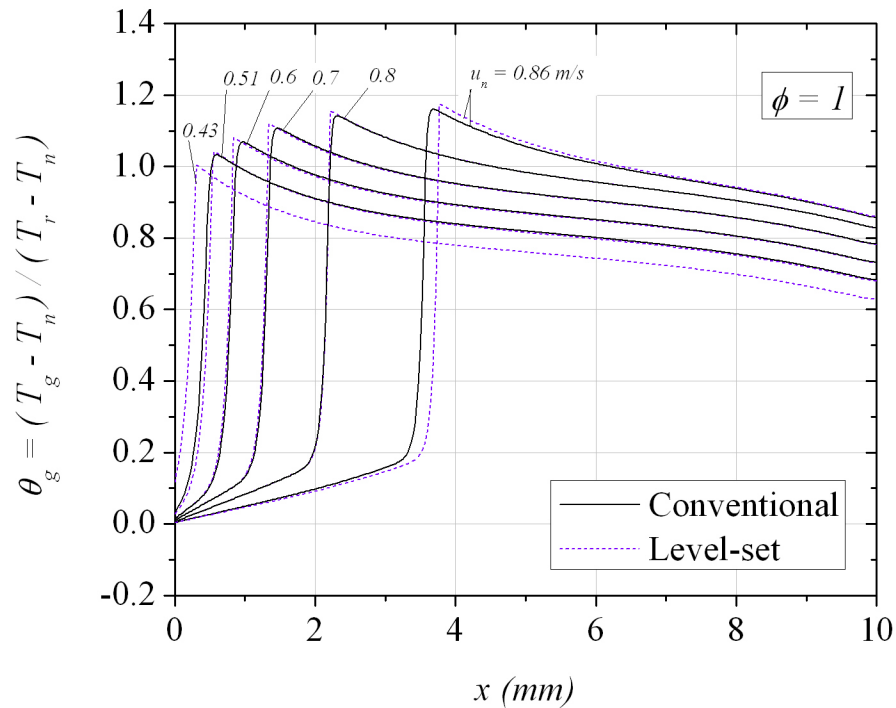


Figure 6.8: Gas-phase temperature distribution as a function of the inlet flow velocity u_n for $\phi = 1$

As shown in [48], a further increase in u_n , beyond the blow-off limit, may lead to a new flame position (near the outlet surface of the burner) where the equilibrium between inlet and flame velocities is found again, however, this position is unstable and will not be considered here. Note that, near the blow-off limit, small differences in the flame velocity prediction may result in completely distinct stabilization conditions, since a small increase in u_n may lead to large flame displacements. This explains the discrepancies observed between the models near the blow-off limit. Then, as a general rule, the flame has a tendency to find its stable position near the inlet surface

of the burner. The relative errors between both models for the flame temperature prediction are smaller than 2%. The errors between both models for the flame position prediction, relative to the total length of the burner, are also smaller than 2%.

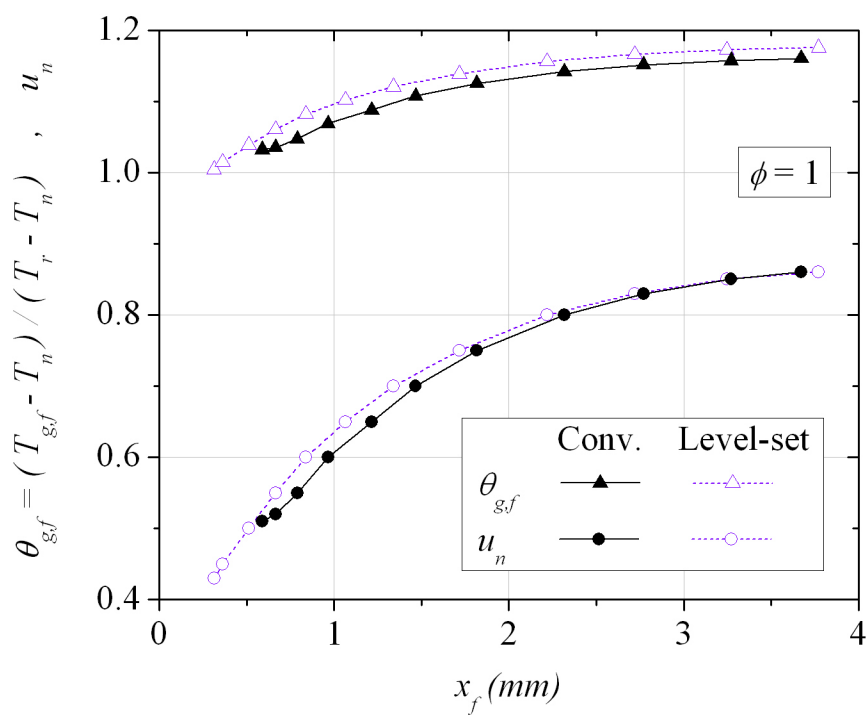


Figure 6.9: Inlet velocity u_n and flame temperature $\theta_{g,f}$ as a function of the flame position x_f .

The flash-back limit is characterized by the situation where a decrease in the inlet velocity leads the flame to propagate upstream from the burner inlet surface. The discrepancies between the models near this limit are due to the differences in the response of the flame temperature (and velocity) to the upstream heat losses. As is shown in Fig. 6.9, the conventional model results are less sensitive to the flame

position and, consequently, to the inlet heat losses near the inlet end of the burner. Then, the flame velocity does not decrease sufficiently to stabilize smaller flow rates and the flash back limit is found.

Figures 6.10 and shows the gas and solid-phase temperatures for u_n equal to 0.51 and 0.86 m/s. The differences in the solid-phase temperature predictions are similar to those in the gas-phase. These differences are smaller near the outlet surface of the burner, what is important since the solid-phase temperature distribution in this region defines the forward radiant output of the burner. This is shown in figure 6.11, which brings the forward and backward radiant losses of the burner, as defined by the boundary conditions, Eqs. (6.30) and (6.32). The discrepancies between the two models for the prediction of the forward radiant output of the burner are smaller than 0.5% (unless near the flashback limit where the errors increase to 3%).

Figures 6.12 and 6.13 show the stability range for $\phi = 0.8$ and $\phi = 0.6$ respectively. It is known from experimental works that the stability range decreases as the equivalence ratio is decreased [1, 13] and this tendency is captured by the numerical solution. The agreement between both models becomes less precise for lower equivalence ratios, although the errors for the flame position prediction are still smaller than 2%. However, for example, for $\phi = 0.6$, the level-set model overestimates the flame temperature and the relative errors between both models reaches 6%. This occurs because, for lower values of ϕ , the reaction region thickness increases and the concentrated heat release condition, imposed in the level-set model, becomes a poor approximation. Additionally, the increase of the reaction region thickness for lower values of ϕ , renders the conventional model more sensitive to the inlet heat losses and, thus, the flash back limit is found for lower inlet flow rates.

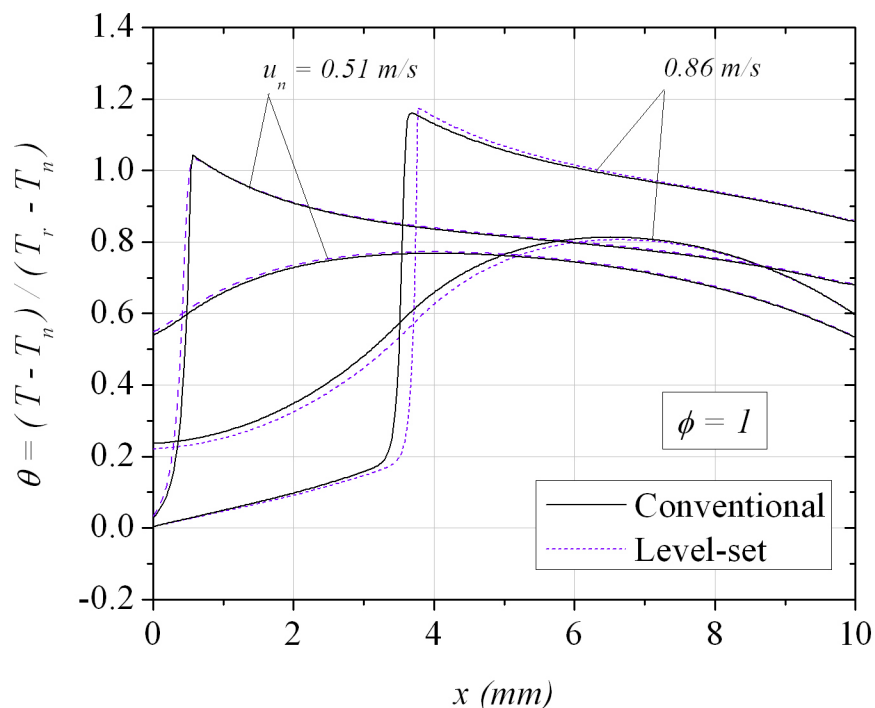


Figure 6.10: Gas and solid-phase temperatures for $u_n = 0.51$ and 0.86 m/s.

CPU time evaluation

The advantages of the present model can be observed in the figures 6.14 to 6.16. In the conventional model, Fig. 6.14, 400 points in the mesh are required to achieve mesh independence (the mesh points evaluated were 50, 100, 200, 400 and 800 points). The criterion used to determine mesh independence was to achieve relative errors smaller than 0.1% for the flame temperature and flame position predictions. For a 100-points mesh no solution can be obtained. The level-set model with a concentrated heat release is much less sensitive to the mesh size and Fig. 6.15 shows that good solutions

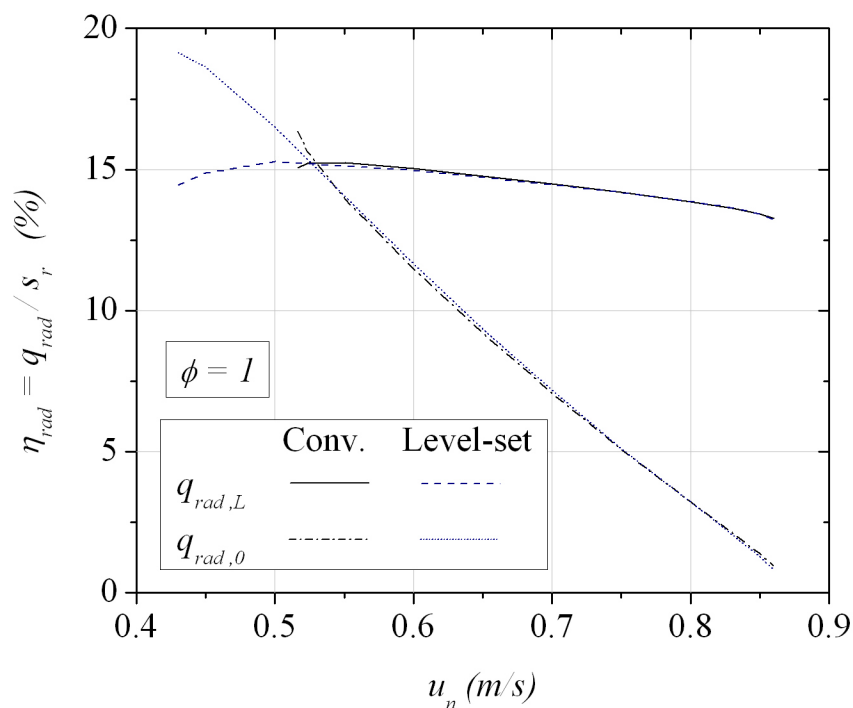


Figure 6.11: Forward ($q_{rad,L}$) and backward ($q_{rad,0}$) radiant losses as a function of the inlet velocity for $\phi = 1$.

can be obtained even with a 100-points mesh.

Finally Fig. 6.16 shows the *CPU time* required to obtain a converged solution in a standard 2.0 GHz processor / 1.0 Gb RAM PC for both models. The computations were initiated with hyperbolic tangents for the guessed temperature and species distributions with the flame placed at 1 mm from the inlet surface. For number of points in the mesh larger than 250, the level-set model is faster than the conventional one. With an 800-points mesh, for example, the level-set model is approximately 40% faster. For a 200-points mesh, the conventional model is faster than the level-set

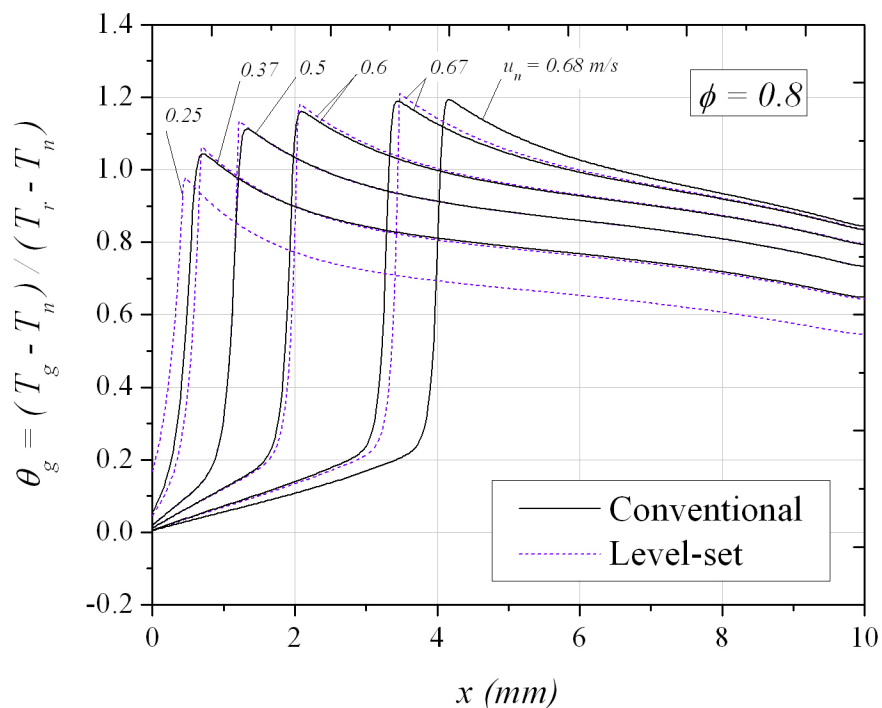


Figure 6.12: Gas-phase temperature distributions as a function of the inlet flow velocity u_n for $\phi = 1$.

model, however, the solution obtained is poor due to the low resolution of the mesh as seen in Fig. 6.14, i.e., the solution is no more mesh independent. For the present problem, to assure mesh independence, the comparison must be made between the level-set model with 100-points mesh and the conventional model with 400-points mesh. The result of this comparison is that the level-set model is about 16 times faster than the conventional model. For some points near the blow-off limit, the level-set model requires a 200-points mesh to achieve mesh independence. In these critical cases, the level-set model is about 6 times faster than the conventional one,

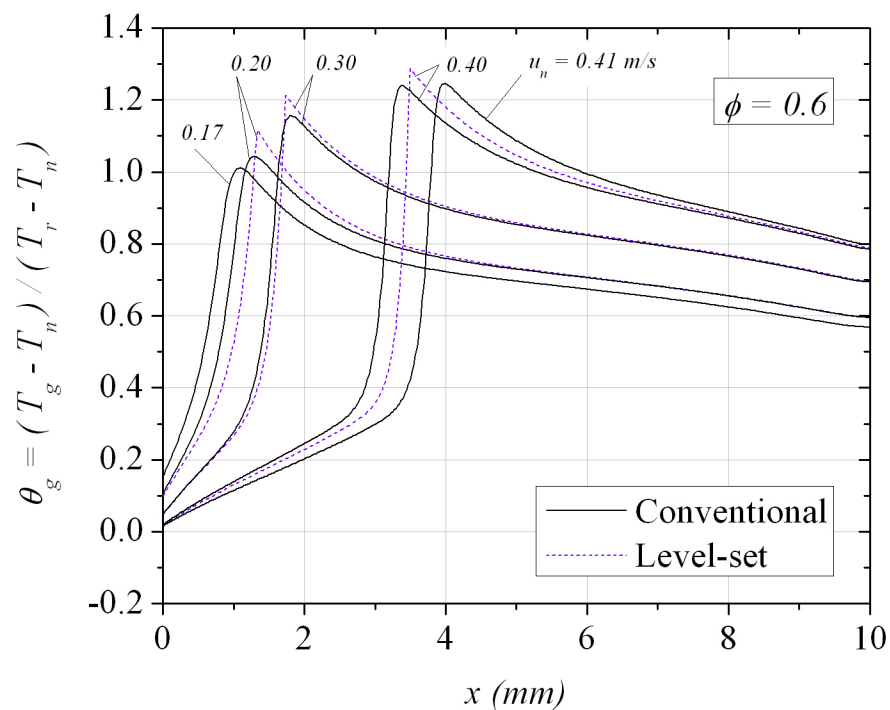


Figure 6.13: Gas-phase temperature distributions as a function of the inlet flow velocity u_n for $\phi = 0.6$.

which also meets with difficulties in finding the converged solution.

In summary, the present problem shows that the level-set model is able to predict reasonably well the flame position and temperature distributions as a function of the inlet flow velocity for moderately lean mixtures ($\phi \geq 0.6$) with reduced computational effort. The difficulties in extending the present model to multidimensional problems are discussed in the next section.

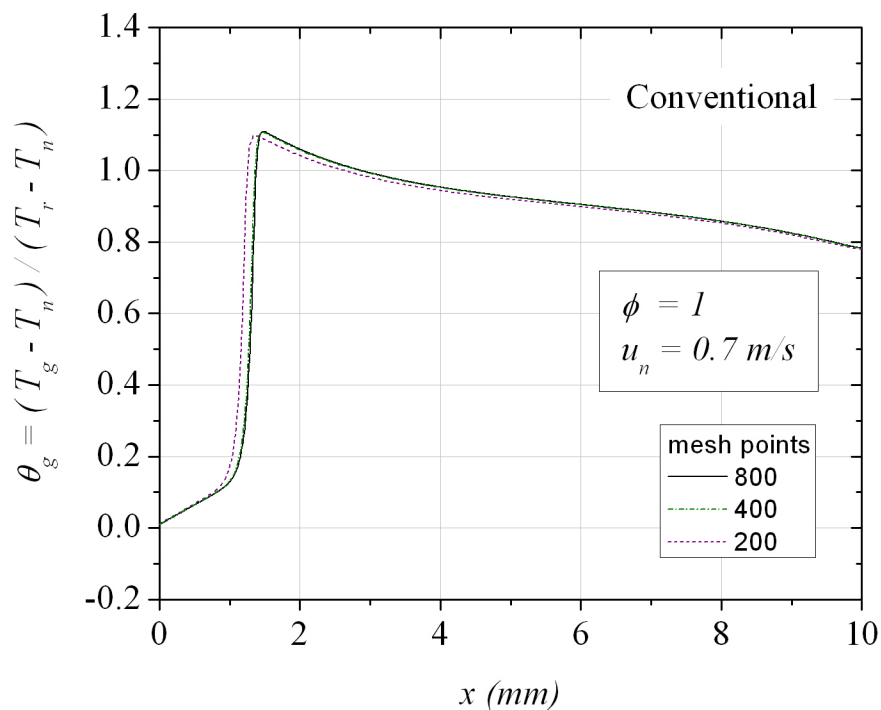


Figure 6.14: Dependence of the gas-phase temperature on the numerical mesh for the conventional model.

6.4.3 Discussion on multi-dimensional implementation

The level-set model can be employed to study two- and three-dimensional problems. The expected advantage is the requirement of less computational effort than that with conventional models. This advantage comes from the fact that the level-set model does not solve the inner structure of the flame and that coarser grids can be used.

However, in multidimensional problems two important aspects of the present model need to be adapted. The first one is the reinitialization scheme. In the 1D problem solved here, the direct reinitialization scheme used was easy to implement

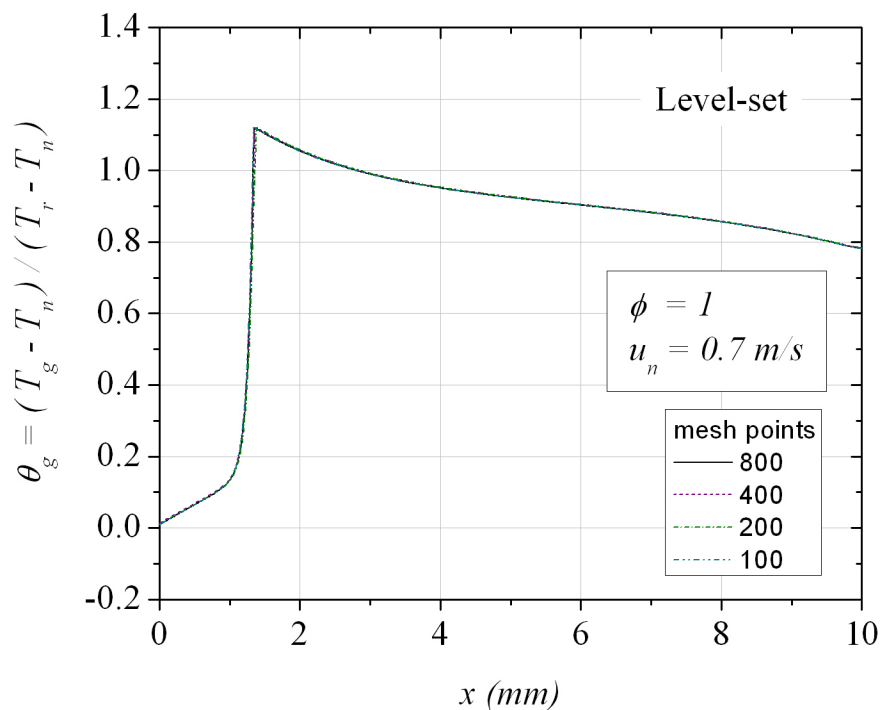


Figure 6.15: Dependence of the gas-phase temperature on the numerical mesh for the level-set model.

and had a marginal impact in the *CPU* time. In the proposed scheme, the flame position ($G = G_0$) is precisely identified (via front tracking) and the G -field is imposed to be a signed distance function based on the position of the mesh points in relation to the flame position [$G(x) = x - x_f$]. This approach is computationally demanding for 2D and 3D simulations. A more efficient scheme that could be used is based on the solution at each time step of a transient reinitialization equation for the G -field that has the properties of maintaining its zeroth-level while converging it to a signed distance function at steady-state [101]. A method for solving this equation that guarantees the conservation of the flame surface is proposed in the literature

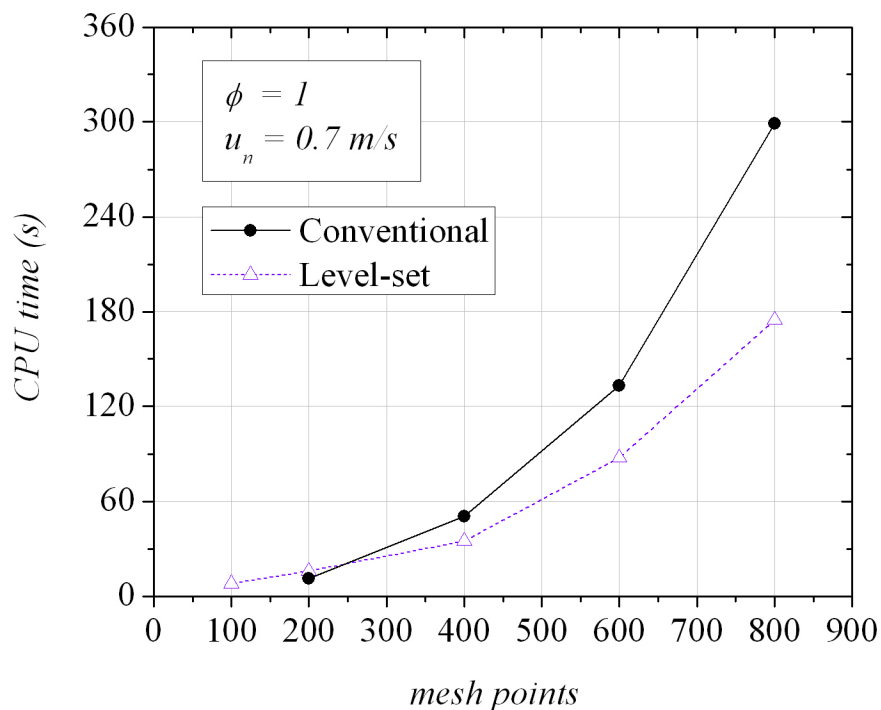


Figure 6.16: CPU time vs mesh points.

[102]. Additionally, since the G -equation is valid only at flame surface, the reinitialization procedure could be restricted to a narrow region around $G = G_0$ (narrow band approach).

The second aspect to be addressed in multidimensional simulations is the distribution of the heat release. The scheme proposed here relies on geometric considerations based in the comparison of the G -field and the reaction length-scale, l_R , thus determining the heat source at each mesh cell. Again, this scheme is simple to be employed in the 1D problem, but can be computationally demanding in multidimensional simulations. Nevertheless, this approach is currently being used by some authors [104, 108].

Another option is to develop some kind of temperature or heat release reconstruction as proposed in [106].

An important characteristic of the present level-set model is that the flame speed is intrinsically dependent on the flame front temperature through η_{rec} . The advantage of this dependence is that the effect of flame curvature in the large scale, l_S , is already accounted for by the numerical solution of the gas- and solid-phase energy equations. Note that the curvature effect for the combustion in porous media is much more pronounced than in free-flames, since the solid-phase conductivity enlarges the thermal affected region. Then, as a first approximation, no modification to Eq. (6.4) is needed to avoid formation of cusps. On the other hand, this approach requires the identification of the flame temperature and, consequently, the flame position (via front tracking) at each time step, what may reduce the computational advantages.

6.5 Conclusions

A level-set model is developed for the simulation of complex three-dimensional flow and reaction in porous media. This model is based on a subgrid model that relates the flame speed (microscale model) to the flame temperature that results from the energy balance between the phases (macroscale model). The species conservation equation is not solved and the heat release is distributed around the flame position in the gas-phase. The flame movement is accounted for by a transport equation of a non-reacting scalar G that describes the propagation of the flame front.

A 1D version of the model is implemented to validate the method and is compared to a conventional model based on the solution of the full set of conservation equations. Two situations were studied, the flame propagation in an adiabatic infinite medium

and the flame stabilization in a finite medium with radiant heat losses at the ends. The results of the level-set model were in accordance with a conventional model for both cases. Flame velocities, gas and solid-phase temperature profiles and flame position were reasonably well predicted with the present approach.

The advantage of the proposed method is the lower *CPU* times required to achieve convergence. For the problems studied, the level-set model is 6 to 16 times faster than the conventional model, when $\phi \geq 0.6$. In the present implementation, the heat release is distributed in a length-scale that is smaller than the mesh size. Then, better results are obtained for higher equivalence ratios since, in these flames, the concentration of the heat release in a thin region is a valid approximation.

Chapter 7

Conclusion

In this chapter, the conclusions obtained in the previous chapters are summarized and future works are proposed.

7.1 Summary of conclusions

This thesis is divided in two major parts. The first part is devoted to analytical analysis of the structure of lean stationary adiabatic premixed flames within porous inert media, covering a wide range of equivalence ratios (Chapters 3 to 5). The second part is devoted to the construction of a level-set model for multidimensional numerical simulations of porous radiant burners (Chapter 6).

In the model for $N \sim O(1)$ (Chapter 3) the principal characteristic length-scales of the problem were identified and used to construct an approximate solution for moderately lean mixtures ($0.6 \leq \phi \leq 0.8$). The two innermost length scales, the gas-phase length scale l_G and the reaction length scale l_R , are the same scales defined in the classical premixed flame structure analysis. The outermost length scale l_S , the solid-phase length scale, is related to the heat conduction in the porous matrix. In

this model, the interphase heat transfer at the gas-phase length-scale l_G is neglected (this is the reason why this model is not valid for extremely lean mixtures). Then, the influence of the porous medium on the flame is to increase its temperature and velocity and this influence is more pronounced for leaner mixtures, higher solid-phase thermal conductivities (higher Γ), lower porosities and lower fuel Lewis numbers. Also, under the hypotheses considered, a number that defines the effects of all these parameters, characterizing the flame variables and universalizing the results, is identified. For this reason, this number is called the porous-media-flame number. The upper bound for ϕ is a result of the simplifications made in the one-step kinetic mechanism used. This restriction is removed in the flame velocity expression used in Chapter 6.

In the model for $N \sim O(\Gamma)$ (Chapter 4), the flame structure is characterized by an intense interphase heat transfer, a condition found for ultra-lean mixtures. These flames present a wide region of local thermal equilibrium between the phases and the superadiabatic effect is limited by the interphase heat transfer at the gas-phase length-scale l_G . Contrary to the previous model, the superadiabatic flame temperature decreases as ϕ is decreased, i.e., as the interphase heat transfer becomes more intense, which implies the existence of a point of maximum nondimensional superadiabatic flame temperature in the lean side of the equivalence ratio spectrum. The model also shows (qualitatively) that, for extremely lean mixtures, the gas-phase temperature at the flame must reach a minimum superadiabatic flame temperature for the flame propagation to be possible, i.e., there is a lean flammability limit for the premixed combustion within porous inert media. A more accurate determination of this limit would require the use of, at least, a four-steps kinetic mechanism and the solution of the problem of $N \gg \Gamma$.

An alternative formulation, based on the excess enthalpy function, proposed in Chapter 5 was able to extend the validity of the first model ($N \sim O(1)$) for intermediate lean mixtures, where the condition $\Gamma > N \geq 1$ is found. This model shows (qualitatively) the maximum nondimensional superadiabatic temperature discussed in Chapter 4 and also predicts (qualitatively) the lean flammability limit.

Finally, a level-set model is developed for the simulation of complex three-dimensional flow and reaction in porous media (Chapter 6). This model is based on a subgrid model that relates the flame speed (microscale model) to the flame temperature that results from the energy balance between the phases (macroscale model). The flame movement is accounted for by the level-set method that describes the displacement of a thin interface due to the flow convection and self-propagation. The microscale model is built based on the results of the previous chapters. A 1D version of the model was implemented to illustrate the method and showed reasonable accordance with a conventional model based on the solution of the full set of conservation equations. The advantage of the proposed method is the lower *CPU* times required to achieve convergence. For the problems studied, the level-set model was 6 to 16 times faster than the conventional model.

7.2 Suggestions for future works

Some important extensions of the models presented in this thesis can be suggested for future works:

- To refine the model for $N \sim O(1)$ with the use of a 4-step kinetic mechanism, relaxing the assumption of a thin reaction region, to obtain more physical insights

about the solid matrix effect on the inner flame structure.

- To develop the model for $N \gg \Gamma$ with 4-step kinetic mechanism to study flame extinction phenomena.
- To include an approximate form of surface reaction dependent on pore size (through porosity and specific surface area) and assess the effect of surface reactions on flame extinction and propagation.
- To study the burning of liquid fuels in porous media, including in the the solid-phase length analysis a model for the droplet evaporation.
- To built a 2D version of the level-set model, including the solution of the radiant transfer equation (RTE) and temperature dependent properties, to compare with steady-state and transient experiments.

Bibliography

- [1] F. M. Pereira, Medição de características térmicas e estudo do mecanismo de estabilização de chama em queimadores porosos radiantes, Master monography, Departamento de Engenharia Mecânica, Universidade Federal de Santa Catarina, Florianópolis - SC (2002).
- [2] R. C. Catapan, F. M. Pereira, A. A. M. Oliveira, Development of a radiant porous burner with a combined thermal and fluidynamic mechanism of flame stabilization, Proc. Int. Congress of Mechanical Engineering - COBEM 2005 (Brazil).
- [3] J. R. Howell, M. J. Hall, J. L. Ellzey, Combustion of hydrocarbon fuels within porous inert media, Prog. Energy Combust. Sci. 22 (1996) 121–145.
- [4] A. A. M. Oliveira, M. Kaviany, Nonequilibrium in the transport of heat and reactants in combustion in porous media, Prog. Energy Combust. Sci. 27 (2001) 523–545.
- [5] S. Wood, A. Harris, Porous burners for lean-burn applications, Prog. Energy Combust. Sci. 34 (2008) 667–684.
- [6] F. J. Weinberg, Combustion temperatures: the future?, Nature 233 (1971) 239–241.

- [7] S. A. Lloyd, F. J. Weinberg, A burner for mixtures of very low heat content, *Nature* 251 (1974) 47–49.
- [8] D. R. Hardesty, F. J. Weinberg, Burners producing large excess enthalpies, *Combust. Sci. Technol.* 8 (1974) 201–214.
- [9] T. Takeno, K. Sato, An excess enthalpy flame theory, *Combust. Sci. Technol.* 20 (1979) 73–84.
- [10] R. Echigo, Radiation enhanced/controlled phenomena of heat and mass transfer in porous media, *ASME/JSME Thermal Eng. Proc.* 4 (1991) 21–32.
- [11] Y. Kotani, T. Takeno, An experimental study on stability and combustion characteristics of an excess enthalpy flame, *Proc. 19th Symposium (Intl.) on Combustion* (1982) 1503–1509.
- [12] D. K. Min, H. D. Shin, Laminar premixed flame stabilized inside a honeycomb ceramic, *Int. J. Heat Mass Transfer* 34 (1991) 341–356.
- [13] P. Hsu, W. D. Evans, J. R. Howell, Experimental and numerical study of premixed combustion within nonhomogeneous porous ceramics, *Combust. Sci. Technol.* 90 (1993) 149–172.
- [14] V. Khanna, R. Goel, J. L. Ellzey, Measurements of emissions and radiation for methane combustion within a porous medium burner, *Combust. Sci. Technol.* 99 (1994) 133–142.
- [15] R. Mital, J. P. Gore, R. Viskanta, A study of the structure of submerged reaction zone in porous ceramic radiant burners, *Combust. Flame* 111 (1997) 175–184.
- [16] S. A. Leonardi, R. Viskanta, J. P. Gore, Radiation and thermal performance measurements of a metal fiber burner, *J. Quant. Spectrosc. Ra.* 73 (2002) 491–501.

- [17] Y. Huang, C. Y. H. Chao, P. Cheng, Effects of preheating and operation conditions on combustion in a porous medium, *Int. J. Heat Mass Transfer* 45 (2002) 4315–4324.
- [18] J. Kiefer, M. C. Weikl, T. Seeger, F. von Issendorff, F. Beyrau, A. Leipertz, Non-intrusive gas-phase temperature measurement inside a porous burner using dual-pump cars, *Proc. Combust. Inst.*
- [19] X. Fu, R. Viskanta, J. P. Gore, Prediction of effective thermal conductivity of cellular ceramics, *Int. Comm. Heat Mass Transfer* 25 (1998) 151–160.
- [20] H. L. Pan, O. Pickenäcker, K. Pickenäcker, D. Trimis, T. Weber, Experimental determination of effective heat conductivities of highly porous media, Fifth European Conference on Industrial Furnaces and Boilers, Porto (Portugal).
- [21] X. Fu, R. Viskanta, J. P. Gore, Measurement and correlation of volumetric heat transfer coefficients of cellular ceramics, *Exp. Therm. Fluid Sci.* 17 (1998) 285–293.
- [22] K. Kamiuto, S. S. Yee, Heat transfer correlations for open-cellular porous materials, *Int. Comm. Heat Mass Transfer* 32 (2005) 947–953.
- [23] S. A. Zhdanok, K. V. Dobrego, S. I. Futko, Effect of porous media transparency on spherical and cylindrical filtration combustion heat transfer performance, *Int. J. Heat Mass Transfer* 43 (2000) 3469–3480.
- [24] D. Trimis, F. Durst, Combustion in a porous medium - advances and applications, *Combust. Sci. Technol.* 121 (1996) 153–168.
- [25] N. Delalic, D. Mulahasanovic, E. N. Ganic, Porous media compact heat exchanger unit - experiment and analysis, *Exp. Therm. Fluid Sci.* 28 (2004) 185–192.

- [26] S. Mößbauer, O. Pickenäcker, K. Pickenäcker, D. Trimis, Application of the porous burner technology in energy- and heat-engineering, Proc. Fifth International Conference on Technologies and Combustion for a Clean Environment (Clean Air V), Lisbon (Portugal) 1 (1999) 519–523.
- [27] Z. Al-Hamamre, S. Diezinger, P. Talukdar, F. von Issendorff, D. Trimis, Combustion of low calorific gases from landfills and waste pyrolysis using porous medium burner technology, Trans IChemE 84 (2006) 297–308.
- [28] M. A. A. Mendes, J. M. C. Pereira, J. C. F. Pereira, On the stability of ultra-lean H₂/CO combustion in inert porous burners, Int. J. of Hydrogen Energ. 33 (2008) 3416–3425.
- [29] M. Kaplan, M. J. Hall, The combustion of liquid fuels within a porous media radiant burner, Exp. Therm. Fluid Sci. 11 (1995) 13–20.
- [30] T. K. Kayal, M. Chakravarty, Combustion of liquid fuel inside inert porous media: an analytical approach, International Journal of Heat and Mass Transfer 48 (2005) 331–339.
- [31] S. Vijaykant, A. K. Agrawal, Liquid fuel combustion within silicon-carbide coated carbon foam, Exp. Therm. Fluid Sci. 32 (2007) 117–125.
- [32] P. H. Bouma, L. P. H. D. Goey, Premixed combustion on ceramic foam burners, Combust. Flame 119 (1999) 133–143.
- [33] I. Cerri, G. Saraco, V. Specchia, Methane combustion over low-emission catalytic foam burners, Catal. Today 60 (2000) 21–32.
- [34] I. Cerri, G. Saraco, V. Specchia, D. Trimis, Improved-performance knitted fibre mats as supports for pre-mixed natural gas catalytic combustion, Chem. Eng. J. 82 (2001) 73–85.

- [35] S. Jugjai, A. Sawananon, The surface combustor-heater with cyclic flow reversal comustion embedded with water tube bank, *Fuel* 83 (2004) 2369–2379.
- [36] S. Zhdanok, L. A. Kennedy, G. Koester, Superadiabatic combustion of methane air mixtures under filtration in a packed bed, *Combust. Flame* 100 (1995) 221–231.
- [37] K. V. Dobrego, N. N. Gnesdilov, S. H. Lee, H. K. Choi, Lean combustibility limit of methane in reciprocal flow filtration combustion reactor, *Int. J. Heat Mass Transfer* 51 (2008) 2190–2198.
- [38] R. S. Dhamrat, J. L. Ellzey, Numerical and experimental study of the conversion of methane to hydrogen in a porous reactor, *Proc. Int. Congress of Mechanical Engineering - COBEM 2005 (Brazil)* 18.
- [39] I. Schoegl, J. L. Ellzey, A mesoscale fuel reformer to produce syngas in portable power systems, *Proc. Combust. Inst.*
- [40] M. A. Mujeebu, M. Z. Abdullah, M. Z. A. Bakar, A. A. Mohamad, M. K. Abdullah, Applications of porous media combustion technology a review, *Appl. Energ.* 86 (2009) 1365–1375.
- [41] M. A. Mujeebu, M. Z. Abdullah, M. Z. A. Bakar, A. A. Mohamad, M. K. Abdullah, A review of investigations on liquid fuel combustion in porous inert media, *Prog. Energy Combust. Sci.* 35 (2009) 216–230.
- [42] M. A. Mujeebu, M. Z. Abdullah, M. Z. A. Bakar, A. A. Mohamad, R. M. N. Muhad, M. K. Abdullah, Combustion in porous media and its applications a comprehensive survey, *J. Environ. Manage.* 90 (2009) 2287–2312.
- [43] Y. Yoshizawa, K. Kiyoshi, R. Echigo, Analytical study of the structure of radiation controlled flame, *Int. J. Heat Mass Transfer* 31 (1988) 311–319.

- [44] M. Sahraoui, M. Kaviany, Direct simulation vs volume-averaged treatment of adiabatic, premixed flame in a porous medium, *Int. J. Heat Mass Transfer* 37 (1994) 2817–2834.
- [45] F. A. Lammers, L. P. H. de Goey, A numerical study of flash back of laminar premixed flames in ceramic-foam surface burners, *Combust. Flame* 133 (2003) 47–61.
- [46] P. Talukdar, S. C. Mishra, D. Trimis, F. Durst, Heat transfer characteristics of a porous radiant burner under the influence of a 2-D radiation field, *J. Quant. Spectrosc. Ra.* 84 (2004) 527–537.
- [47] A. J. Barra, J. L. Ellzey, Heat recirculation and heat transfer in porous burners, *Combust. Flame* 137 (2004) 230–241.
- [48] M. A. A. Mendes, J. M. C. Pereira, J. C. F. Pereira, A numerical study of the stability of one-dimensional laminar premixed flames in inert porous media, *Combust. Flame* 153 (2008) 525–539.
- [49] G. Brenner, K. Pickenäcker, O. Pickenäcker, D. Trimis, K. Wawrzinek, T. Weber, Numerical and experimental investigation of matrix-stabilized methane/air combustion in porous inert media, *Combust. Flame* 123 (2000) 201–213.
- [50] T. C. Hayashi, I. Malico, J. C. F. Pereira, Three-dimensional modeling of a two-layer porous burner for household applications, *Comput. Struct.* 82 (2004) 1543–1550.
- [51] C. L. Hackert, J. L. Ellzey, O. A. Ezekoye, Combustion and heat transfer in model two-dimensional porous burners, *Combust. Flame* 116 (1999) 177–191.
- [52] P. J. Elverum, J. L. Ellzey, D. Kovar, Durability of YZA ceramic foams in a porous burner, *J. Mater. Sci.* 40 (2005) 155–164.

- [53] N. Peters, *Turbulent combustion*, Cambridge University Press, London, 2000.
- [54] H. Pitch, L. D. de Lageneste, Large-eddy simulation of premixed turbulent combustion using a level-set approach, *Proc. Combust. Inst.* 29 (2002) 2001–2008.
- [55] L. P. H. de Goey, J. H. M. Boonkamp, A flamelet description of premixed laminar flames and the relation with flame stretch, *Combust. Flame* 119 (1999) 253–271.
- [56] J. A. van Oijen, L. P. H. de Goey, Modelling of premixed laminar flames using flamelet generated manifolds, *Combust. Sci. Technol.* 161 (2000) 113–137.
- [57] J. A. van Oijen, F. A. Lammers, L. P. H. de Goey, Modeling of complex premixed burner systems by using flamelet-generated manifolds, *Combust. Flame* 127 (2001) 2124–2134.
- [58] G. D. Ingram, I. T. Cameron, K. M. Hangos, Classification and analysis of integrating frameworks in multiscale modelling, *Chem. Eng. Sci.* 59 (2004) 52171–2187.
- [59] F. M. Pereira, A. A. M. Oliveira, F. F. Fachini, Asymptotic analysis of stationary adiabatic premixed flames in porous inert media, *Combust. Flame* 156 (2009) 152–165.
- [60] T. Poinso, D. Veynante, *Theoretical and Numerical Combustion*, Edwards, Philadelphia, 2000.
- [61] R. B. Bird, W. E. Stewart, E. N. Lightfoot, *Transport Phenomena*, John Wiley and Sons, New York, 1960.
- [62] R. Aris, *Vectors, tensors, and the basic equations of fluid mechanics*, Dover, New York, 1962.

- [63] M. Kaviany, Principles of heat transfer in porous media, 2nd Edition, Springer-Verlag, New York, 1995.
- [64] J. Daou, M. Matalon, Influence of conductive heat-losses on the propagation of premixed flames in channels, *Combust. Flame* 128 (2002) 321–339.
- [65] M. Quintard, M. Kaviany, S. Whitaker, Two-medium treatment of the heat transfer in porous media: numerical results for effective properties, *Adv. Water Resour.* 20 (1997) 77–94.
- [66] I. Nozad, R. G. Carbonell, S. Whitaker, Heat conduction in multiphase systems - i, theory and experiments for two-phase systems, *Chem. Eng. Sci.* 40 (1985) 843–855.
- [67] M. Kaviany, Principles of convective heat transfer, Springer-Verlag, New York, 1994.
- [68] S. R. Turns, An introduction to combustion: concepts and applications, 2nd Edition, McGraw-Hill, New York, 2000.
- [69] X. Y. Zhou, J. C. F. Pereira, Comparison of four combustion models for simulating the premixed combustion in inert porous media, *Combust. Flame* 118 (1998) 76–90.
- [70] P. Hsu, R. Matthews, The necessity of using detailed kinetics in models for premixed combustion within porous media, *Combust. Flame* 93 (1993) 457–466.
- [71] R. Siegel, J. R. Howell, Thermal radiation heat transfer, 3rd Edition, Taylor and Francis, 1992.
- [72] M. Kaviany, B. P. Singh, Radiative heat transfer in porous media, *Adv. Heat Transfer* 23 (1993) 133–186.

- [73] P. Hsu, J. R. Howell, Measurements of thermal conductivity and optical properties of porous partially stabilized zirconia, *Exp. Heat Transfer* 5 (1993) 293–313.
- [74] B. Deshaies, G. Joulin, Asymptotic study of an excess-enthalpy flame, *Combust. Sci. Technol.* 22 (1980) 281–285.
- [75] J. D. Buckmaster, T. Takeno, Blow-off and flashback of an excess-enthalpy flame, *Combust. Sci. Technol.* 25 (1981) 153–159.
- [76] T. Takeno, K. Sato, K. Hase, A theoretical study on an excess enthalpy flame, *Proc. Combust. Instit.* (1980) 465–472.
- [77] L. Boshoff-Mostert, H. J. Viljoen, Analysis of the homogeneous combustion in monolith structures, *Chem. Engng. Sci.* 51 (1996) 1107–1111.
- [78] A. P. Aldushin, S. G. Kasparian, Stability of stationary filtrational combustion waves, *Combust. Explo. Shock* (1982) 615–625.
- [79] A. P. Aldushin, B. J. Matkowsky, D. A. Schultz, Downward buoyant filtration combustion, *Combust. Flame* 107 (1996) 151–176.
- [80] D. A. Schultz, B. J. Matkowsky, V. A. Volker, A. C. Fernandez-Pello, Forced forward smolder combustion, *Combust. Flame* 104 (1996) 1–26.
- [81] A. P. Aldushin, I. E. Rumanov, B. J. Matkowsky, Maximal energy accumulation in a superadiabatic filtration combustion wave, *Combust. Flame* 118 (1998) 76–90.
- [82] C. W. Wahle, B. J. Matkowsky, Rapid, upward buoyant filtration combustion waves driven by convection, *Combust. Flame* 124 (2001) 14–34.
- [83] C. W. Wahle, B. J. Matkowsky, A. P. Aldushin, Effects of gas-solid nonequilibrium in filtration combustion, *Combust. Sci. Technol.* 175 (2003) 1389–1499.

- [84] V. I. Bubnovich, S. A. Zhdanok, K. V. Dobrego, Analytical study of the combustion waves propagation under filtration of methane-air mixture in a packed bed, *Int. J. Heat Mass Transfer* 49 (2006) 2578–2586.
- [85] A. C. McIntosh, Simplified model of a surface-combustion burner with radiant heat emission, *AIAA Prog. Astronaut. Aeronaut.* 113 (1988) 385–405.
- [86] A. C. McIntosh, A. Prothero, A model of large heat transfer surface combustion with radiant heat emission, *Combust. Flame* 83 (1991) 111–126.
- [87] A. Liñán, The asymptotic structure of counterflow diffusion flames for large activation energies, *Acta Astronautica* 1 (1974) 1007–1039.
- [88] F. A. Williams, *Combustion theory, the fundamental theory of chemically reacting flow systems*, Perseus Books, Cambridge Massachusetts, 1985.
- [89] Y. B. Zel'dovich, G. L. Barenblatt, V. B. Librovich, G. M. Makhviladze, *The mathematical theory of combustion and explosions*, Consultants Bureau, New York, 1985.
- [90] F. Fachini, A. Liñán, Transient effects in droplet ignition phenomenon, *Combust. Flame* 109 (1997) 303–313.
- [91] F. Fachini, Transient effects in the droplet combustion process in an acoustically perturbed high temperature environment, *Combust. Sci. Technol.* 139 (1998) 173–189.
- [92] F. Fachini, A. Liñán, F. A. Williams, Theory of flame histories in droplet combustion at small stoichiometric fuel-air ratios, *AIAA J.* 37 (1999) 1426–1435.
- [93] D. L. Zhu, F. N. Egolfopoulos, C. K. Law, Experimental and numerical determination of laminar flame speeds of methane/(Ar, N₂, CO₂)-air mixtures as

- function of stoichiometry, pressure and flame temperature, Proc. 22nd Symposium (Intl.) on Combustion, The Combustion Institute, Pittsburgh, PA, (1989) 1539–1545.
- [94] S. V. Patankar, Numerical heat transfer and fluid flow, Hemisphere Publishing Corporation, 1980.
- [95] J. F. Liu, W. H. Hsieh, Experimental investigation of combustion in porous heating burners, Combust. Flame 138 (2004) 295–303.
- [96] Y. Kotani, H. F. Behbahani, T. Takeno, An excess enthalpy flame combustor for extended flow ranges, Proc. 12th Symposium (Intl.) on Combustion (1984) 2025–2033.
- [97] H. M. R. J. Ellzey, Modeling of filtration combustion in a packed bed, Combust. Flame 117 (1999) 832–840.
- [98] I. Schoegl, J. Ellzey, Superadiabatic combustion in conducting tubes and heat exchangers of finite length, Combust. Flame 151 (2007) 142–159.
- [99] M. van Dike, Perturbation methods in fluid mechanics, Academic Press Inc., New York, 1964.
- [100] I. S. Watchman, R. Vance, A study of one-dimensional laminar premixed flame annihilation, Combust. Flame 110 (1997) 508–523.
- [101] M. Sussman, P. Smereka, S. Osher, A level set approach for computing solutions to incompressible two-phase flow, J. Comput. Phys. 114 (1994) 146–159.
- [102] G. Russo, P. Smereka, A remark on computing distance functions, J. Comput. Phys. 163 (2000) 51–67.
- [103] M. Herrmann, Numerical simulation of turbulent bunsen burner flames with a level set flamelet model, Combust. Flame 145 (2006) 357–375.

- [104] L. Ma, J. Chomiak, Asymptotic flame shapes and speeds of hydrodynamically unstable laminar flames, *Proc. Combust. Inst.* (1998) 545–553.
- [105] Z. Tan, R. Reitz, An ignition and combustion model based on the level-set method for spark ignition engine multidimensional modeling, *Combust. Flame* 145 (2006) 1–15.
- [106] J. Piana, D. Veynante, S. Candel, T. Poinsot, Direct numerical simulation analysis of the G-equation in premixed combustion, *Direct and large eddy simulation II* (1997) 321–330.
- [107] U. C. Muller, M. Bollig, N. Peters, Approximations for burning velocities and markenstein numbers for lean hydrocarbons and methanol flames, *Combust. Flame* 108 (1997) 349–356.
- [108] L. Liang, R. Reitz, Spark ignition engine combustion modeling using a level set method with detailed chemistry, *Multi-dimensional engine modelling - SAE* 01-0243.